

**MATHEMATICAL MODELLING OF LIGHT
PROPAGATION IN PHOTONIC CRYSTAL
WAVEGUIDES**

**A Thesis Submitted to
the Graduate School of Engineering and Sciences of
İzmir Institute of Technology
in Partial Fulfillment of the Requirements for the Degree of**

DOCTOR OF PHILOSOPHY

in Mathematics

**by
Neslihan ETİ**

**July 2014
İZMİR**

We approve the thesis of **Neslihan ETİ**

Examining Committee Members:

Assoc. Prof. Dr. H. Sami SÖZÜER
Department of Physics, İzmir Institute of Technology

Prof. Dr. Oktay K. Pashaev
Department of Mathematics, İzmir Institute of Technology

Prof. Dr. M. Salih Dinleyici
Department of Electric and Electronics Engineering, İzmir Institute of Technology

Prof. Dr. Coşkun İşçi
Department of Electric and Electronics Engineering, Yaşar University

Prof. Dr. Orhan Öztürk
Department of Physics, İzmir Institute of Technology

24 July 2014

Assoc. Prof. Dr. H. Sami SÖZÜER
Supervisor, Department of Physics
İzmir Institute of Technology

Prof. Dr. Oğuz YILMAZ
Head of the Department of
Mathematics

Prof. Dr. R. Tuğrul ŞENGER
Dean of the Graduate School of
Engineering and Sciences

ACKNOWLEDGMENTS

My journey with İyte began in 1999 and now ends after 15 years. First I was an undergraduate student in the Physics Department, then I was a master student and thereafter a Phd student in the Mathematics Department. So, this appreciation is not only for Phd but also for all of this 15 years. In this respect, it is a pleasure for me to acknowledge all members of the Physics and the Mathematics Department.

I am grateful to my thesis advisor, Assoc. Prof. Dr. H. Sami Sözüer, whose tolerance, insight and patience helped me throughout my study. He has been a tremendous mentor for me. It was a privilege to be his student.

I would like to thank Prof. Dr. Oktay K. Pashaev, who has been a perfect role-model to me through my undergraduate, graduate and Phd years. I have learned a lot from him. He has been a great mentor for me.

I would like to express my sincere gratitude to Prof. Dr. M. Salih Dinleyici, not only for his time and extreme patience, but for his intellectual contributions to my thesis.

The numerical calculations reported in this thesis were fully performed at TUBITAK ULAKBIM, High Performance and Grid Computing Center (TRUBA resources). So I would like to thank TUBITAK ULAKBIM, especially Sefa Arslan.

I wish to thank my lab-mates, Adem Enes Erol and Zebih Çetin, for the fun and their supports. I am very glad to meet with them. I learned alot from Zebih Çetin about computers, he was always very patient to me.

I should also thank to my friends, Tina B. Sevim, Koray Sevim, Barış Ateş, Barış Çiçek, Şengül N. Tümer for their sincere friendship, their endless and unconditional support. I would never forget all the chats and beautiful moments I shared with them.

My deepest gratitude goes to my family for their unflagging love and unconditional support throughout my life and my studies.

Finally, I would like to thank my husband, Murat Eti. he was always there cheering me up and stood by me through the good times and bad.

ABSTRACT

MATHEMATICAL MODELLING OF LIGHT PROPAGATION IN PHOTONIC CRYSTAL WAVEGUIDES

Photonic crystals are artificially engineered materials where the dielectric constant varies periodically. A photonic band gap can be created by scattering at the dielectric interfaces, which forbids propagation of light in a certain frequency range of light. This property enables us to control light, which is normally impossible with conventional optics. Moreover, by placing a linear defect into the photonic crystal, one can construct a waveguide, which keeps light inside the waveguide in the desired direction. Thus, by using photonic crystal waveguides one can control light propagation in integrated circuit devices.

The goal of this work is to provide a comprehensive understanding of how to bend light using photonic crystal waveguides. The purpose is to create a 90° bend for line defect photonic crystal assisted waveguides and present fully three-dimensional calculations with optimized geometrical parameters that minimize the bending loss.

The scheme uses one-dimensional photonic crystal slab waveguides for straight sections, and a corner element that employs a square photonic crystal with a band gap at the operating frequency..

The two different structures, with either silicon-silica or with silicon-air are used in the guiding photonic crystal layer. Furthermore, the guiding layer is sandwiched between either air on both top and bottom, or between air on top and silica substrate at the bottom, to serve as the "cladding" medium. Calculations are presented for the transmission values of TE-like modes where the electric field is strongly transverse to the direction of propagation, with and without the photonic crystal corner element for comparison. We find that the bending loss can be reduced to under 2%.

ÖZET

IŞIĞIN FOTONİK KRİSTAL DALGA KILAVUZUNDA YAYILIMININ MATEMATİKSEL MODELLEMESİ

Fotonik kristaller, dielektrik sabitinin periyodik olarak değiştiği, yapay olarak düzenlenmiş malzemelerdir. Fotonik bant aralığı ise fotonik kristale gönderilen ışığın, belli bir bant aralığındaki frekanslarda yayılımının yasaklanması anlamına gelir. Bu özellik yardımıyla, geleneksel optik ile normalde mümkün olmayan ışığın kontrol altına alınmasını sağlayabiliriz. Ayrıca, fotonik kristalin iine doğrusal bir kusur koyarak dalga kılavuzu elde edilebilir, böylece bir tel nasıl iinde akımı saklıyor ve onu taşıyorsa, fotonik kristal dalga kılavuzunda dalga kılavuzunun iinde ışığı saklar ve onu istenilen yöne taşır. Bu yol ile, fotonik kristal dalga kılavuzları sayesinde ışık iletimini entegre devre cihazlarda kontrol edebiliriz.

Bu çalışmanın amacı, fotonik kristal dalga kılavuzlarında ışığın bükülmesi konusunu kapsamlı bir şekilde incelemektir. Amaç fotonik kristal destekli çizgisel kusurlu dalga kılavuzunu 90° açı ile bükme ve üç boyutlu hesaplamalarla bükmeden kaynaklı kayıpları parametreleri optimize ederek minimuma indirmektir.

Önerilen yöntem ile ışık düz ilerlerken bir boyutta periyodik dalga kılavuzu kullanılır, ışık döneceği zaman iki boyutta periyodik kare örgülülü fotonik kristal içine girer, dönüşünü tamamlar ve tekrar düz ilerlemek üzere bir boyutta periyodik dalga kılavuzunun içine girer.

Çalışmamızda kılavuz katmanı olarak iki farklı yapı üzerinde çalışılmıştır. Bu yapılardan biri silika-silikon kullanılarak diğeri ise hava-silikon kullanılarak elde edilmiştir. Ayrıca, kılavuz katmanını iki farklı şekilde çalışılmıştır. Birincisinde, kılavuz katmanını üstten ve alttan hava arasına alınmıştır, ikincisinde ise kılavuz katmanını üstten hava ve alttan silika arasına alınmıştır.

Hesaplamalar TE-benzeri modları için verilmiştir, TE-benzeri modlar tanım olarak elektrik alanın ışığın yayılım yönünde bileşeninin değerinin 0'a yakın olduğu durumdur. Işığın virajı dönmeden önce ve döndükten sonra enerji değerleri oranlanmış, iletim bu orana göre hesaplanmıştır. İletim değeri grafiklerinde fotonik kristal dalga kılavuzu kullanılarak tasarlanan yapılarla sadece dalga kılavuzu kullanılarak tasarlanmış yapılara ait sonuçlar karşılaştırılmalı olarak verilmiştir. Dönmeden kaynaklanan kayıpların %2'nin altına indirilebileceği gösterilmiştir.

This thesis is dedicated to my lovely son, Bilge Kağan Eti: there were many times when this thesis took me away from precious moments with him.

TABLE OF CONTENTS

LIST OF FIGURES	ix
LIST OF TABLES	xiii
CHAPTER 1. INTRODUCTION	1
1.1. Photonic Crystals	2
1.2. Photonic Crystal Waveguides	4
1.3. Photonic Crystal Waveguide Slabs	6
1.4. Overview of the Thesis	8
CHAPTER 2. FUNDAMENTAL CONCEPTS	9
2.1. Maxwell's Equations in Inhomogeneous Media	9
2.1.1. Maxwell's Equations	9
2.1.2. Maxwell's Equations and the Eigenvalue Problem	11
2.1.3. Boundary Conditions	14
2.1.4. Energy Density and Continuity Theorem	16
2.2. Periodic Dielectric Function	17
2.2.1. Bloch-Floquet Theorem and Brillouin Zones	23
CHAPTER 3. FINITE DIFFERENCE TIME DOMAIN METHOD	26
3.1. Discretization of Maxwell's Equations	26
CHAPTER 4. DIELECTRIC WAVEGUIDE SLABS	31
4.1. SYMMETRIC DIELECTRIC WAVEGUIDE SLABS	32
4.1.1. Guided TE Modes	35
4.1.2. Guided TM Modes	40
4.1.3. Mode Profiles of Symmetric Dielectric Waveguide Slab	42
4.2. ASYMMETRIC DIELECTRIC WAVEGUIDE SLABS	46
4.2.1. Guided TE Modes	46
4.2.2. Guided TM Modes	48
4.2.3. Mode Profiles of Asymmetric Dielectric Waveguide Slab	50
CHAPTER 5. PHOTONIC CRYSTAL WAVEGUIDE SLAB (PCW-SLAB)	55

5.1. PCW-Slab as an Eigenvalue Problem	56
5.1.1. Similarity Transformation	60
5.2. PCW-Slab Structure	63
5.2.1. 1D-LDWG Slab Structure	63
5.2.2. 2D-LDWG Slab Structure	64
CHAPTER 6. L-SHAPED PHOTONIC CRYSTAL WAVEGUIDE SLAB	67
6.1. Waveguide Structures in 2D	67
6.2. Waveguide Structures in 3D.....	70
6.3. Mode Polarization	72
6.4. Mode Coupling	74
6.5. Silica Silicon Waveguide Slab	74
6.5.1. Symmetric Silica Silicon Waveguide Slab	74
6.5.2. Asymmetric Silica Silicon Waveguide Slab	78
6.6. Air Silicon Waveguide Slab.....	81
6.6.1. Symmetric Air Silicon Waveguide Slab.....	81
6.6.2. Asymmetric Air Silicon Waveguide Slab	86
6.7. Transmission Results.....	89
CHAPTER 7. CONCLUSION	99
REFERENCES	100

LIST OF FIGURES

<u>Figure</u>	<u>Page</u>
Figure 1.1. Examples of photonic crystals; periodically in 1D in a), periodically in 2D in b) and periodically in 3D in c).	2
Figure 1.2. If the incoming wavelength of light is in the order of a , then light at the specific frequencies is evanescent.	3
Figure 1.3. Photonic band gap of silicon circles are placed in the air.	4
Figure 1.4. When we locate a defect into the structure we see an extra mode in the band gap.	5
Figure 1.5. FDTD simulations of the single-core waveguide slab bend and the photonic crystal assisted waveguide bend. The single-core waveguide slab is excited with a mode source that matches the guided mode at the guided frequency in a). The photonic crystal assisted waveguide bend is excited with a mode source which is in the band gap in b).	6
Figure 1.6. The proposed waveguide slab, which is a combination of 1D-LDWGS and 2D-LDWGS.	7
Figure 2.1. $2D$ perfect square lattice in real space.	19
Figure 2.2. $2D$ perfect square lattice in reciprocal space.	20
Figure 2.3. $\epsilon(r)$ in a unit cell for $2D$ perfect square lattice. $V_{cell} = a_1 a_2$	22
Figure 2.4. The first Brillouin zone is shown with red square and the irreducible Brillouin zone with the symmetry points $\Gamma = (0, 0)$, $X = (0, \frac{\pi}{a})$ and $M = (\frac{\pi}{a}, \frac{\pi}{a})$. The path to calculate band structure is taken as $\Gamma \rightarrow X \rightarrow M \rightarrow \Gamma$	24
Figure 2.5. The TE and TM modes for a perfect 2D square lattice.	25
Figure 3.1. 2D computation region for TM modes	28
Figure 3.2. FDTD simulation region with perfectly matched layer (PML). PML absorbs electromagnetic waves at the boundaries without reflections.	30
Figure 4.1. Dielectric waveguide slab.	31
Figure 4.2. Symmetric dielectric waveguide slab.	32
Figure 4.3. For odd TE modes graphical roots.	39
Figure 4.4. Band diagram of Symmetric Dielectric Waveguide Slab. Refraction indexes are $n_1 = 1$, $n_2 = 3.6$, $R_z = a$, a is a period of the cell, all cell is $41a$. The cell is taken in z-direction and light propagates in x-direction. The structure of the band diagram is shown in Fig. (4.2). The band diagram is calculated by using MPB program.	43

Figure 4.5. <i>TE</i> Confined Modes for Symmetric Dielectric Waveguide Slab. Y-axis shows E_y component of the electric field, and x-axis shows the z direction of the waveguide slab.	44
Figure 4.6. <i>TM</i> Confined Modes for Symmetric Dielectric Waveguide Slab. Y-axis shows H_y component of the magnetic field, and x-axis shows the z direction of the waveguide slab.	44
Figure 4.7. <i>TE</i> Radiation Modes for Symmetric Dielectric Waveguide Slab. Y-axis shows E_y component of the electric field, and x-axis shows the z direction of the waveguide slab.	45
Figure 4.8. <i>TM</i> Radiation Modes for Symmetric Dielectric Waveguide Slab. Y-axis shows H_y component of the magnetic field, and x-axis shows the z direction of the waveguide slab.	45
Figure 4.9. Asymmetric waveguide slab.	46
Figure 4.10. Band Diagram for Asymmetric Dielectric Waveguide Slab. Refraction indexes are $n_1 = 1$, $n_2 = 3.61$, $n_3 = 1.58$ $R_z = a$, a is a period of the cell. The length of the cell is $41a$. The cell is taken in z -direction and light propagates in x -direction.	51
Figure 4.11. <i>TE</i> Confined Modes for Asymmetric Dielectric Waveguide Slab. Y-axis shows E_y component of the electric field, and x-axis shows the z direction of the waveguide slab.	52
Figure 4.12. <i>TM</i> Confined Modes for Asymmetric Dielectric Waveguide Slab. Y-axis shows H_y component of the magnetic field, and x-axis shows the z direction of the waveguide slab.	52
Figure 4.13. <i>TE</i> Slab Modes for Asymmetric Dielectric Waveguide Slab. Y-axis shows E_y component of the electric field and x-axis shows the z direction of the waveguide slab.	53
Figure 4.14. <i>TM</i> Slab Modes for Asymmetric Dielectric Waveguide Slab. Y-axis shows H_y component of the magnetic field and x-axis shows the z direction of the waveguide slab.	53
Figure 4.15. <i>TE</i> Radiation Modes for Asymmetric Dielectric Waveguide Slab. Y-axis shows E_y of the electric field, and x-axis shows the z direction of the waveguide slab.	54
Figure 4.16. <i>TM</i> Radiation Modes for Asymmetric Dielectric Waveguide Slab. Y-axis shows H_y components of the magnetic field, and x-axis shows the z direction of the waveguide slab.	54
Figure 5.1. PCW-slab	55
Figure 5.2. 1D-LDWG slab.	66

Figure 5.3. 2D-LDWG slab.	66
Figure 6.2. L-shaped photonic crystal line defect waveguide in 2D on the top, geometrical details of line defect waveguide on the bottom.	68
Figure 6.3. "Silica silicon waveguide". The overlapped band diagrams of 1D-LDWG in green color and 2D-LDWG in black color.	69
Figure 6.4. "Air silicon waveguide." The overlapped band diagrams of 1D-LDWG in green color and 2D-LDWG in black color.	70
Figure 6.6. 2D-LDWG band diagrams of "silica silicon waveguide" for TE modes, TM modes and for mixed modes.	72
Figure 6.8. 2D-LDWG band diagrams of "air silicon waveguide" for TE modes, TM modes and for mixed modes.	73
Figure 6.9. Symmetric silica silicon waveguide slab.	75
Figure 6.10. Band diagrams of silica silicon waveguide (1D-LDWG)	76
Figure 6.11. Band diagrams of symmetric silica silicon waveguide slab (1D-LDWG Slab).	76
Figure 6.12. Band diagrams of silica silicon waveguide (2D-LDWG)	77
Figure 6.13. Band diagrams of symmetric silica silicon waveguide slab (2D-LDWG Slab).	77
Figure 6.14. Matched band diagrams of symmetric silica silicon waveguide slab.	78
Figure 6.15. Asymmetric silica silicon waveguide slab.	78
Figure 6.16. Band diagram of asymmetric silica silicon waveguide, 1D-LDWG Slab, mixed modes.	79
Figure 6.17. Band diagram of asymmetric silica silicon waveguide slab (2D-LDWG Slab).	80
Figure 6.18. Matched band diagrams of asymmetric silica silicon waveguide slab.	80
Figure 6.19. Symmetric air silicon waveguide slab.	81
Figure 6.21. Band diagrams of air silicon waveguide (1D-LDWG) and symmetric air silicon waveguide slab (1D-LDWG Slab).	82
Figure 6.23. Band diagrams of air silicon waveguide (2D-LDWG) and symmetric air silicon waveguide slab (2D-LDWG Slab).	84
Figure 6.24. Matched band diagrams of symmetric air silicon waveguide slab.	85
Figure 6.25. Asymmetric air silicon waveguide slab.	86
Figure 6.26. Band diagram of asymmetric air silicon waveguide, 1D-LDWG Slab, mixed modes.	87
Figure 6.27. Band diagram of asymmetric air silicon waveguide slab (2D-LDWG Slab).	87
Figure 6.28. Matched band diagrams of asymmetric air silicon waveguide slab.	88

Figure 6.29. $z = 0$ slice from 3D slab is shown with $d_{separ} = 0.2a$. All parameters are the same described for 3 dimensional system.	90
Figure 6.30. FDTD simulations of $z = 0$ slice from "silica silicon waveguide" symmetric slab. On the left the slab is at the frequency of $\omega a/2\pi c = 0.2967$ which is in the band gap. a, b and c show different plane sections for the figure on the left. On the right the slab is at the frequency of $\omega a/2\pi c = 0.2633$ which is below the band gap. The wave is gaussian with width $\Delta(\omega a/2\pi c) = 0.1$	90
Figure 6.31. $z = 0$ slice from 3D single slab is shown. Single slab is a waveguide without photonic crystal assistance.	91
Figure 6.32. Transmission result of MEEP according to different values of $\omega a/2\pi c$ for the "silica silicon waveguide". All parameters are the same described for 3D system.	92
Figure 6.33. Transmission result of MEEP according to different values of $\omega a/2\pi c$ for the "air silicon waveguide". All parameters are the same described for 3D system.	93
Figure 6.34. FDTD simulations of the symmetric silicon silica waveguide slab at a frequency out of the photonic band gap, $\tilde{\omega} = 0.2633$	95
Figure 6.35. FDTD simulations of the symmetric silicon silica waveguide slab at a frequency in the photonic band gap, $\tilde{\omega} = 0.2966$	97

LIST OF TABLES

<u>Table</u>		<u>Page</u>
Table 6.1.	Dielectric values for each variations.	71
Table 6.2.	Mode polarizations.	74
Table 6.3.	The best transmission results.	98

CHAPTER 1

INTRODUCTION

We are going day by day towards miniaturization and high speed at today's information and communications technology. This brings to mind the question, what could be faster than electrons as the information carrier. The possible answer to this question is light, since physically the fastest thing that can be manipulated by current technology is light. Replacement of electrons by light has several benefits. Light can travel faster than electrons in the medium, it can carry larger information than electrons and since photons are not strongly interacting particles as electrons, this helps reduce energy losses.

The next question is how to use light as the information carrier instead of electrons. Photonic crystals are ideally suited for this task. Photonic crystals are very tempting for use in a new generation of integrated circuit design because of their unique ability to confine light within certain regions of space.

The history of photonic crystals starts with the early idea for electromagnetic wave propagation in a periodic medium, which was studied by Lord Rayleigh in 1887, that corresponds to 1D photonic crystals.

After 100 years, in 1987, two independent works appeared that are considered as the starting point of the research field. One was the paper was by Yablonovitch, titled "Inhibition of spontaneous emission of electromagnetic radiation using a three dimensionally periodic structure" [Yablonovitch (1987)]. Yablonovitch's idea was to understand controlling the spontaneous emission by modifying the photonic density of states of the medium using periodic dielectrics.

The second paper by Sajeev John was titled "Strong localization of photons in certain disordered dielectric super-lattices" [John (1987)]. John's aim was to understand how a random refractive-index variation affects photon localization.

In 1994, Meade et al. first time studied a 2D periodic dielectric waveguide [Meade et al. (1994)]. They showed that a linear defect mode in a photonic band gap can act as a waveguide for electromagnetic waves. They suggested to use this modes in bends, in y couplers, waveguide tappers and other devices, where the radiation loss causes problems. In 1996, Mekis et al. (1996) theoretically calculated sharp bends in photonic crystal waveguides. By numerical simulations, they got complete transmission at certain frequencies, and very high transmission ($> 95\%$) over wide frequency ranges. They observed high transmission even for 90 degrees bends with zero radius of curvature. The maximum transmission was 98%

as opposed to 30% for analogous conventional dielectric waveguides. This was experimentally demonstrated by Lin et al. (1998) in 1998 and the transmission efficiency is found larger than 80%.

In 1999, Johnson et al. (1999) searched the guided modes in photonic crystal slabs. They analysed the properties of 2D periodic dielectric structures but in 3D. These structures have a band gap for propagation in a plane and that use index guiding to confine light in the third dimension.

In 2000, Johnson et al. (2000), also published a paper about linear waveguides in photonic crystal slabs. Also in the same period, Lončar et al. (2000) designed and fabricated photonic crystal planar circuits in silicon on silicon dioxide. Shinya et al. (2002) studied on SOI-based photonic crystal line-defect waveguides. Since that time, there have been many publications about the different kinds of photonic crystal waveguides, Chutinan and Noda (2000), Lin et al. (2000), Tokushima et al. (2000), Noda et al. (2000), Kafesaki et al. (2002), Imada et al. (2006), Ishizaki and Noda (2009), Kawashima et al. (2010), Ishizaki et al. (2013).

1.1. Photonic Crystals

Photonic crystals are periodic artificial structures which control the motion of photons. The periodicity is obtained by using materials with different dielectric constants.

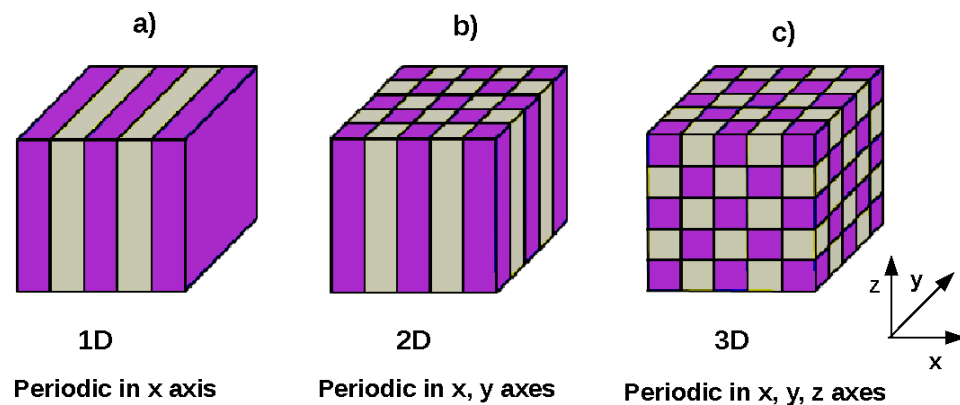


Figure 1.1. Examples of photonic crystals; periodically in 1D in a), periodically in 2D in b) and periodically in 3D in c).

Fig. (1.1) is an illustration of photonic crystals with various dimensionalities: a) represents 1D periodic photonic crystal since it is periodic only in x direction. b) represents 2D

periodic photonic crystal since it is periodic only in x and y directions. c) represents 3D periodic photonic crystal since it is periodic in x, y and z directions. The different colors in the figure represent materials with different dielectric constants.

Similar to wires that keep electrical currents, we can construct a photonic crystal to keep light in the desired direction. This ability to control the direction of light is gained by photonic band gaps [Joannopoulos et al. (1997)].

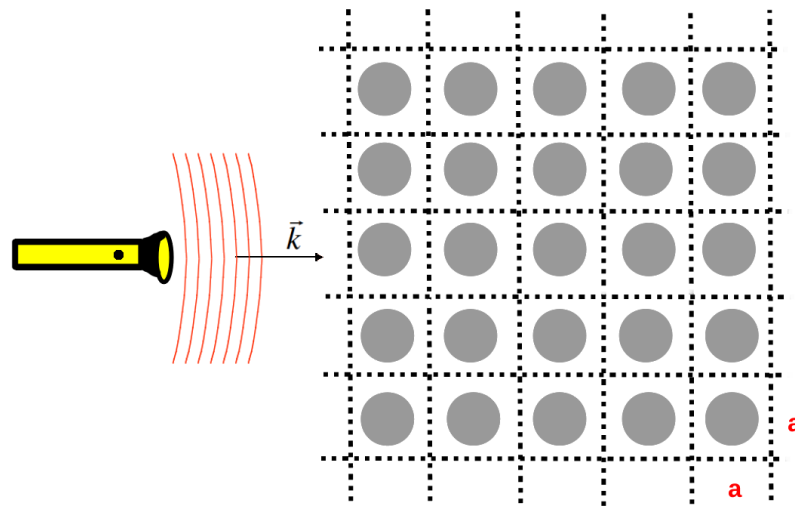


Figure 1.2. If the incoming wavelength of light is in the order of a , then light at the specific frequencies is evanescent.

To get a better understanding let's work through an example. In this example silicon circles, which form a square lattice, are placed in the air. So it is an example for 2 dimensionally periodic photonic crystal. light is sent through the circles as in Fig. (1.2). Here a is the lattice constant. If a is of the order of the wavelength of incoming light, photonic crystal won't let the light in the particular wavelength which leads a photonic band gap.

In Fig. (1.3), the band diagram of the example structure is given. Here the yellow region is the photonic band gap. So if the frequency of incoming wave is in the yellow region then it will not be able to propagate in the medium.

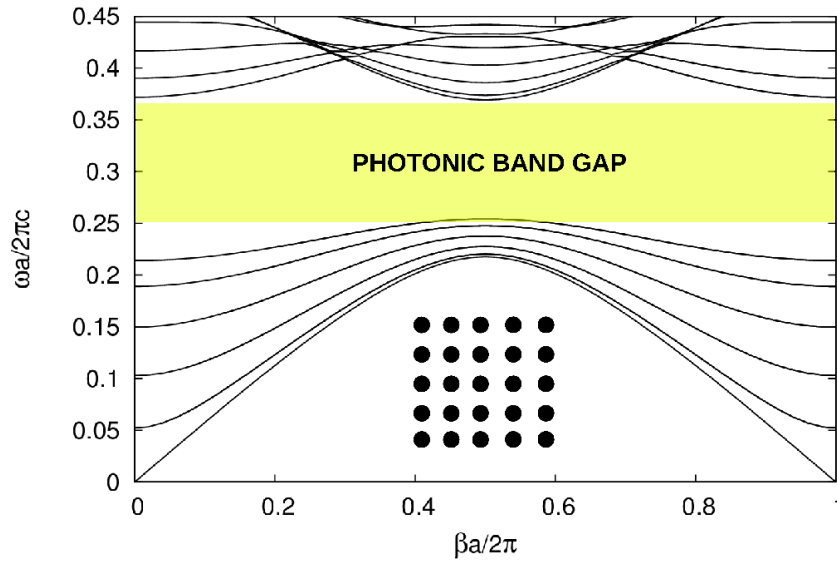


Figure 1.3. Photonic band gap of silicon circles are placed in the air.

As a result the photonic band gap forbids propagation of light in a certain frequency range of light. This property ensure us to control light to a degree which is normally impossible with conventional means.

1.2. Photonic Crystal Waveguides

Where can we use the photonic band gaps? One of the applications of photonic band gaps is photonic crystal waveguides: Meade et al. (1994), Benisty (1996), Mekis et al. (1998). We can create a waveguide placing a line defect into the photonic crystal. This line defect will behave like a waveguide.

To show the effect of a line defect in the photonic crystal, let's continue with the previous example. If we introduce a line defect into the photonic crystal in Fig. (1.2) the band diagram in Fig. (1.3) will slightly change as in Fig. (1.4).

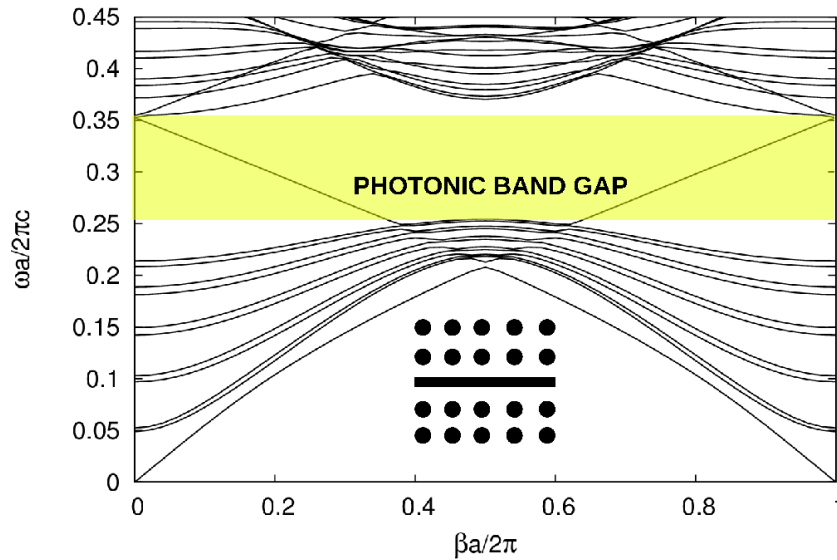


Figure 1.4. When we locate a defect into the structure we see an extra mode in the band gap.

In Fig. (1.4) the mode that appears inside the photonic band gap is the line defect mode. If one constructs a source with a frequency inside the photonic band gap, only this line defect mode will propagate in the material.

The photonic crystal waveguides can also be used to bend light [Mekis et al. (1996)].

In the single-core waveguide, guidance relies only on total internal reflection so the light propagates without loss, but when the single waveguide turns a sharp bend light is radiated and lost at the bend. Hence there is a serious leakage problem to bend light using a conventional single core waveguide.

In the photonic crystal assisted waveguide bend, since light can not escape because of the photonic band gap at the corner, light will propagate without any loss in the waveguide.

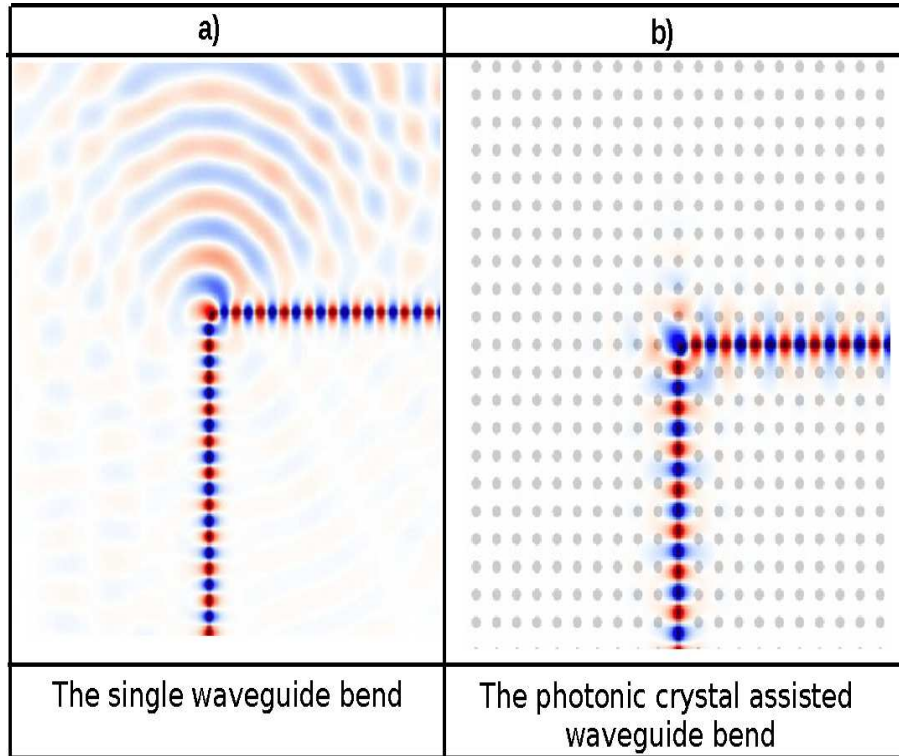


Figure 1.5. FDTD simulations of the single-core waveguide slab bend and the photonic crystal assisted waveguide bend. The single-core waveguide slab is excited with a mode source that matches the guided mode at the guided frequency in *a*). The photonic crystal assisted waveguide bend is excited with a mode source which is in the band gap in *b*).

In Fig. (1.5) we see snapshots from FDTD simulations of single-core waveguide bend in *a*) and photonic crystal assisted waveguide bend in *b*). In *a*) there is a serious leakage at the corner, but in *b*) light turns the bend without radiation.

So far we restricted our attention to purely two-dimensional systems. For the realistic cases, one can want to examine the effects of vertical confinement in the photonic crystal waveguides or fabricate these structures with a finite thickness. This time we call the photonic crystal waveguides in finite thickness as photonic crystal waveguide slabs.

1.3. Photonic Crystal Waveguide Slabs

Photonic-crystal waveguide slabs are 1 dimensionally or 2 dimensionally periodic dielectric structures with a finite thickness in vertical direction. Photonic crystal waveguide slabs have three-dimensional simple geometry, which consist of a thin guiding layer sand-

wiched between two bounded media Johnson et al. (1999), Johnson et al. (2000), Baba et al. (2002), Kuchinsky et al. (2000) Loncar et al. (2000). They have a band gap in the propagation plane and they use index-confinement in the third dimension. Their fabrication is easier than three-dimensionally periodic photonic crystals. This is why photonic crystal waveguide slabs have been proposed as an alternative to 3 dimensionally periodic photonic crystals Kawashima et al. (2010), Ishizaki et al. (2013).

Photonic crystal waveguide slabs must provide some conditions to obtain perfect transmission through bends in most of the integrated optical circuit designs Johnson et al. (2000):

- I. The waveguide must be periodic in the propagation direction to propagate without reflections.
- II. The waveguide must be single mode in the frequency range.
- III. The guided mode must be in the band gap of a photonic crystal to prevent radiation losses.

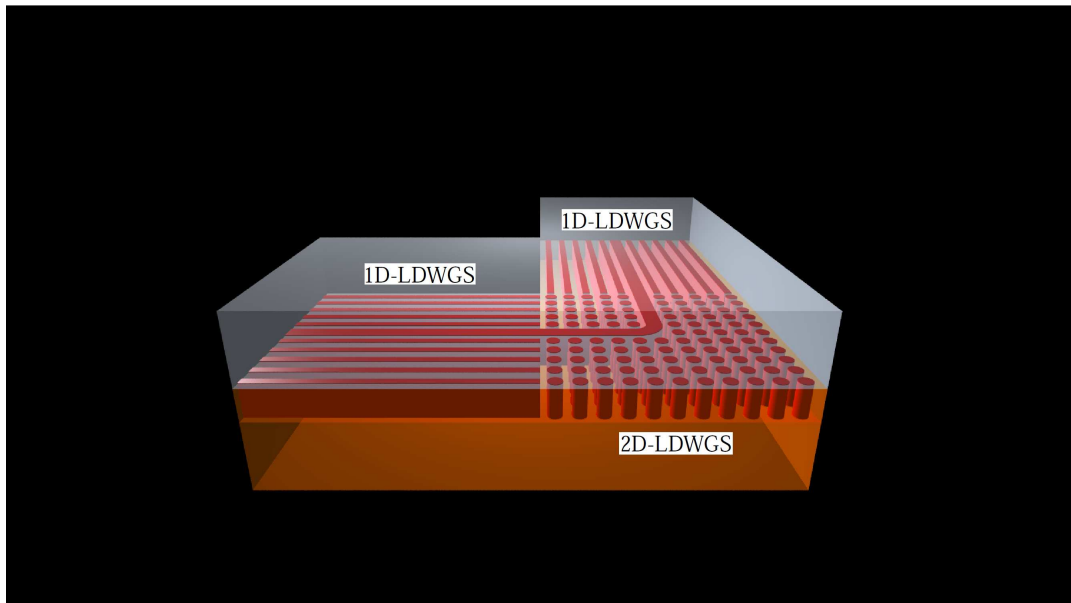


Figure 1.6. The proposed waveguide slab, which is a combination of 1D-LDWGS and 2D-LDWGS.

In this thesis, our aim is to design some novel corner elements using line defect photonic crystal slab waveguides for the integrated optical circuits. Basically, the studied corner elements are a combination of 1D (1D-LDWG slab) and 2D periodic (2D-LDWG slab) photonic crystal waveguide slabs.

The reason for this combination can be explained as follows; 1D-LDWG is a good option if light would travel straight. Therefore light will be guided with much less loss in such a waveguide due to lesser manufacturing imperfections as a result of its much simpler geometry Taniyama et al. (2005), Sözüer and Sevim (2005). But also 1D-LDWG slab is not useful to bend the light through a sharp turn because of its geometry. Besides 2D-LDWG is not a good choice for light to travel straight in it for long distances, it is still the most convenient geometry to bend the light through a sharp turn.

1.4. Overview of the Thesis

In chapter 2 we start from fundamental concepts. Firstly we give Maxwell's equations in inhomogeneous media which we then write as an Hermitian eigenvalue problem with appropriate boundary conditions. Secondly we introduce the periodic dielectric function, Bloch-Floquet theorem and Brillouin zones.

In chapter 3 we describe the Finite Difference Time Domain Method (FDTD) for the 2D Yee cell. First we discretize Maxwell's Equations and then we give the boundary conditions and talk about PML.

In chapter 4 we discuss dielectric waveguide slabs for symmetric and asymmetric cases. We will give the formalism for TE modes and TM modes. Also we give the mode profiles for waveguide slabs.

In chapter 5 we give mathematical analysis of photonic crystal waveguide slabs (PCW-Slab). First we define PCW-Slab as an eigenvalue problem. Then we will define a similarity transformation. After we introduce PCW-Slab structure for 1D-LDWG Slab and 2D-LDWG Slab.

In chapter 6 we talk about L-shaped PCW-Slab starting from waveguide structures in 2D and then give waveguide structures in 3D. After we will talk on mode polarization and mode coupling. Then silica silicon waveguide slab and air silicon waveguide slab for symmetric and asymmetric cases are given.

CHAPTER 2

FUNDAMENTAL CONCEPTS

2.1. Maxwell's Equations in Inhomogeneous Media

In this part we give some basic concepts about Maxwell's equations, then we formulate Maxwell's equations as a Hermitian eigenvalue problem. After we introduce the boundary conditions for Maxwell's equations, which are very important while solving electromagnetic wave problems. Then we will give the formulation of energy density and the continuity theorem. We present also periodic dielectric function, the Bloch-Floquet theorem and Brillouin zones.

2.1.1. Maxwell's Equations

The behaviour of electromagnetic (EM) radiation in a material medium is described by a set of four partial differential equations called Maxwell's Equations and stated as follows;

$$\nabla \times \mathbf{E}(\mathbf{r}, t) + \frac{\partial \mathbf{B}(\mathbf{r}, t)}{\partial t} = 0, \quad (2.1)$$

$$\nabla \times \mathbf{H}(\mathbf{r}, t) - \frac{\partial \mathbf{D}(\mathbf{r}, t)}{\partial t} = \mathbf{J}_f, \quad (2.2)$$

$$\nabla \cdot \mathbf{D}(\mathbf{r}, t) = \rho_f, \quad (2.3)$$

$$\nabla \cdot \mathbf{B}(\mathbf{r}, t) = 0, \quad (2.4)$$

where \mathbf{E} is electric field vector, \mathbf{H} is magnetic field vector, \mathbf{D} is electric displacement, \mathbf{B} is magnetic induction, ρ_f and \mathbf{J}_f are the free charge and current densities, respectively.

Equation (2.1) is called Faraday's law of induction, which describes how an electric field can be induced by a time-varying magnetic flux. Equation (2.2) is called Ampere's law, which describes the creation of an induced magnetic field due to charge flow and non-stationary electric field. Equation (2.3) is Coulomb's law, which describes the electric field distribution produced by the electric charge distribution. Equation (2.4) is a statement of the non-existence magnetic monopoles in nature.

The equations from Eq. (2.1) to Eq. (2.4) can be considered as 8 scalar equations that relate a total of 12 variables. To find field vectors these equations must be supplemented by the so-called constitutive equations, which describe the effect of electromagnetic fields in material media:

$$\mathbf{D} \equiv \epsilon \mathbf{E} = \epsilon_0 \mathbf{E} + \mathbf{P}, \quad (2.5)$$

$$\mathbf{B} \equiv \mu \mathbf{H} = \mu_0 \mathbf{H} + \mathbf{M}, \quad (2.6)$$

where ϵ and μ are the permittivity and the permeability, respectively (ϵ_0 and μ_0 are the permittivity and the permeability of vacuum). \mathbf{P} is the electric polarization of the medium and \mathbf{M} is the magnetization. We will work with linear, non-dispersive, non-lossy materials which leads to $\mathbf{D} = \epsilon_0 \epsilon \mathbf{E}$ and $\mathbf{B} = \mu_0 \mu \mathbf{H}$, with real ϵ and μ .

Also we allow ϵ and μ to vary from point to point in space, so we formulate them as follows;

$$\mathbf{D} = \epsilon_0 \epsilon(\mathbf{r}) \mathbf{E}, \quad (2.7)$$

$$\mathbf{B} = \mu_0 \mu(\mathbf{r}) \mathbf{H}. \quad (2.8)$$

In a material medium if the medium is dielectric then $\mu(r) \approx 1$. If there are no free charges and currents, i.e., if $\rho_f = 0$ and $\mathbf{J}_f = \mathbf{0}$, then Maxwell's equations become

$$\nabla \times \mathbf{E}(\mathbf{r}, t) = -\mu_0 \frac{\partial \mathbf{H}(\mathbf{r}, t)}{\partial t}, \quad (2.9)$$

$$\nabla \times \mathbf{H}(\mathbf{r}, t) = \epsilon_0 \frac{\partial \epsilon(\mathbf{r}) \mathbf{E}(\mathbf{r}, t)}{\partial t}, \quad (2.10)$$

$$\nabla \cdot [\epsilon(\mathbf{r}) \mathbf{E}(\mathbf{r}, t)] = 0, \quad (2.11)$$

$$\nabla \cdot \mathbf{H}(\mathbf{r}, t) = 0. \quad (2.12)$$

From Maxwell's equations the following wave equations for \mathbf{E} and \mathbf{H} can be derived;

$$\nabla \times (\nabla \times \mathbf{E}) + \frac{1}{c^2} \frac{\partial^2}{\partial t^2} \epsilon(\mathbf{r}) \mathbf{E} = 0, \quad (2.13)$$

$$\nabla \times \left(\frac{1}{\epsilon(\mathbf{r})} \nabla \times \mathbf{H} \right) + \frac{1}{c^2} \frac{\partial^2}{\partial t^2} \mathbf{H} = 0. \quad (2.14)$$

where $c = 1/\sqrt{\epsilon_0\mu_0}$ is the speed of light in vacuum.

2.1.2. Maxwell's Equations and the Eigenvalue Problem

Maxwell's equations are linear equations. This is why we can represent any solutions of Maxwell's equations in terms of a linear combination of harmonic modes in time

$$\begin{aligned}\mathbf{E}(\mathbf{r}, t) &= \mathbf{E}(\mathbf{r})e^{-i\omega t}, \\ \mathbf{H}(\mathbf{r}, t) &= \mathbf{H}(\mathbf{r})e^{-i\omega t}.\end{aligned}\tag{2.15}$$

In Eq. (2.15) to get physical fields we can take the real parts of the complex valued fields. Substituting Eq. (2.15) into Eqns. (2.9)-(2.10), we get;

$$\mathbf{E}(\mathbf{r}) = \frac{i}{\omega\epsilon_0\epsilon(\mathbf{r})}\nabla \times \mathbf{H}(\mathbf{r}),\tag{2.16}$$

$$\mathbf{H}(\mathbf{r}) = -\frac{i}{\omega\mu_0}\nabla \times \mathbf{E}(\mathbf{r}).\tag{2.17}$$

We can separate \mathbf{E} and \mathbf{H} . Let's work only on H . Taking the curl of Eq. (2.16) and substituting it to the right hand side of Eq. (2.17), we obtain an equation for \mathbf{H} :

$$\nabla \times \left(\frac{1}{\epsilon(\mathbf{r})}\nabla \times \mathbf{H}(\mathbf{r}) \right) = \left(\frac{\omega}{c} \right)^2 \mathbf{H}(\mathbf{r})\tag{2.18}$$

Here the velocity of light is $c = 1/\sqrt{\epsilon_0\mu_0}$. If we solve the above equation and find \mathbf{H} , we can find \mathbf{E} easily using Eq. (2.16).

Eq. (2.18) can be re-written as the eigenvalue equation in the next form;

$$\Theta\mathbf{H}(\mathbf{r}) = \left(\frac{\omega}{c} \right)^2 \mathbf{H}(\mathbf{r}),\tag{2.19}$$

where

$$\Theta\mathbf{H}(\mathbf{r}) \equiv \nabla \times \left(\frac{1}{\epsilon(\mathbf{r})}\nabla \times \mathbf{H}(\mathbf{r}) \right),\tag{2.20}$$

The eigenvectors $\mathbf{H}(\mathbf{r})$ are the harmonic modes, and Θ is an operator acting on $\mathbf{H}(\mathbf{r})$, $(\frac{\omega}{c})^2$ are the eigenvalues for corresponding eigenvectors, $\mathbf{H}(\mathbf{r})$.

The operator, Θ is a linear operator. We know that any linear combination of the solutions is again a solution; such as if \mathbf{H}_I and \mathbf{H}_{II} are both solutions of eigenvalue equation with the same frequency ω , then $a\mathbf{H}_I + b\mathbf{H}_{II}$ is again a solution with the same frequency ω , where a and b are arbitrary constants.

Since all observables must be represented by the Hermitian operators, the operator Θ should be Hermitian as well. We define the inner product of two vector fields $\mathbf{A}(\mathbf{r})$ and $\mathbf{B}(\mathbf{r})$ as

$$(\mathbf{A}, \mathbf{B}) \equiv \int d^3\mathbf{r} \mathbf{A}^*(\mathbf{r}) \cdot \mathbf{B}(\mathbf{r})$$

As easy to see it is bilinear form satisfying all properties of the inner product. Then the operator Θ is Hermitian operator if it satisfies the relation

$$(\mathbf{A}, \Theta\mathbf{B}) = (\Theta\mathbf{A}, \mathbf{B})$$

The proof is as follows:

$$(\mathbf{A}, \Theta\mathbf{B}) = \int d^3\mathbf{r} \mathbf{A}^* \cdot \left[\nabla \times \left(\frac{1}{\epsilon} \nabla \times \mathbf{B} \right) \right] \quad (2.21)$$

$$= \int d^3\mathbf{r} (\nabla \times \mathbf{A})^* \cdot \left(\frac{1}{\epsilon} \nabla \times \mathbf{B} \right) \quad (2.22)$$

$$= \int d^3\mathbf{r} \left[\nabla \times \left(\frac{1}{\epsilon} \nabla \times \mathbf{A} \right) \right]^* \cdot \mathbf{B} \quad (2.23)$$

$$= (\Theta\mathbf{A}, \mathbf{B}) \quad (2.24)$$

Here

$$\nabla \cdot (\mathbf{A} \times \mathbf{C}) = (\nabla \times \mathbf{A}) \cdot \mathbf{C} - \mathbf{A} \cdot (\nabla \times \mathbf{C})$$

and the Divergence Theorem and vanishing of the surface terms.

Properties of Hermitian operators:

1. Eigenvalues of a Hermitian operator are real.

Proof 2.1 *To prove this we start from the eigenvalue equation;*

$$\Theta \mathbf{H} = \left(\frac{\omega^2}{c^2} \right) \mathbf{H}, \quad (2.25)$$

let's take the inner product of the above equation with \mathbf{H} ,

$$(\mathbf{H}, \Theta \mathbf{H}) = \left(\frac{\omega^2}{c^2} \right) (\mathbf{H}, \mathbf{H}). \quad (2.26)$$

If we take the complex conjugate of the above equation we get

$$(\mathbf{H}, \Theta \mathbf{H})^* = \left(\frac{\omega^2}{c^2} \right)^* (\mathbf{H}, \mathbf{H}). \quad (2.27)$$

From the definition of the inner product we know $(\mathbf{H}, \Theta \mathbf{H}) = (\Theta \mathbf{H}, \mathbf{H})^$ and from the definition of the Hermitian property we know $(\mathbf{H}, \Theta \mathbf{H}) = (\Theta \mathbf{H}, \mathbf{H})$. Combining these informations we get the following result;*

$$\left(\frac{\omega^2}{c^2} \right) = \left(\frac{\omega^2}{c^2} \right)^*$$

which means ω^2 is real.

2. Non-equal eigenvectors corresponding to different eigenvalues are orthogonal.

Proof 2.2 *Let's consider two eigenvectors \mathbf{H}_I and \mathbf{H}_{II} with different eigen frequencies ω_I and ω_{II} . We start with eigenvalue equation for \mathbf{H}_I ;*

$$\Theta \mathbf{H}_I = \left(\frac{\omega_I}{c} \right)^2 \mathbf{H}_I \quad (2.28)$$

If take the inner product of the above equation with \mathbf{H}_{II} from the left, we get

$$(\mathbf{H}_{II}, \Theta \mathbf{H}_I) = \left(\frac{\omega_I}{c} \right)^2 (\mathbf{H}_{II}, \mathbf{H}_I). \quad (2.29)$$

Then we write eigenvalue equation for \mathbf{H}_{II} :

$$\Theta \mathbf{H}_{II} = \left(\frac{\omega_{II}}{c}\right)^2 \mathbf{H}_{II}, \quad (2.30)$$

If take the inner product of the above equation with \mathbf{H}_I from the right we get

$$(\mathbf{H}_{II}, \Theta \mathbf{H}_I) = \left(\frac{\omega_{II}}{c}\right)^2 (\mathbf{H}_{II}, \mathbf{H}_I). \quad (2.31)$$

Subtracting Eq. (2.29) from Eq. (2.31) we get;

$$(\omega_I^2 - \omega_{II}^2) (\mathbf{H}_{II}, \mathbf{H}_I) = 0 \quad (2.32)$$

This result show us if $\omega_I \neq \omega_{II}$ then the eigenvectors \mathbf{H}_I and \mathbf{H}_{II} are orthogonal. If $\omega_I = \omega_{II}$ then we say they are degenerate and not necessarily orthogonal.

2.1.3. Boundary Conditions

By using the divergence theorem and Stokes's theorem the Maxwell equations can be rewritten in integral form. These integral forms can be used to find the relationship of normal and tangential components of the fields between different boundary surfaces.

Firstly, we find relations between the normal components of the fields. Let V is a finite valume in space, S is a closed surface bounding that valume, da is an area element on the surface and \mathbf{n} is a the unit normal vector to the surface da , pointing towards outward from the enclosed surface. Applying the divergence theorem $\oint_S \mathbf{F} \cdot \mathbf{n} da = \int_V \nabla \cdot \mathbf{F} dV$ to Eq. (2.3) and Eq. (2.4) yields the integral relations

$$\oint_S \mathbf{D} \cdot \mathbf{n} da = \int_V \rho_f d^3x, \quad (2.33)$$

$$\oint_S \mathbf{B} \cdot \mathbf{n} da = 0. \quad (2.34)$$

Let's apply equations (2.33) and (2.34) to the valume of pillbox. We consider a pillbox, which is very shallow so that the side of the surfaces does not contribute to the integrals. The left

hand-side and right hand-side of Eq. (2.33) become

$$\oint_S \mathbf{D} \cdot \mathbf{n} da = (\mathbf{D}_2 - \mathbf{D}_1) \cdot \mathbf{n} \Delta a \quad (2.35)$$

$$\int_V \rho_f d^3x = \sigma \Delta a \quad (2.36)$$

As a result the normal components of \mathbf{D} and \mathbf{B} on the above and the below of the boundary are related to each other by

$$(\mathbf{D}_2 - \mathbf{D}_1) \cdot \mathbf{n} = \sigma, \quad (2.37)$$

$$(\mathbf{B}_2 - \mathbf{B}_1) \cdot \mathbf{n} = 0. \quad (2.38)$$

Here the normal component of \mathbf{D} is discontinuous by amount of σ at any boundary. The normal component of \mathbf{B} is continuous.

Secondly, we find the tangential components of the fields. Let C is a closed rectangular contour in space, S is a surface spanning the contour, $d\mathbf{l}$ is a line element on the contour. $d\mathbf{a}$ is area element on S , \mathbf{n} is a unit normal vector on $d\mathbf{a}$. Applying the Stoke's theorem $\oint_C \mathbf{F} \cdot d\mathbf{l} = \int_S \nabla \times \mathbf{F} \cdot d\mathbf{a}$ to Eq. (2.1) and Eq. (2.2) yields the integral relations

$$\oint_C \mathbf{H} \cdot d\mathbf{l} = \int_S \left[\mathbf{J} + \frac{\partial \mathbf{D}}{\partial t} \right] \cdot \mathbf{n} da \quad (2.39)$$

$$\oint_C \mathbf{E} \cdot d\mathbf{l} = - \int_S \frac{\partial \mathbf{B}}{\partial t} \cdot \mathbf{n} da \quad (2.40)$$

The short arms of rectangular contour C are negligible and long arms are parallel to the surface with length Δl . Then we can write for the left hand side of the (2.39) and (2.40);

$$\oint_C \mathbf{H} \cdot d\mathbf{l} = (\mathbf{t} \times \mathbf{n}) \cdot (\mathbf{H}_2 - \mathbf{H}_1) \Delta l, \quad (2.41)$$

$$\oint_C \mathbf{E} \cdot d\mathbf{l} = (\mathbf{t} \times \mathbf{n}) \cdot (\mathbf{E}_2 - \mathbf{E}_1) \Delta l, \quad (2.42)$$

and for the right hand side of the (2.39) and (2.40) as follows

$$\int_S \left[\mathbf{J} + \frac{\partial \mathbf{D}}{\partial t} \right] \cdot \mathbf{t} da = \mathbf{K} \cdot \mathbf{t} \Delta l, \quad (2.43)$$

$$- \int_S \frac{\partial \mathbf{B}}{\partial t} \cdot \mathbf{n} da = 0, \quad (2.44)$$

where \mathbf{K} is surface current density flowing on the boundary surface. Here Eq. (2.43) and second part of Eq. (2.44) are vanishing because $\frac{\partial \mathbf{D}}{\partial t}$ and $\frac{\partial \mathbf{B}}{\partial t}$ are finite at the surface and the area of the loop is zero, since the length of the short sides goes to zero. As a result the tangential components of \mathbf{H} and \mathbf{E} on each side of the boundary are related to each other as

$$\mathbf{n} \times (\mathbf{H}_2 - \mathbf{H}_1) = \mathbf{K}, \quad (2.45)$$

$$\mathbf{n} \times (\mathbf{E}_2 - \mathbf{E}_1) = 0. \quad (2.46)$$

Here the difference between the tangential components of \mathbf{H} is equal to the surface current density \mathbf{K} and tangential component of \mathbf{E} is continuous at the boundary surface.

In our study we will deal with situations in which the surface charge density σ and the surface current density \mathbf{K} , both of them vanish. In that case all normal and tangential components of \mathbf{B} and \mathbf{D} are continuous at the boundaries.

2.1.4. Energy Density and Continuity Theorem

Electromagnetic waves carry energy in the form of electromagnetic radiation. We want to find the energy stored in electromagnetic wave and the power flow with electromagnetic wave. Let's start from Maxwell's Equation, Eq. (2.2);

$$\nabla \times \mathbf{H} - \frac{\partial \mathbf{D}}{\partial t} = \mathbf{J}$$

The dot product of the above equation with \mathbf{E} gives us the work done by electromagnetic field, which is

$$\mathbf{J} \cdot \mathbf{E} = \mathbf{E} \cdot (\nabla \times \mathbf{H}) - \mathbf{E} \cdot \frac{\partial \mathbf{D}}{\partial t}. \quad (2.47)$$

If

$$\nabla \cdot (\mathbf{E} \times \mathbf{H}) = \mathbf{H} \cdot (\nabla \times \mathbf{E}) - \mathbf{E} \cdot (\nabla \times \mathbf{H})$$

and sequentially the Maxwell's Equation, Eq. (2.1);

$$\nabla \times \mathbf{E} = -\frac{\partial \mathbf{B}}{\partial t},$$

then we get

$$\mathbf{J} \cdot \mathbf{E} = -\nabla \cdot (\mathbf{E} \times \mathbf{H}) - \mathbf{H} \cdot \frac{\partial \mathbf{B}}{\partial t} - \mathbf{E} \cdot \frac{\partial \mathbf{D}}{\partial t}, \quad (2.48)$$

or

$$-\mathbf{J} \cdot \mathbf{E} = \nabla \cdot \mathbf{S} + \frac{\partial U}{\partial t}, \quad (2.49)$$

where $\mathbf{S} = \mathbf{E} \times \mathbf{H}$ is called the energy flux and $U = \frac{1}{2}(\mathbf{E} \cdot \mathbf{D} + \mathbf{B} \cdot \mathbf{H})$ is called the energy density of electromagnetic fields. Eq. (2.49) is known as continuity equation.

If $\mathbf{J} = 0$ then it states the decrease of electromagnetic energy density in a volume is a result of outflow of electromagnetic energy through the surface of that volume.

2.2. Periodic Dielectric Function

At the previous part we worked on Maxwell's equations, which is basically a second order partial differential equation and contains a periodic dielectric function in it.

In this part we will formalise the periodic dielectric function in the reciprocal space. The periodic dielectric function is a function of \mathbf{r} and it is periodic with a period \mathbf{R} , given by the next form:

$$\epsilon(\mathbf{r}) = \epsilon(\mathbf{r} + \mathbf{R}). \quad (2.50)$$

In Eq. (2.50), \mathbf{R} is called as the lattice vector and it is given by the next formula

$$\mathbf{R} = n_1 \mathbf{a}_1 + n_2 \mathbf{a}_2 + n_3 \mathbf{a}_3, \quad (2.51)$$

where, $\mathbf{a}_1, \mathbf{a}_2, \mathbf{a}_3$ are primitive vectors of the crystal lattice and not all of them are in the same plane ($\mathbf{a}_1 \cdot (\mathbf{a}_2 \times \mathbf{a}_3) \neq 0$). n_1, n_2, n_3 are integers. We can define the volume of the primitive unit cell as a cell that contains only one lattice point and call it as V_{cell} , which is equal to $V_{cell} = \mathbf{a}_1 \cdot (\mathbf{a}_2 \times \mathbf{a}_3)$

The periodic dielectric function can be expanded in terms of the Fourier series. Let's define a 3D Fourier basis function $e^{i\mathbf{G}\cdot\mathbf{r}}$ with $\mathbf{G} = m_1 \mathbf{b}_1 + m_2 \mathbf{b}_2 + m_3 \mathbf{b}_3$ for some basis vectors \mathbf{b}_i , ($i = 1, 2, 3$), which will find later in the calculations. Then the dielectric function in the Fourier basis is;

$$\epsilon(\mathbf{r}) = \sum_{\mathbf{G}} \epsilon(\mathbf{G}) e^{i\mathbf{G}\cdot\mathbf{r}}, \quad (2.52)$$

$$\epsilon(\mathbf{r} + \mathbf{R}) = \sum_{\mathbf{G}} \epsilon(\mathbf{G}) e^{i\mathbf{G}\cdot(\mathbf{r}+\mathbf{R})}. \quad (2.53)$$

Eq. (2.52) is equal to Eq. (2.53) because of the periodicity condition. Then subtracting Eq. (2.52) from Eq. (2.53) we get;

$$\sum_{\mathbf{G}} \epsilon(\mathbf{G}) e^{i\mathbf{G}\cdot\mathbf{r}} [1 - e^{i\mathbf{G}\cdot\mathbf{R}}] = 0 \quad (2.54)$$

This equation holds when $e^{i\mathbf{G}\cdot\mathbf{R}} = 1$, which means $\mathbf{G} \cdot \mathbf{R} = 2\pi n$, where n is an integer:

$$\mathbf{G} \cdot \mathbf{R} = (m_1 \mathbf{b}_1 + m_2 \mathbf{b}_2 + m_3 \mathbf{b}_3) \cdot (n_1 \mathbf{a}_1 + n_2 \mathbf{a}_2 + n_3 \mathbf{a}_3) = 2\pi n \quad (2.55)$$

This condition can be satisfied if we take $\mathbf{b}_i \cdot \mathbf{a}_j = 2\pi \delta_{ij}$, where $i, j = 1, 2, 3$, then

$$\mathbf{G} \cdot \mathbf{R} = 2\pi(m_1 n_1 + m_2 n_2 + m_3 n_3) \quad (2.56)$$

$$= 2\pi n. \quad (2.57)$$

Due to this condition \mathbf{b}_1 is perpendicular to both \mathbf{a}_2 and \mathbf{a}_3 . Also $\mathbf{a}_2 \times \mathbf{a}_3$ is perpendicular to both \mathbf{a}_2 and \mathbf{a}_3 so \mathbf{b}_1 must be parallel to $\mathbf{a}_2 \times \mathbf{a}_3$. We can write $\mathbf{b}_1 = \alpha(\mathbf{a}_2 \times \mathbf{a}_3)$, where α is a constant to be determined. We know that $\mathbf{b}_1 \cdot \mathbf{a}_1 = 2\pi$, writing the value of \mathbf{b}_1 we get $[\alpha(\mathbf{a}_2 \times \mathbf{a}_3)] \cdot \mathbf{a}_1 = 2\pi$. Omitting α we find $\alpha = 2\pi/[\mathbf{a}_1 \cdot (\mathbf{a}_2 \times \mathbf{a}_3)]$. Based on this, by cyclic permutations we can calculate the values of all primitive vectors of the reciprocal lattice;

$$\mathbf{b}_1 = 2\pi \frac{\mathbf{a}_2 \times \mathbf{a}_3}{\mathbf{a}_1 \cdot (\mathbf{a}_2 \times \mathbf{a}_3)}, \quad (2.58)$$

$$\mathbf{b}_2 = 2\pi \frac{\mathbf{a}_3 \times \mathbf{a}_1}{\mathbf{a}_2 \cdot (\mathbf{a}_3 \times \mathbf{a}_1)}, \quad (2.59)$$

$$\mathbf{b}_3 = 2\pi \frac{\mathbf{a}_1 \times \mathbf{a}_2}{\mathbf{a}_3 \cdot (\mathbf{a}_1 \times \mathbf{a}_2)}. \quad (2.60)$$

Example: Calculation of the reciprocal lattice vectors of 2D perfect photonic crystal
In Fig. (2.1) we see a 2D perfect square lattice. The primitive vectors are $\mathbf{a}_1 = a_1\hat{\mathbf{x}}$ and $\mathbf{a}_2 = a_2\hat{\mathbf{y}}$ and the lattice vector is $\mathbf{R} = a_1\hat{\mathbf{x}} + a_2\hat{\mathbf{y}}$.

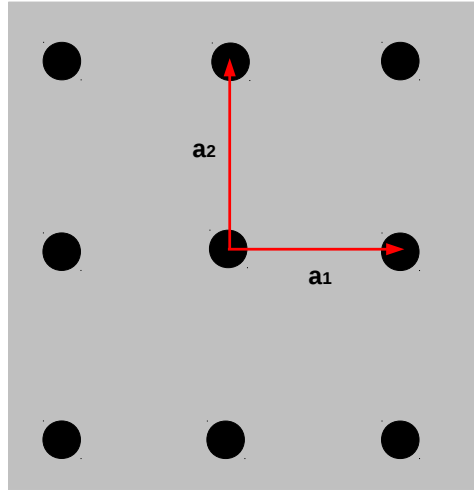


Figure 2.1. 2D perfect square lattice in real space.

If we calculate this lattice vectors in the reciprocal space first we should find the vectors for primitive cells of the reciprocal space: \mathbf{b}_1 , \mathbf{b}_2 and \mathbf{b}_3 using (2.58)-(2.60). The primitive vectors of the reciprocal space are $\mathbf{b}_1 = \frac{2\pi}{a_1}\hat{\mathbf{x}}$ and $\mathbf{b}_2 = \frac{2\pi}{a_2}\hat{\mathbf{y}}$ and the lattice vector is

$\mathbf{G} = \frac{2\pi}{a_1}\hat{\mathbf{x}} + \frac{2\pi}{a_2}\hat{\mathbf{y}}$. The Fig. (2.2) shows 2D perfect square lattice in reciprocal space. \triangle

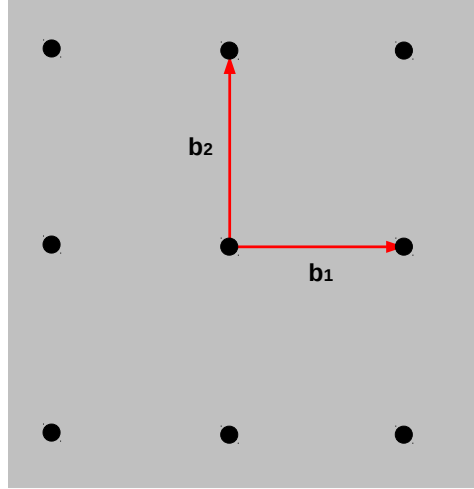


Figure 2.2. 2D perfect square lattice in reciprocal space.

Returning to our subject we can find the Fourier expansion of the periodic dielectric function $\epsilon(\mathbf{r}) = \epsilon(\mathbf{r} + \mathbf{R})$ in the form;

$$\epsilon(\mathbf{r}) = \sum_{\mathbf{G}} \epsilon(\mathbf{G}) e^{i\mathbf{G}\cdot\mathbf{r}}.$$

The next step is to find $\epsilon(\mathbf{G})$. For this reason we multiply the both sides of the above equation by $e^{-i\mathbf{G}'\cdot\mathbf{r}}$ and integrate over the primitive cell,

$$\int_{cell} \epsilon(\mathbf{r}) e^{-i\mathbf{G}'\cdot\mathbf{r}} d^3\mathbf{r} = \sum_{\mathbf{G}} \epsilon(\mathbf{G}) \int_{cell} \epsilon(\mathbf{r}) e^{-i(\mathbf{G}-\mathbf{G}')\cdot\mathbf{r}} d^3\mathbf{r} \quad (2.61)$$

To evaluate the integral, let's consider a primitive cell of parallelepiped formed by the vectors \mathbf{a}_1 , \mathbf{a}_2 , and \mathbf{a}_3 . We can construct an oblique coordinate system with the coordinates \mathbf{u} , \mathbf{v} , \mathbf{w} along the \mathbf{a}_1 , \mathbf{a}_2 and \mathbf{a}_3 directions, respectively. Then any vector \mathbf{r} can be written as $\mathbf{r} = x\mathbf{x} + y\mathbf{y} + z\mathbf{z} = u\mathbf{u} + v\mathbf{v} + w\mathbf{w}$, where

$$\mathbf{u} = \frac{\mathbf{a}_1}{a_1}, \quad \mathbf{v} = \frac{\mathbf{a}_2}{a_2}, \quad \mathbf{w} = \frac{\mathbf{a}_3}{a_3}.$$

The volume element $d^3\mathbf{r}$ is the volume of the parallelepiped which is equal to next form;

$$d^3\mathbf{r} = du dv dw \mathbf{u} \cdot (\mathbf{v} \times \mathbf{w}), \quad (2.62)$$

$$= du dv dw \frac{V_{\text{cell}}}{a_1 a_2 a_3}. \quad (2.63)$$

The argument of the exponential can be written as;

$$(\mathbf{G} - \mathbf{G}') \cdot \mathbf{r} = \mathbf{G}'' \cdot \mathbf{r} \quad (2.64)$$

$$= (m_1'' \mathbf{b}_1 + m_2'' \mathbf{b}_2 + m_3'' \mathbf{b}_3) \cdot \left(u \frac{\mathbf{a}_1}{a_1} + v \frac{\mathbf{a}_2}{a_2} + w \frac{\mathbf{a}_3}{a_3} \right) \quad (2.65)$$

$$= 2\pi \left(\frac{m_1'' u}{a_1} + \frac{m_2'' v}{a_2} + \frac{m_3'' w}{a_3} \right) \quad (2.66)$$

Now we are ready to evaluate the integral:

$$\begin{aligned} \int_{\text{cell}} \epsilon(\mathbf{r}) e^{-i(\mathbf{G}-\mathbf{G}') \cdot \mathbf{r}} d^3\mathbf{r} &= \frac{V_{\text{cell}}}{a_1 a_2 a_3} \int_0^{a_1} du e^{(i \frac{2\pi m_1'' u}{a_1})} \int_0^{a_2} dv e^{(i \frac{2\pi m_2'' v}{a_2})} \int_0^{a_3} dw e^{(i \frac{2\pi m_3'' w}{a_3})} \\ &= V_{\text{cell}} \delta_{m_1'' 0} \delta_{m_2'' 0} \delta_{m_3'' 0} \end{aligned} \quad (2.67)$$

$$= V_{\text{cell}} \delta_{\mathbf{G}'' 0} \quad (2.68)$$

$$= V_{\text{cell}} \delta_{\mathbf{G} \mathbf{G}'} \quad (2.69)$$

$$= V_{\text{cell}} \delta_{m_1 m_1'} \delta_{m_2 m_2'} \delta_{m_3 m_3'} \quad (2.70)$$

Substituting to Eq. (2.61) we obtain the value of $\epsilon(\mathbf{G})$:

$$\epsilon(\mathbf{G}) = \frac{1}{V_{\text{cell}}} \int_{\text{cell}} \epsilon(\mathbf{r}) e^{-i\mathbf{G} \cdot \mathbf{r}} d^3\mathbf{r}. \quad (2.71)$$

As continuation of the earlier example we calculate $\epsilon(\mathbf{G})$ using Eq. (2.71) for 2D perfect square lattice. Firstly we start the formulation of $\epsilon(\mathbf{r})$ just for a unit cell which is given in Fig. (2.3)

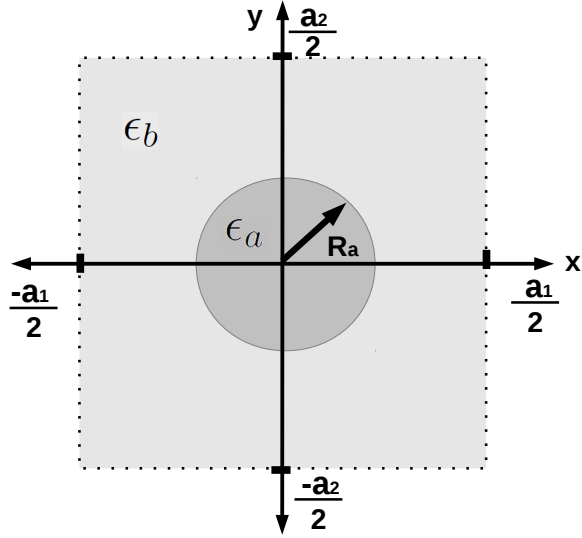


Figure 2.3. $\epsilon(r)$ in a unit cell for 2D perfect square lattice. $V_{cell} = a_1 a_2$

$$\begin{aligned}\epsilon(r) &= \epsilon(x, y), \\ &= \epsilon_b + (\epsilon_a - \epsilon_b)\Theta(|\mathbf{R}_a| - |\mathbf{r}|)\end{aligned}\quad (2.72)$$

Here $\Theta(x)$ is the step function and it is defined as

$$\Theta(x) = \begin{cases} 0 & \text{if } x < 0 \\ 1 & \text{otherwise} \end{cases}$$

Then we can calculate the integral;

$$\begin{aligned}\epsilon(\mathbf{G}) &= \frac{1}{V_{cell}} \int_{cell} \epsilon(\mathbf{r}) e^{-i\mathbf{G}\cdot\mathbf{r}} d^2\mathbf{r} \\ &= \frac{\epsilon_b}{V_{cell}} \int_{cell} e^{-i\mathbf{G}\cdot\mathbf{r}} d^2\mathbf{r} + \frac{(\epsilon_a - \epsilon_b)}{V_{cell}} \int_{cell} \Theta(|\mathbf{R}_a| - |\mathbf{r}|) e^{-i\mathbf{G}\cdot\mathbf{r}} d^2\mathbf{r} \\ &= \frac{\epsilon_b}{V_{cell}} \int_{cell} e^{-i(G_x x + G_y y)} dx dy + \frac{(\epsilon_a - \epsilon_b)}{V_{cell}} \int_0^{R_a} \int_0^{2\pi} e^{-i(Gr \cos \theta)} r dr d\theta \\ &= \epsilon_b \delta_{G_x 0} \delta_{G_y 0} + (\epsilon_a - \epsilon_b) \left(\frac{\pi R_a^2}{V_{cell}} \right) 2 \left(\frac{J_1(GR_a)}{GR_a} \right)\end{aligned}$$

or equivalently

$$\epsilon(\mathbf{G}) = \begin{cases} \epsilon_b + \left(\frac{\pi R_a^2}{V_{cell}}\right) (\epsilon_a - \epsilon_b) & \text{if } G = 0, \\ (\epsilon_a - \epsilon_b) 2 \left(\frac{J_1(GR_a)}{GR_a}\right) \left(\frac{\pi R_a^2}{V_{cell}}\right) & \text{if } G \neq 0. \end{cases} \quad (2.73)$$

2.2.1. Bloch-Floquet Theorem and Brillouin Zones

We present the Bloch-Floquet theorem, which was found in a one-dimensional setting by Floquet, Floquet (1883) and later rediscovered by Bloch in Bloch (1929). The Bloch-Floquet theorem for periodic eigenvalue problems states that the solutions of Eq. (2.18), can be written in the form:

$$\mathbf{H}(\mathbf{r}) = e^{i\mathbf{k}\cdot\mathbf{r}}\mathbf{H}_{n,\mathbf{k}}(\mathbf{r})$$

with eigenvalues $\omega_n(\mathbf{k})$, where $\mathbf{H}_{n,\mathbf{k}}$ is a periodic function, satisfying the equation;

$$(\nabla + i\mathbf{k}) \times \frac{1}{\epsilon} (\nabla + i\mathbf{k}) \times \mathbf{H}_{n,\mathbf{k}} = \left(\frac{\omega_n(\mathbf{k})}{c}\right)^2 \mathbf{H}_{n,\mathbf{k}} \quad (2.74)$$

where $n = 1, 2, \dots$

For each chose of \mathbf{k} the above equation give different eigenvalue problem over the primitive cell of the lattice. The eigenvalues $\omega_n(\mathbf{k})$ are continuous functions of \mathbf{k} forming the band structure when \mathbf{k} is plotted versus ω .

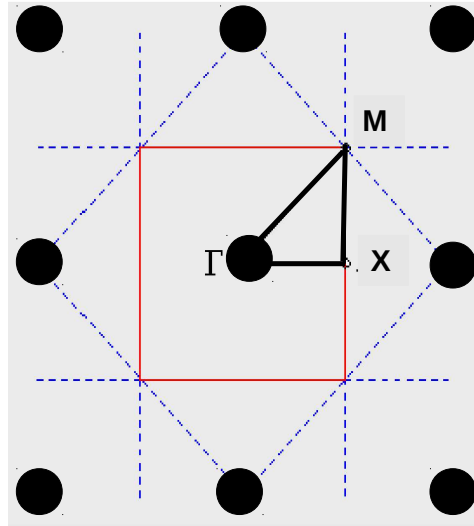


Figure 2.4. The first Brillouin zone is shown with red square and the irreducible Brillouin zone with the symmetry points $\Gamma = (0, 0)$, $X = (0, \frac{\pi}{a})$ and $M = (\frac{\pi}{a}, \frac{\pi}{a})$. The path to calculate band structure is taken as $\Gamma \rightarrow X \rightarrow M \rightarrow \Gamma$.

For the calculation of the band structure, we need a minimum calculation cell, that will give us all information about the lattice. This minimum cell can be formed by a primitive reciprocal lattice vector defined as the first Brillouin zone. So the solutions of the all eigenvalue equations are the same as the solutions at the first Brillouin zone.

For example in Fig. (2.4) we see the square lattice of 2D perfect Photonic Crystal. Here the red square shows the Brillouin zone. But for calculation of the band diagram we will solve the eigenvalue equation at the irreducible Brillouin zone, that is where the triangular wedge exists. Because the rest of the Brillouin zone can be formed from the irreducible Brillouin zone by rotational symmetry. a set of ω values which is given in Fig. (2.5) for TM-modes and TE-modes.

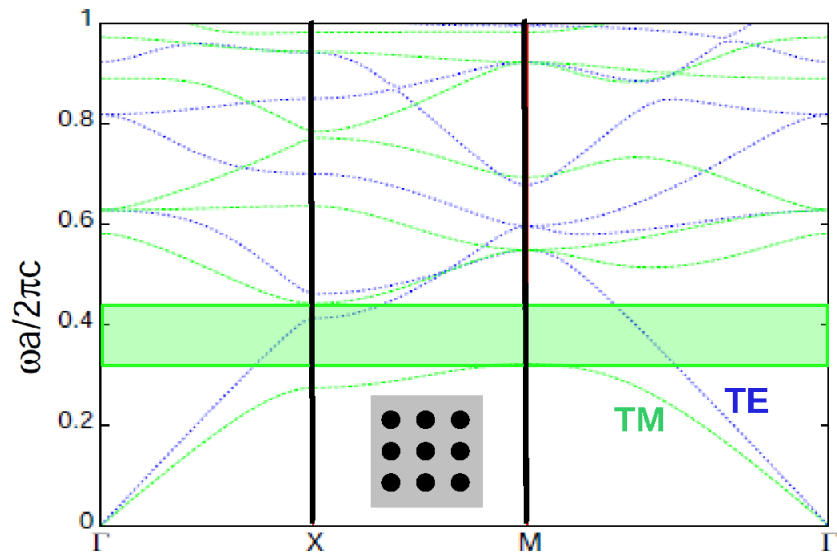


Figure 2.5. The TE and TM modes for a perfect 2D square lattice.

In Fig. (2.5) frequency is expressed as a dimensionless ratio $\omega a / 2\pi c$. The band structure shows that there is a band gap for the TM polarization, coloured with green, but there is no band gap for the TE polarization.

CHAPTER 3

FINITE DIFFERENCE TIME DOMAIN METHOD

In this chapter we will give an overview of Finite Difference Time Domain Method (FDTD) , which is used as the simulation technique in this thesis.

In 1966 Yee Yee et al. (1966) described the FDTD numerical technique for solving Maxwell's curl equations by discretization of the equations in space and time on grids. Today the FDTD method is one of the most useful methods for investigating the field distribution in complicated photonic crystal based devices with non-uniform refractive index distribution.

The FDTD method involves discretization of the space, which means replacing the continuum by a discrete set of nodes. Then the derivatives of Maxwell's equations are replaced by finite differences. The numerical solution depends on the permittivity distribution, which determines optical properties of the photonic crystals, and on the initial and boundary conditions. Setting all these terms, the field distribution can be computed beginning from the radiation source.

3.1. Discretization of Maxwell's Equations

We want to derive Maxwell's equations in terms of finite differences. Maxwell's equations for the case of no dispersion, no absorption nor any source, are

$$\nabla \times \mathbf{E}(\mathbf{r}, t) = -\frac{1}{c} \frac{\partial \mathbf{B}(\mathbf{r}, t)}{\partial t}, \quad (3.1)$$

$$\nabla \times \mathbf{H}(\mathbf{r}, t) = \frac{1}{c} \frac{\partial \mathbf{D}(\mathbf{r}, t)}{\partial t}. \quad (3.2)$$

We will write the equations in the vector components for $\mathbf{E}(\mathbf{r}, t)$ and $\mathbf{H}(\mathbf{r}, t)$ as follows,

$$\begin{aligned} \frac{\partial E_z}{\partial y} - \frac{\partial E_y}{\partial z} &= -\frac{1}{c} \frac{\partial B_x}{\partial t} \\ \frac{\partial E_x}{\partial z} - \frac{\partial E_z}{\partial x} &= -\frac{1}{c} \frac{\partial B_y}{\partial t} \\ \frac{\partial E_y}{\partial x} - \frac{\partial E_x}{\partial y} &= -\frac{1}{c} \frac{\partial B_z}{\partial t} \end{aligned} \quad (3.3)$$

$$\begin{aligned}
\frac{\partial H_z}{\partial y} - \frac{\partial H_y}{\partial z} &= \frac{1}{c} \frac{\partial D_x}{\partial t} \\
\frac{\partial H_x}{\partial z} - \frac{\partial H_z}{\partial x} &= \frac{1}{c} \frac{\partial D_y}{\partial t} \\
\frac{\partial H_y}{\partial x} - \frac{\partial H_x}{\partial y} &= \frac{1}{c} \frac{\partial D_z}{\partial t}
\end{aligned} \tag{3.4}$$

In two dimensions, we must make a choice between two kinds of modes; the TM mode, which consists of \mathbf{E}_z , \mathbf{H}_x , \mathbf{H}_y or the TE mode, which consists of \mathbf{H}_z , \mathbf{E}_x , \mathbf{E}_y . We will illustrate the method using the TM mode. We will make discretization of the space so we replace all partial derivatives by finite differences.

$$\frac{\partial}{\partial x} \approx \frac{\Delta}{\Delta x}, \quad \frac{\partial}{\partial y} \approx \frac{\Delta}{\Delta y}, \quad \frac{\partial}{\partial z} \approx \frac{\Delta}{\Delta z}.$$

Now we will change the derivatives by differences in Equations (3.3) and (3.4). and use the constitutive equations: $\mathbf{D} = \epsilon \mathbf{E}$ and $\mathbf{B} = \mu \mathbf{H}$. Also for convenience we will present calculations for the TM mode, so we let $D_x = D_y = H_z = 0$. Thus, Eqs. (3.3) and (3.4) are reduced to:

$$\begin{aligned}
\frac{\Delta E_z}{\Delta y} &= -\frac{\mu}{c} \frac{\Delta H_x}{\Delta t} \\
\frac{\Delta E_z}{\Delta x} &= \frac{\mu}{c} \frac{\Delta H_y}{\Delta t} \\
\frac{\Delta H_y}{\Delta x} - \frac{\Delta H_x}{\Delta y} &= \frac{\epsilon}{c} \frac{\Delta E_z}{\Delta t}
\end{aligned} \tag{3.5}$$

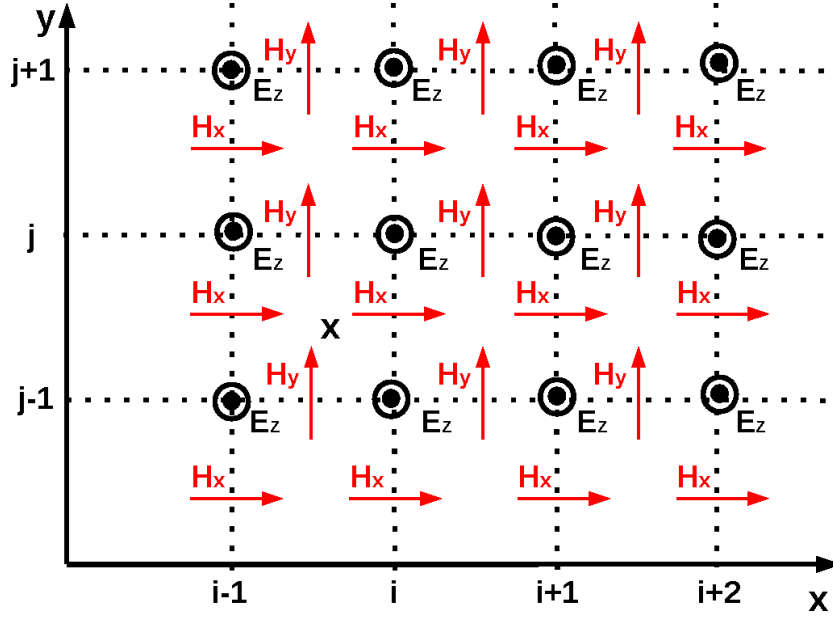


Figure 3.1. 2D computation region for TM modes

In Fig. (3.1), we show 2D computation region for TM modes. According to this interleaving the Maxwell's equations will be calculated in each cell, so the fields intensity will be found in each cell. Using the Yee cell we write;

$$-\frac{E_z^{n+\frac{1}{2}}(i, j+1) - E_z^{n+\frac{1}{2}}(i, j)}{\Delta y} = \frac{\mu(i, j+\frac{1}{2})}{c} \frac{H_x^{n+1}(i, j+\frac{1}{2}) - H_x^n(i, j+\frac{1}{2})}{\Delta t} \quad (3.6)$$

$$\frac{E_z^{n+\frac{1}{2}}(i+1, j) - E_z^{n+\frac{1}{2}}(i, j)}{\Delta x} = \frac{\mu(i+\frac{1}{2}, j)}{c} \frac{H_y^{n+1}(i+\frac{1}{2}, j) - H_y^n(i+\frac{1}{2}, j)}{\Delta t} \quad (3.7)$$

$$\frac{\epsilon(i, j)}{c} \frac{E_z^{n+\frac{1}{2}}(i, j) - E_z^{n-\frac{1}{2}}(i, j)}{\Delta t} = \left(\frac{H_y^n(i+\frac{1}{2}, j) - H_y^n(i-\frac{1}{2}, j)}{\Delta x} \right) - \left(\frac{H_x^n(i, j+\frac{1}{2}) - H_x^n(i, j-\frac{1}{2})}{\Delta y} \right) \quad (3.8)$$

Here we separated time n and space i, j in order to interleave Maxwell's equations in space and time. Time index is n , which means $t = n\Delta t$ and $n+1$ represents one time step later. Δx and Δy are space increments in the (x, y) directions, and i, j represents the coordinate values $x = i\Delta x, y = j\Delta y$. Then we take the central difference approximation for both n and i, j

derivatives.

Let's derive the recursion equations for E_z , H_x and H_y components using the above equations;

$$\begin{aligned}
E_z^{n+\frac{1}{2}}(i, j) &= E_z^{n-\frac{1}{2}}(i, j) \\
&+ \frac{c}{\epsilon(i, j)} \frac{\Delta t}{\Delta x} \left(H_y^n(i + \frac{1}{2}, j) - H_y^n(i - \frac{1}{2}, j) \right) \\
&- \frac{c}{\epsilon(i, j)} \frac{\Delta t}{\Delta y} \left(H_x^n(i, j + \frac{1}{2}) - H_x^n(i, j - \frac{1}{2}) \right)
\end{aligned} \tag{3.9}$$

$$\begin{aligned}
H_x^{n+1}(i, j + \frac{1}{2}) &= H_x^n(i, j + \frac{1}{2}) \\
&+ \frac{c}{\mu(i, j + \frac{1}{2})} \frac{\Delta t}{\Delta y} \left(E_z^{n+\frac{1}{2}}(i, j) - E_z^{n+\frac{1}{2}}(i, j + 1) \right)
\end{aligned} \tag{3.10}$$

$$\begin{aligned}
H_y^{n+1}(i + \frac{1}{2}, j) &= H_y^n(i + \frac{1}{2}, j) \\
&+ \frac{c}{\mu(i + \frac{1}{2}, j)} \frac{\Delta t}{\Delta x} \left(E_z^{n+\frac{1}{2}}(i + 1, j) - E_z^{n+\frac{1}{2}}(i, j) \right)
\end{aligned} \tag{3.11}$$

By using (3.9)-(3.11) we can find E_z , H_x and H_y components for any lattice point or at any time starting from the initial values and for the next points using the previous values.

This approach can be applied to 3D case. The significant point is that according to Courant stability condition Δt can be at most $\Delta t = \Delta x/(c/n)$ and $\Delta t = \Delta y/(c/n)$, where n is the smallest refractive index in the computational domain.

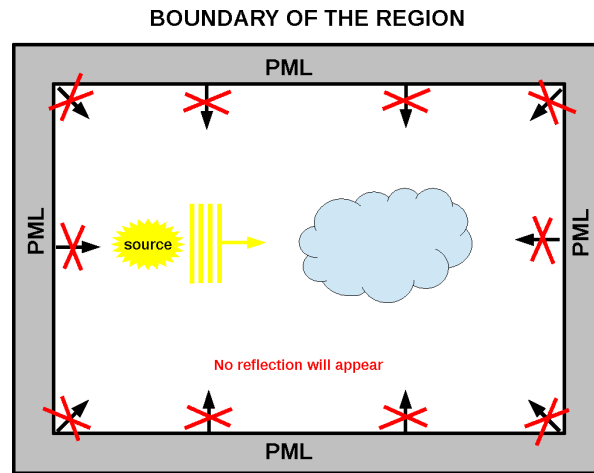


Figure 3.2. FDTD simulation region with perfectly matched layer (PML). PML absorbs electromagnetic waves at the boundaries without reflections.

The numerical solutions can be simplified by using a finite computation domain with suitable numerical boundary conditions. In this thesis, we use perfectly matched layer (PML) Berenger (1994) boundary conditions which absorbs electromagnetic waves at the boundaries without reflections. The Fig. (3.2) shows PML layer.

In the computation domain between transition from one dielectric material to another dielectric material we use average dielectric constant value, which takes the average of the dielectric constants at the transitions. Of course, resolution or the number of cells in the Yee lattice must be enough to give correct results.

FDTD is a time-domain technique. By using this method we can find \mathbf{E} fields and \mathbf{H} fields in the computational domain. Also this method provides animation displays of the electromagnetic fields, which helps us to understand the designed model. In this thesis we used the freely available MEEP software (MIT Electromagnetic Equation Propagation) for FDTD simulations, which can be accessed from: <http://ab-initio.mit.edu/wiki/index.php/Meep>.

CHAPTER 4

DIELECTRIC WAVEGUIDE SLABS

Dielectric waveguide slabs are the easiest structures to describe mathematically, because of their simple geometry. Therefore, as a preparation to study photonic crystal waveguide slabs, we start by dielectric waveguide slabs.

Dielectric waveguide slabs consist of a thin guiding layer sandwiched between two semi-infinite bounded media. Usually, the refractive index of the guiding layer must be greater than the bounding media for the occurrence of total internal reflection. Also the guiding layer, R_z , is at the order of a wavelength.

If the two bounding media are identical then dielectric slab is called the symmetric waveguide slab ($n_1 = n_3$). If two bounding media are not identical then waveguide called asymmetric waveguide slab.

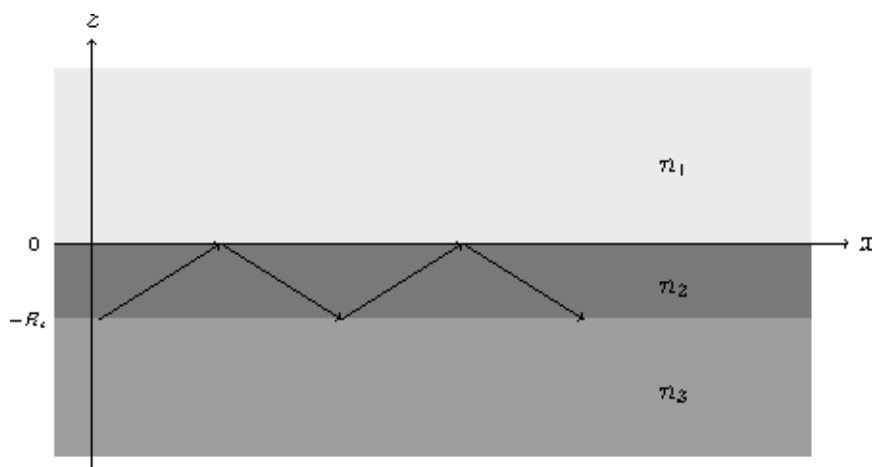


Figure 4.1. Dielectric waveguide slab.

The Fig. (4.1) shows a schema of dielectric waveguide slab. In the figure, R_z is the thickness of the guiding layer, n_1 is the refractive index of the upper cladding, n_3 is the refractive index of the lower cladding and n_2 is the refractive index of the guiding layer. The slab is infinitely extended in the xy-plane. Light propagates in the x-direction.

In this chapter we will give mathematical derivation of confined modes for symmetric

and asymmetric waveguide slabs. In order to obtain these confined modes of waveguide slabs, Maxwell's equations must be solved. Maxwell's equations in homogeneous media are equation of the plane waves. So we can solve the problem writing the plane wave solutions for each partition and matching the boundary conditions. The calculations will be derived both transverse electric and transverse magnetic modes of the propagation.

4.1. SYMMETRIC DIELECTRIC WAVEGUIDE SLABS

The simplest optical waveguides are the symmetric dielectric slab as shown in Fig. (4.2);

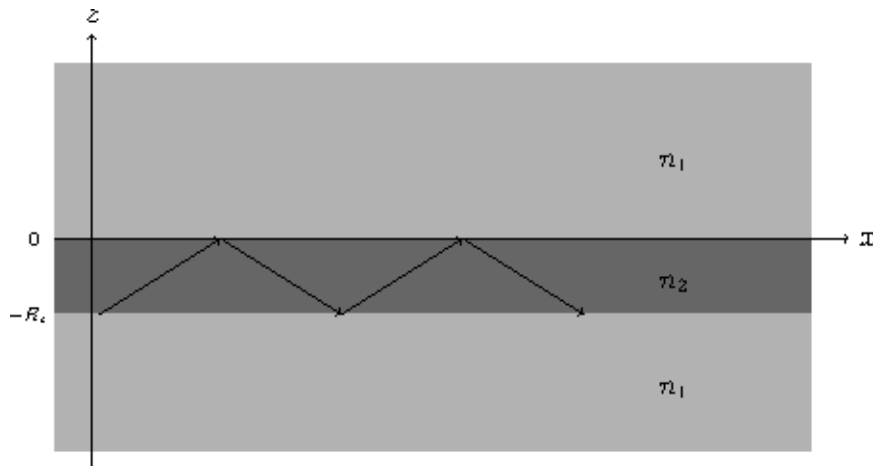


Figure 4.2. Symmetric dielectric waveguide slab.

The following equation describes the index profile of the symmetric dielectric waveguide slab:

$$n(z) = \begin{cases} n_2, & -R_z < z < 0 \\ n_1, & \text{otherwise} \end{cases} \quad (4.1)$$

where R_z is the thickness of the core, n_2 is the refractive index of the core and n_1 is the refractive index of the bounding media. As mentioned above to support confined modes the refractive index of core must be greater than the cladding ($n_2 > n_1$). Now our task is to find these confined modes.

To obtain these confined modes of waveguide slab, Maxwell's equations can be written in the form;

$$\nabla \times \mathbf{H} = i\omega\epsilon_0 n^2 \mathbf{E} \quad (4.2)$$

$$\nabla \times \mathbf{E} = -i\omega\mu_0 \mathbf{H} \quad (4.3)$$

where n is given in Equation (4.1)

The waveguide slab is homogeneous along the x -direction so we search solutions in the form;

$$\mathbf{E} = \mathbf{E}_m(z)e^{i(\omega t - \beta x)} \quad (4.4)$$

$$\mathbf{H} = \mathbf{H}_m(z)e^{i(\omega t - \beta x)} \quad (4.5)$$

where β is the x component of the wave-vector, $\mathbf{E}_m(z)$ and $\mathbf{H}_m(z)$ are wave functions and m is the mode number.

Now we substitute (4.4) and (4.5) into (4.2) and (4.3). We accept no variation in y direction, so that $\frac{\partial}{\partial y} = 0$. After differentiating and cancelling out the exponential factor we get the set of equations;

$$\frac{\partial E_y}{\partial z} = i\omega\mu_0 H_x \quad (4.6)$$

$$i\beta E_z + \frac{\partial E_x}{\partial z} = -i\omega\mu_0 H_y \quad (4.7)$$

$$\beta E_y = \omega\mu_0 H_z \quad (4.8)$$

$$-\frac{\partial H_y}{\partial z} = i\omega\epsilon_0 n^2 E_x \quad (4.9)$$

$$i\beta H_z + \frac{\partial H_x}{\partial z} = i\omega\epsilon_0 n^2 E_y \quad (4.10)$$

$$-\beta H_y = \omega\epsilon_0 n^2 E_z \quad (4.11)$$

From this first order coupled system of equations we can find two decoupled second order equations

First we use (4.6), (4.8) and (4.10), they yield

$$\frac{\partial E_y}{\partial z} = i\omega\mu_0 H_x \quad (4.12)$$

$$\beta E_y = \omega\mu_0 H_z \quad (4.13)$$

$$i\omega\epsilon_0 n^2 E_y = i\beta H_z + \frac{\partial H_x}{\partial z} \quad (4.14)$$

From these set of equations one can see that, if E_y is known, then H_x and H_z can be easily found. If we substitute (4.12) and (4.13) into (4.14) we get the wave equation for E_y

$$\frac{\partial^2 E_y}{\partial z^2} + \left(\frac{\omega^2 n^2}{c^2} - \beta^2 \right) E_y = 0 \quad (4.15)$$

where $c = 1/\sqrt{\mu_0\epsilon_0}$.

As a second set we use (4.7), (4.9) and (4.11),

$$-\frac{\partial H_y}{\partial z} = i\omega\epsilon_0 n^2 E_x \quad (4.16)$$

$$-\beta H_y = \omega\epsilon_0 n^2 E_z \quad (4.17)$$

$$-i\omega\mu_0 H_y = i\beta E_z + \frac{\partial E_x}{\partial z} \quad (4.18)$$

From this set of equations one can see that, if H_y is known, then H_x and H_z can be easily found. If we substitute (4.16) and (4.17) into (4.18) we get wave equation for H_y

$$\frac{\partial^2 H_y}{\partial z^2} + \left(\frac{\omega^2 n^2}{c^2} - \beta^2 \right) H_y = 0 \quad (4.19)$$

where $c = 1/\sqrt{\mu_0\epsilon_0}$.

These two sets can be classified as TE and TM modes. The first couple represents TE modes. They have their electric field perpendicular to plane of propagation (xz-plane) that means they have the field components E_y , H_x and H_z . The second couple represents TM modes. They have their magnetic field perpendicular to plane of propagation with the field components H_y , E_x and E_z .

Now for each media we will solve (4.15) and (4.19) by applying the boundary condi-

tions. First we will use the following boundary condition; the tangential components of the field vectors at each interfaces must satisfy the continuity condition. Second we will use another boundary condition for guided modes; that is the field amplitude of guided modes must vanish at $z = \pm\infty$.

The propagation constant β specifies whether the field varies sinusoidally or exponentially and to get confined modes the field amplitude must decrease exponentially outside the core. For these reasons the following conditions must hold

$$\begin{cases} \left(\frac{\omega n_2}{c}\right)^2 - \beta^2 > 0, & -R_z < z < 0, \\ \left(\frac{\omega n_1}{c}\right)^2 - \beta^2 < 0, & \text{otherwise.} \end{cases} \quad (4.20)$$

For the rest of the section we will find the confined modes whose β satisfies these above conditions for guided TE modes and TM modes.

4.1.1. Guided TE Modes

The guided TE modes can be find by solving Equation (4.15) with boundary conditions for each interfaces of the waveguide. The solution of Eq. (4.15) has the form

$$E_y = E_m(z)e^{i(\omega t - \beta x)} \quad (4.21)$$

where for each region $E_m(z)$ can be written as

$$E_m(z) = \begin{cases} Ae^{-\delta z}, & z \geq 0 \\ A \cos \kappa z + B \sin \kappa z, & 0 \geq z \geq -R_z \\ (A \cos \kappa R_z - B \sin \kappa R_z)e^{\delta(z+R_z)}, & z \leq -R_z \end{cases} \quad (4.22)$$

The above solution given by Eq. (4.22) clearly obey the boundary condition, which states the tangential component of E_y must be continuous at the interfaces at $z = 0$ and

$z = -R_z$, where A,B are the constants and the parameters δ and κ are

$$\delta = \left[\beta^2 - \left(\frac{\omega n_1}{c} \right)^2 \right]^{1/2}, \quad (4.23)$$

$$\kappa = \left[\left(\frac{\omega n_2}{c} \right)^2 - \beta^2 \right]^{1/2}. \quad (4.24)$$

To complete the set, we need to find H_x and H_z . These components in terms of E_y are given as follows,

$$H_x = \frac{-i}{\mu_0 \omega} \frac{\partial E_y}{\partial z}, \quad (4.25)$$

$$H_z = \frac{\beta}{\mu_0 \omega} E_y. \quad (4.26)$$

Since H_z is a constant times E_y we don't need to calculate H_z because we already calculated E_y . But we need to calculate H_x . The solution of Eq. (4.25) has the form,

$$H_x = H_m(z) e^{[i(\omega t - \beta x)]} \quad (4.27)$$

where for each region $H_m(z)$ can be written as

$$H_m(z) = \begin{cases} \left(\frac{i\delta}{\mu_0 \omega} \right) A e^{-\delta z}, & z \geq 0 \\ \left(\frac{i\kappa}{\mu_0 \omega} \right) (A \sin \kappa z - B \cos \kappa z), & 0 \geq z \geq -R_z \\ \left(\frac{-i\delta}{\mu_0 \omega} \right) (A \cos \kappa R_z - B \sin \kappa R_z) e^{\delta(z+R_z)}, & z \leq -R_z \end{cases} \quad (4.28)$$

Now to satisfy the boundary condition we match the functions at the above equation at the interfaces $z = 0$ and $z = -R_z$. But it is not evident that the solutions obey the boundary conditions. For this reason we have to make an extra job. We apply the boundary conditions which lead to

$$\begin{aligned}\delta\mathbf{A} + \kappa\mathbf{B} &= 0, \\ (\kappa \sin \kappa R_z - \delta \cos \kappa R_z)\mathbf{A} + (\kappa \cos \kappa R_z + \delta \sin \kappa R_z)\mathbf{B} &= 0,\end{aligned}$$

This homogeneous system has non-trivial solution only if determinant vanishes;

$$\delta(\kappa \cos \kappa R_z + \delta \sin \kappa R_z) - \kappa(\kappa \sin \kappa R_z - \delta \cos \kappa R_z) = 0, \quad (4.29)$$

or

$$(2\delta\kappa) \cos \kappa R_z + (\delta^2 - \kappa^2) \sin \kappa R_z = 0, \quad (4.30)$$

which leads to,

$$\tan \kappa R_z = \frac{2\kappa\delta}{(\kappa^2 - \delta^2)}. \quad (4.31)$$

We can write the above equation using the double angle formula for tangent in the next form

$$\tan(2\kappa R_z/2) = \frac{2 \tan \kappa R_z/2}{1 - \tan^2 \kappa R_z/2} = \frac{2\kappa\delta}{(\kappa^2 - \delta^2)}. \quad (4.32)$$

which leads to the second order algebraic equation

$$\frac{\delta}{\kappa} \tan^2(\kappa R_z/2) - \left(\frac{\delta^2}{\kappa^2} - 1\right) \tan(\kappa R_z/2) - \frac{\delta}{\kappa} = 0 \quad (4.33)$$

with the solutions

$$\tan(\kappa R_z/2) = \frac{\delta}{\kappa} \quad (4.34)$$

and

$$\tan(\kappa R_z/2) = -\frac{\kappa}{\delta}. \quad (4.35)$$

We can substitute for $\tilde{\kappa} = \frac{1}{2}R_z\kappa$ and for $\tilde{\delta} = \frac{1}{2}R_z\delta$ and rewrite the above equations in the next form;

1. For even TE modes;

$$\tan(\tilde{\kappa}) = \frac{\tilde{\delta}}{\tilde{\kappa}} \quad (4.36)$$

2. For odd TE modes;

$$\tan(\tilde{\kappa}) = -\frac{\tilde{\kappa}}{\tilde{\delta}}, \quad (4.37)$$

Eq. (4.36) and Eq. (4.37) are the eigenvalue equations for symmetric slab waveguides for even and odd modes respectively.

Now we have two implicit equations, (4.36) and (4.37). We will solve graphically Eq. (4.37) to show the structure of the solution. For a given value of $\tilde{\delta}$, the solutions of Eq. (4.37) yields several values for $\tilde{\kappa}$. Graphical solution of the Eq. (4.37) is shown in Fig. (4.3). In the plotted graph, the solutions are the intersections of the functions $\tan(\tilde{\kappa})$ and $-\tilde{\kappa}/\tilde{\delta}$.

To find the roots let's define the next iteration

$$\tilde{\kappa}_{n+1} = \tan^{-1}\left(-\frac{\tilde{\kappa}_n}{\tilde{\delta}_n}\right), \quad (n = 0, 1, 2, 3\dots), \quad (4.38)$$

with the initial guesses $\tilde{\kappa}_0 = n\pi$. By this way for each given $\tilde{\delta}$ we get set of solutions for $\tilde{\kappa}$. To see the confined modes our aim is to calculate ω and β . ω and β can be picked out from the below equations;

$$\tilde{\delta} = \frac{1}{2}R_z \left[\beta^2 - \left(\frac{\omega n_1}{c}\right)^2 \right]^{1/2} \quad (4.39)$$

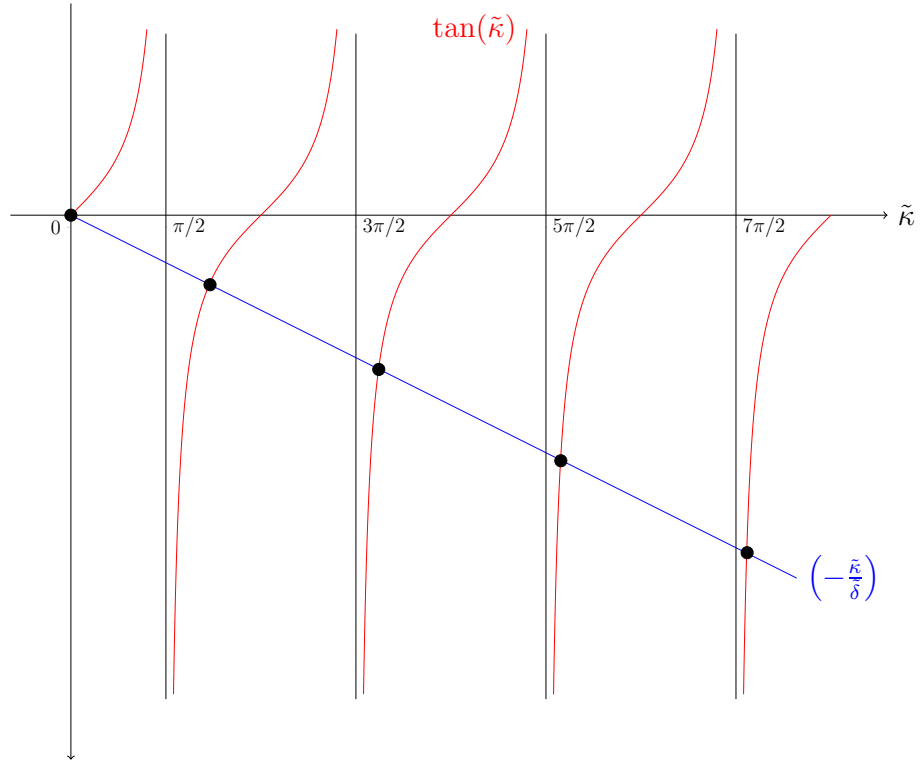


Figure 4.3. For odd TE modes graphical roots.

$$\tilde{\kappa} = \frac{1}{2}R_z \left[\left(\frac{\omega n_2}{c} \right)^2 - \beta^2 \right]^{1/2} \quad (4.40)$$

ω and β are equal to the next form;

$$\left(\frac{\omega \frac{1}{2}R_z}{c} \right)^2 = \frac{\tilde{\kappa}^2 + \tilde{\delta}^2}{n_2^2 - n_1^2}, \quad (4.41)$$

$$\left(\frac{\beta \frac{1}{2}R_z}{c} \right)^2 = \frac{n_1^2 \tilde{\kappa}^2 + n_2^2 \tilde{\delta}^2}{n_2^2 - n_1^2}. \quad (4.42)$$

As a result for every given $\tilde{\delta}$, we get the solution set for $\tilde{\kappa}$ by using the iteration given by Eq. (4.38) and use the values of $n_1, n_2, R_z, c, \tilde{\delta}, \tilde{\kappa}$ and (4.41) and (4.42) we can find ω and β .

The similar derivation can be done also for Eq. (4.36), for a given $\tilde{\delta}$ yielding several

values for $\tilde{\kappa}$. To examine this we use the next iteration for a given $\tilde{\delta}$ with the initial guesses $\tilde{\kappa}_0 = n\pi$, ($n = 0, 1, 2, 3\dots$)

$$\tilde{\kappa}_{n+1} = \tan^{-1} \left(\frac{\tilde{\delta}}{\tilde{\kappa}_n} \right), \quad (4.43)$$

By this way for each given $\tilde{\delta}$ we get the set of solutions for $\tilde{\kappa}$. Again by using (4.41) and (4.42) the confined modes ω and β can be found in terms of $\tilde{\kappa}$ and $\tilde{\delta}$.

4.1.2. Guided TM Modes

The guided *TM* modes can be find by solving Eq. (4.19) with boundary conditions for each interfaces of the waveguide. The solution of Eq. (4.19) has the form

$$H_y = H_m(z)e^{i(\omega t - \beta x)} \quad (4.44)$$

where for each region $H_m(z)$ can be written as

$$H_m(z) = \begin{cases} C e^{-\delta z}, & z \geq 0 \\ C \cos \kappa z + D \sin \kappa z, & 0 \geq z \geq -R_z \\ (C \cos \kappa R_z - D \sin \kappa R_z) e^{\delta(z+R_z)}, & z \leq -R_z \end{cases} \quad (4.45)$$

The above solution given by Eq. (4.45) clearly obey the boundary condition, which states the tangential component of H_y must be continuous at the interfaces at $z = 0$ and $z = -R_z$, where C, D are the constants and the parameters δ and κ are previously defined at Eq. (4.23) and Eq. (4.24) respectively.

To complete the set, we need to find E_x and E_z . These components in terms of H_y are given as follows,

$$E_x = \frac{i}{\epsilon_0 \omega n^2} \frac{\partial H_y}{\partial z} \quad (4.46)$$

$$E_z = \frac{-\beta}{\epsilon_0 \omega n^2} H_y. \quad (4.47)$$

Since E_z is a constant times H_y we don't need to calculate E_z because we already calculated H_y . But we need to calculate E_x . The solution of Eq. (4.46) has the form

$$E_x = E_m(z)e^{i(\omega t - \beta x)} \quad (4.48)$$

where for each region $E_m(z)$ can be written as

$$E_m(z) = \begin{cases} \left(\frac{-i\delta}{\epsilon_0\omega n_1^2}\right)(C e^{-\delta z}), & z \geq 0 \\ \left(\frac{i\kappa}{\epsilon_0\omega n_2^2}\right)(-C \sin \kappa z + D \cos \kappa z), & 0 \geq z \geq -R_z \\ \left(\frac{i\delta}{\epsilon_0\omega n_1^2}\right)(C \cos \kappa R_z - D \sin \kappa R_z)e^{\delta(z+R_z)}, & z \leq -R_z \end{cases} \quad (4.49)$$

Now to satisfy the boundary condition we match the functions at the above equation at the interfaces $z = 0$ and $z = -R_z$. But it is not evident that the solutions obey the boundary conditions. For this reason we have to make an extra job. We apply the boundary conditions which lead to

$$\begin{aligned} \frac{\delta}{n_1^2}C + \frac{\kappa}{n_2^2}D &= 0, \\ \left(\frac{\kappa}{n_2^2} \sin \kappa R_z - \frac{\delta}{n_1^2} \cos \kappa R_z\right) C + \left(\frac{\kappa}{n_2^2} \cos \kappa R_z + \frac{\delta}{n_1^2} \sin \kappa R_z\right) D &= 0. \end{aligned}$$

This homogeneous linear system has non-trivial solution only if determinant vanishes;

$$\frac{\delta}{n_1^2} \left(\frac{\kappa}{n_2^2} \cos \kappa R_z + \frac{\delta}{n_1^2} \sin \kappa R_z\right) - \frac{\kappa}{n_2^2} \left(\frac{\kappa}{n_2^2} \sin \kappa R_z - \frac{\delta}{n_1^2} \cos \kappa R_z\right) = 0, \quad (4.50)$$

or

$$\left(\frac{2\delta\kappa}{n_1^2 n_2^2}\right) \cos \kappa R_z + \left(\frac{\delta^2}{n_1^4} - \frac{\kappa^2}{n_2^4}\right) \sin \kappa R_z = 0, \quad (4.51)$$

which leads to,

$$\tan \kappa R_z = \frac{2 \left(\frac{\delta}{n_1^2}\right) \left(\frac{\kappa}{n_2^2}\right)}{\left(\frac{\kappa}{n_2^2}\right)^2 - \left(\frac{\delta}{n_1^2}\right)^2}. \quad (4.52)$$

We can write the above equation using the double angle formula for tangent and that leads a second order algebraic equation with the solutions in the next form

1. For even TM modes;

$$\tan(\tilde{\kappa}) = \frac{\tilde{\delta}n_2^2}{\tilde{\kappa}n_1^2} \quad (4.53)$$

2. For odd TM modes;

$$\tan(\tilde{\kappa}) = -\frac{\tilde{\kappa}n_1^2}{\tilde{\delta}n_2^2}, \quad (4.54)$$

Here we substituted for $\tilde{\kappa} = \frac{1}{2}R_z\kappa$ and for $\tilde{\delta} = \frac{1}{2}R_z\delta$. Then Eq. (4.53) and Eq. (4.54) give the eigenvalue equations for symmetric slab waveguides for even and odd TM modes respectively.

Now we have two implicit equations, (4.53) and (4.54). As mentioned previously a result for every given $\tilde{\delta}$ yields several values for $\tilde{\kappa}$. The used iteration method to find guided TE modes can be used to find guided TM modes.

In the next subsection we present the mode profiles for confined modes and radiation modes explicitly.

4.1.3. Mode Profiles of Symmetric Dielectric Waveguide Slab

We can find the band diagram for symmetric waveguide slab as in Fig. (4.4). In the figure the red line is $\omega = \frac{c}{n_1}\beta$, the green line is $\omega = \frac{c}{n_2}\beta$.

The confined modes appear in the area between the red and the green lines. The modes above the red line are radiation modes. The dashed lines are TE modes. The first dashed line is even TE mode and the second dashed line is odd TE mode. The continuous solid lines are TM modes. The first continuous line is even TM mode and the second continuous line is odd TM mode.

Now, we want to show some examples of the mode profiles. To do this we chose a point on the x-axis $\beta a/2\pi = 0.6$ and we put a blue line along this point. The modes profiles of the examples chosen on the points which ones are intersections of this blue lines and modes.

As previously indicated the confined modes are under the red line. There are only 5 TE confined modes, shown with dashed lines and 5 TM confined modes, shown with

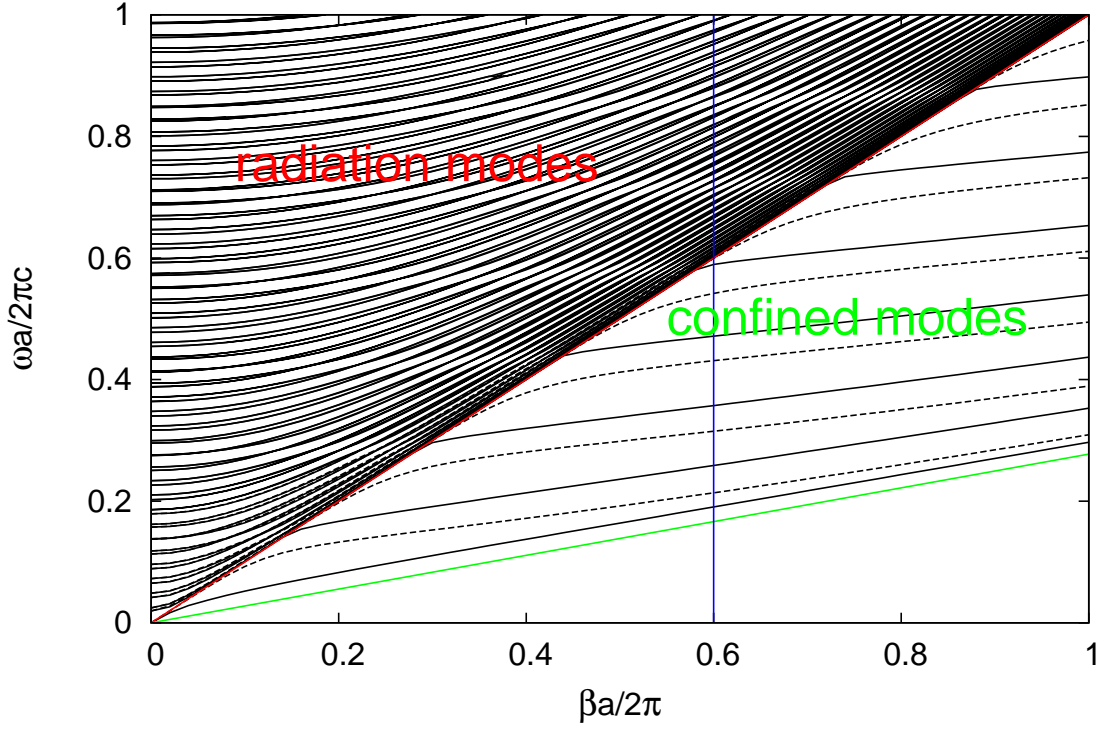


Figure 4.4. Band diagram of Symmetric Dielectric Waveguide Slab. Refraction indexes are $n_1 = 1$, $n_2 = 3.6$, $R_z = a$, a is a period of the cell, all cell is $41a$. The cell is taken in z -direction and light propagates in x -direction. The structure of the band diagram is shown in Fig. (4.2). The band diagram is calculated by using MPB program.

continuous solid lines. The mode profiles of the first 4 TE and TM confined modes are shown in Fig. (4.5) and Fig. (4.6), respectively. The vertical dashed lines on $z = -R_z$ and $z = 0$ represent the limits of the guiding layer. Here as mentioned before all confined modes are well confined in the guiding layer, but decrease exponentially outside the guiding layer, which is obvious in the both figures.

The radiation modes are above the red line. There are TE radiation modes and TM radiation modes. The mode profiles of the some TE and TM radiation modes are shown in Fig. (4.7) and Fig. (4.8), respectively. Again the vertical dashed lines on $z = -R_z$ and $z = 0$ represent the limits of the guiding layer. In this zone, radiation modes are not well confined in the guiding layer because they are not decreasing exponentially outside the guiding layer. Contrarily outside of the guiding layer modes exist, and due to the symmetrical structure, mode is symmetrical in the upper and lower slabs.

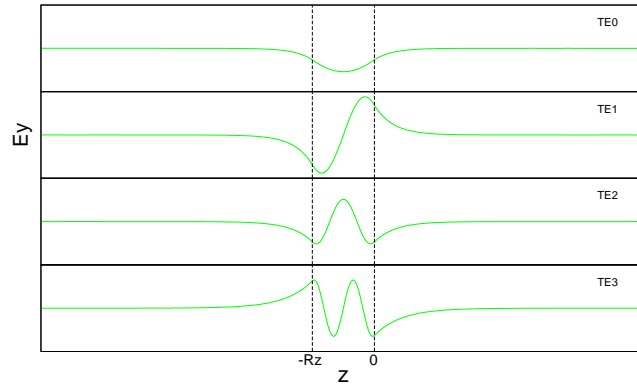


Figure 4.5. *TE* Confined Modes for Symmetric Dielectric Waveguide Slab. Y-axis shows E_y component of the electric field, and x-axis shows the z direction of the waveguide slab.

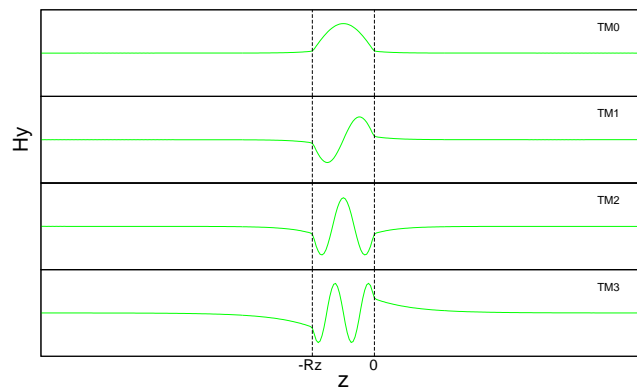


Figure 4.6. *TM* Confined Modes for Symmetric Dielectric Waveguide Slab. Y-axis shows H_y component of the magnetic field, and x-axis shows the z direction of the waveguide slab.

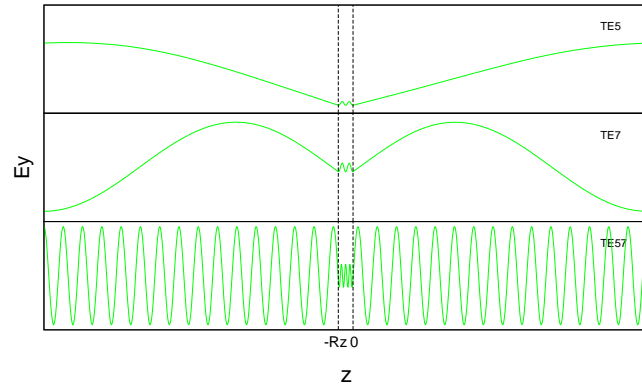


Figure 4.7. *TE* Radiation Modes for Symmetric Dielectric Waveguide Slab. Y-axis shows E_y component of the electric field, and x-axis shows the z direction of the waveguide slab.

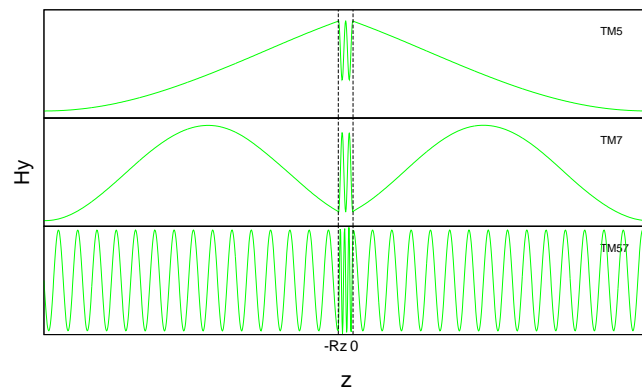


Figure 4.8. *TM* Radiation Modes for Symmetric Dielectric Waveguide Slab. Y-axis shows H_y component of the magnetic field, and x-axis shows the z direction of the waveguide slab.

4.2. ASYMMETRIC DIELECTRIC WAVEGUIDE SLABS

In integrated optic design, mostly waveguides are not symmetric. Therefore, to consider this case, we will study propagation of confined modes of asymmetric slab waveguide shown in Fig. (4.9)

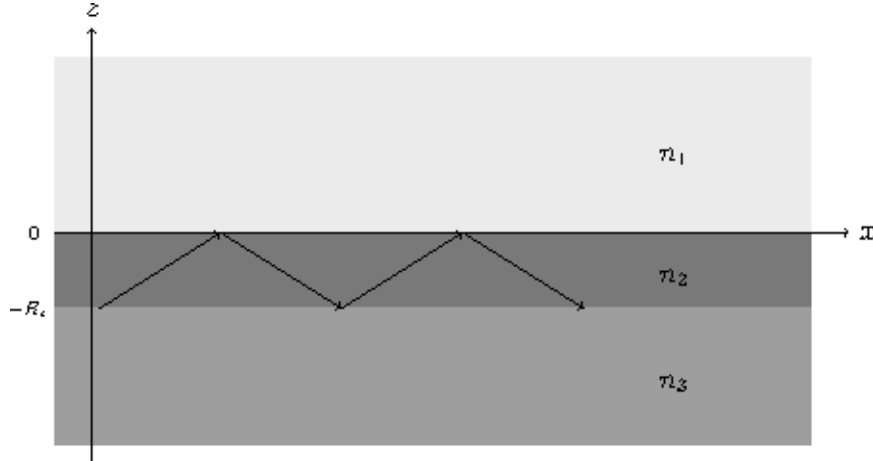


Figure 4.9. Asymmetric waveguide slab.

The index profile of the asymmetric slab waveguide is given by

$$n(z) = \begin{cases} n_1, & 0 < z \\ n_2, & -R_z < z < 0 \\ n_3, & z < -R_z \end{cases} \quad (4.55)$$

where R_z is the thickness of the core, n_2 is the refractive index of the core and n_1 and n_3 are the refractive indices of the upper and lower bounds respectively. To get guided modes, the refractive index of core must be greater than claddings. For our case we take $n_2 > n_3 > n_1$. Now our task is to find these guided modes.

The modes of the waveguide slab can be classified as TE and TM modes. TE modes have their electric field perpendicular to plane of propagation (xz -plane) with only have the field components E_y , H_x and H_z while TM modes have the field components H_y , E_x and E_z

4.2.1. Guided TE Modes

The guided TE modes can be find by solving Eq. (4.15) for E_y component. Since we can get H_x and H_z interns of E_y component using (4.2) and (4.3) (for the case $\partial/\partial y = 0$, $H_y = 0$, $E_x = 0$ and $E_z = 0$), we can determine all TE modes. The solution of Eq. (4.15) for E_y component is in the form of

$$E_y = E_m(z)e^{i(\omega t - \beta x)} \quad (4.56)$$

where for each region $E_m(z)$ can be written as

$$E_m(z) = \begin{cases} Ae^{-\delta z}, & z \geq 0 \\ A \cos \kappa z + B \sin \kappa z, & 0 \geq z \geq -R_z \\ (A \cos \kappa R_z - B \sin \kappa R_z)e^{\delta(z+R_z)}, & z \leq -R_z \end{cases} \quad (4.57)$$

where A,B are the constants and the parameters κ , δ and γ are

$$\delta = \left[\beta^2 - \left(\frac{n_1 \omega}{c} \right)^2 \right]^{1/2} \quad (4.58)$$

$$\kappa = \left[\left(\frac{n_2 \omega}{c} \right)^2 - \beta^2 \right]^{1/2} \quad (4.59)$$

$$\gamma = \left[\beta^2 - \left(\frac{n_3 \omega}{c} \right)^2 \right]^{1/2} \quad (4.60)$$

H_x and H_z components in terms of E_y as follows,

$$H_x = \frac{-i}{\mu_0 \omega} \frac{\partial E_y}{\partial z} \quad \text{and} \quad H_z = \frac{\beta}{\mu_0 \omega} E_y. \quad (4.61)$$

To get solutions the tangential component of E_y and H_x must be continuous at the interfaces, where H_m for the solution of the equation $H_x = H_m(z)e^{i(\omega t - \beta x)}$ is given below;

$$H_m(z) = \begin{cases} \left(\frac{i\delta}{\mu_0 \omega} \right) A e^{-\delta z}, & z \geq 0 \\ \left(\frac{i\kappa}{\mu_0 \omega} \right) (A \sin \kappa z - B \cos \kappa z), & 0 \geq z \geq -R_z \\ \left(\frac{-i\gamma}{\mu_0 \omega} \right) (A \cos \kappa R_z - B \sin \kappa R_z) e^{\gamma(z+R_z)}, & z \leq -R_z \end{cases} \quad (4.62)$$

Now we match the magnitude and derivatives of the TE mode functions at the interfaces $z = 0$ and $z = -R_z$, which leads to

$$\begin{aligned}\delta\mathbf{A} + \kappa\mathbf{B} &= 0, \\ (\kappa \sin \kappa R_z - \gamma \cos \kappa R_z)\mathbf{A} + (\kappa \cos \kappa R_z + \gamma \sin \kappa R_z)\mathbf{B} &= 0,\end{aligned}$$

This homogeneous system has solution only if determinant vanishes;

$$\delta(\kappa \cos \kappa R_z + \gamma \sin \kappa R_z) - \kappa(\kappa \sin \kappa R_z - \gamma \cos \kappa R_z) = 0, \quad (4.63)$$

or

$$\cos \kappa R_z(\delta\kappa + \kappa\gamma) + \sin \kappa R_z(\delta\gamma - \kappa^2) = 0, \quad (4.64)$$

which leads to,

$$\tan \kappa R_z = \frac{\kappa(\delta + \gamma)}{(\kappa^2 - \delta\gamma)}. \quad (4.65)$$

The right hand side of the equation can be written as;

$$\frac{\kappa(\delta + \gamma)}{(\kappa^2 - \delta\gamma)} = \frac{(\kappa R_z)(\delta R_z + \gamma R_z)}{(\kappa R_z)^2 - (\delta R_z)(\gamma R_z)} \quad (4.66)$$

where δ , κ and γ given in (4.58), (4.59) and (4.60). This equation is the mode condition equation for TE modes, for a given set of refractive indices, n_1 , n_2 and n_3 and R_z . The same iteration method can be followed as the symmetric waveguide case to get (ω, β) .

4.2.2. Guided TM Modes

The guided TM modes can be calculated by a similar analysis. TM modes have the field components H_y , E_x and E_z .

$$H_y = H_m(z)e^{i(\omega t - \beta x)} \quad (4.67)$$

where for each region the continuity condition of H_y leads for $H_m(z)$

$$H_m(z) = \begin{cases} C e^{-\delta z}, & z \geq 0 \\ C \cos \kappa z + D \sin \kappa z, & 0 \geq z \geq -R_z \\ (C \cos \kappa R_z - D \sin \kappa R_z) e^{\gamma(z+R_z)}, & z \leq -R_z \end{cases} \quad (4.68)$$

where C,D are the constants and the parameters δ , κ and γ are given in (4.58), (4.59) and (4.60). Also E_x and E_z can be written interns of H_y as follows

$$E_x = \frac{i}{\epsilon_0 n^2 \omega} \frac{\partial H_y}{\partial z}, \quad \text{and} \quad E_z = \frac{-\beta}{\epsilon_0 n^2 \omega} H_y. \quad (4.69)$$

$E_x = E_m(z)e^{i(\omega t - \beta x)}$ at the two interfaces can be written as

$$E_m(z) = \begin{cases} \frac{-i\delta}{\epsilon_0 n_1^2 \omega} C e^{-\delta z}, & z \geq 0 \\ \frac{i\kappa}{\epsilon_0 n_2^2 \omega} (-C \sin \kappa z + D \cos \kappa z), & 0 \geq z \geq -R_z \\ \frac{i\gamma}{\epsilon_0 n_3^2 \omega} (C \cos \kappa R_z - D \sin \kappa R_z) e^{\gamma(z+R_z)}, & z \leq -R_z \end{cases} \quad (4.70)$$

Now we match the magnitude and derivatives of the TM mode functions at the interfaces $z = 0$ and $z = -R_z$, which leads to

$$\begin{aligned} \left(\frac{\delta}{n_1^2} \right) C + \left(\frac{\kappa}{n_2^2} \right) D &= 0, \\ \left(\frac{\kappa}{n_2^2} \sin \kappa R_z - \frac{\gamma}{n_3^2} \cos \kappa R_z \right) C + \left(\frac{\kappa}{n_2^2} \cos \kappa R_z + \frac{\gamma}{n_3^2} \sin \kappa R_z \right) D &= 0 \end{aligned} \quad (4.71)$$

This homogeneous system has solution only if determinant vanishes;

$$\left[\frac{\delta}{n_1^2} \left(\frac{\kappa}{n_2^2} \cos \kappa R_z + \frac{\gamma}{n_3^2} \sin \kappa R_z \right) \right] - \left(\frac{\kappa}{n_2^2} \left(\frac{\kappa}{n_2^2} \sin \kappa R_z - \frac{\gamma}{n_3^2} \cos \kappa R_z \right) \right) = 0 \quad (4.72)$$

or dividing to $\cos \kappa R_z$ we get,

$$\tan \kappa R_z = \frac{\kappa n_2^2 (\delta n_3^2 + \gamma n_1^2)}{(\kappa^2 n_1^2 n_3^2 - \delta \gamma n_2^4)}. \quad (4.73)$$

The right hand side of the equation can be written as;

$$\frac{\kappa(\delta + \gamma)}{(\kappa^2 - \delta\gamma)} = \frac{(\kappa R_z)(\delta R_z + \gamma R_z)}{(\kappa R_z)^2 - (\delta R_z)(\gamma R_z)} \quad (4.74)$$

where κ , δ and γ given in (4.58), (4.59), (4.60). This equation is the mode condition equation for TM modes, for a given set of refractive indices, n_1 , n_2 and n_3 and R_z . The same iteration method can be followed as the symmetric waveguide case to get (ω, β) .

4.2.3. Mode Profiles of Asymmetric Dielectric Waveguide Slab

We can find the band diagram for asymmetric waveguide slab as in Fig. (4.10). In the figure the red line is $\omega = \frac{c}{n_1}\beta$, the yellow line is $\omega = \frac{c}{n_3}\beta$ and the green line is $\omega = \frac{c}{n_2}\beta$.

The band diagram in the figure divided to three parts. Radiation modes, slab modes and finite number confined modes.

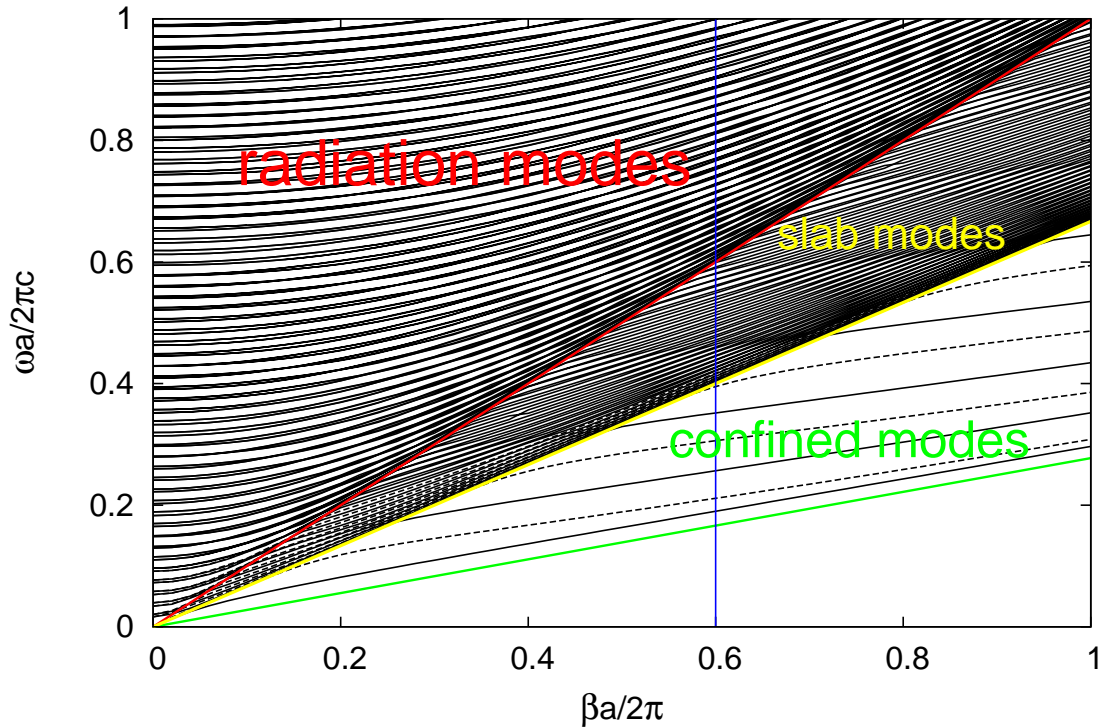


Figure 4.10. Band Diagram for Asymmetric Dielectric Waveguide Slab. Refraction indexes are $n_1 = 1$, $n_2 = 3.61$, $n_3 = 1.58$ $R_z = a$, a is a period of the cell. The length of the cell is $41a$. The cell is taken in z -direction and light propagates in x -direction.

Now, we want to show some examples of the mode profiles. To do this we chose a point on the x -axis $\beta a/2\pi = 0.6$ and we put a blue line along this point. The modes profiles of the examples chosen on the points which ones are intersections of this blue lines and modes.

The confined modes appear in the area between the green and the yellow lines. There are only 3 TE confined modes, shown with dashed lines and 3 TM confined modes, shown with continuous solid lines. The first dashed line is even TE mode and the second dashed line is odd TE mode. The continuous solid lines are TM modes. The first continuous line is even TM mode and the second continuous line is odd TM mode. The mode profiles of the first 3 TE and TM confined modes are shown in Fig. (4.11) and (4.12), respectively. The vertical dashed lines on $z = R_z$ and $z = 0$ represent the limits of the guiding layer. Here as mentioned before all confined modes are well confined in the guiding layer, but decrease exponentially outside the guiding layer, which is obvious in the both figures

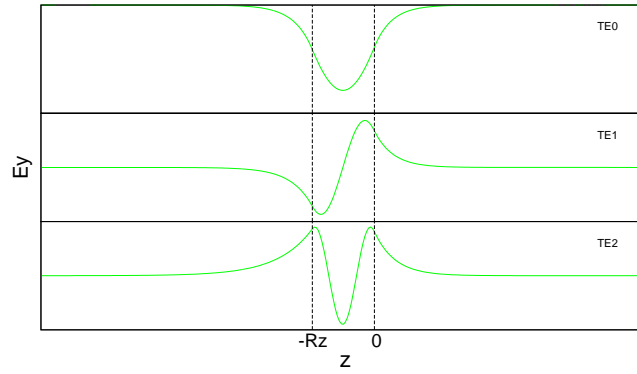


Figure 4.11. *TE* Confined Modes for Asymmetric Dielectric Waveguide Slab. Y-axis shows E_y component of the electric field, and x-axis shows the z direction of the waveguide slab.

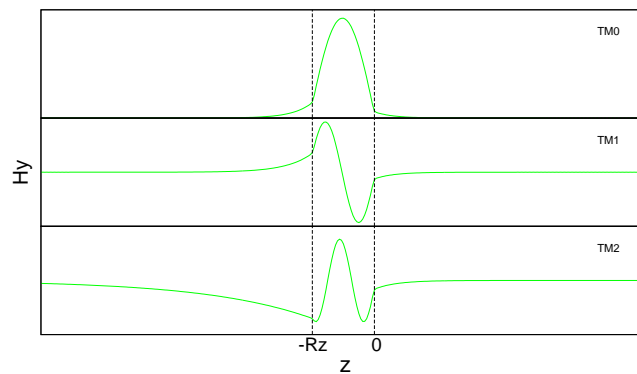


Figure 4.12. *TM* Confined Modes for Asymmetric Dielectric Waveguide Slab. Y-axis shows H_y component of the magnetic field, and x-axis shows the z direction of the waveguide slab.

The slab modes between the yellow and red lines. There are *TE* slab modes and *TM* slab modes. The mode profiles of the some *TE* and *TM* radiation modes are shown in Fig. (4.13) and (4.14), respectively. Again the vertical dashed lines on $z = R_z$ and $z = 0$ represent the limits of the guiding layer. In this zone, slab modes are not well confined in the guiding because these modes are decaying in the slab with refraction index n_1 but radiating in the slab with refraction index n_3 .

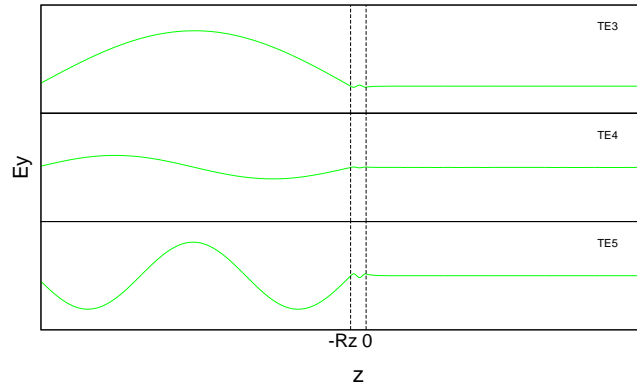


Figure 4.13. *TE* Slab Modes for Asymmetric Dielectric Waveguide Slab. Y-axis shows E_y component of the electric field and x-axis shows the z direction of the waveguide slab.

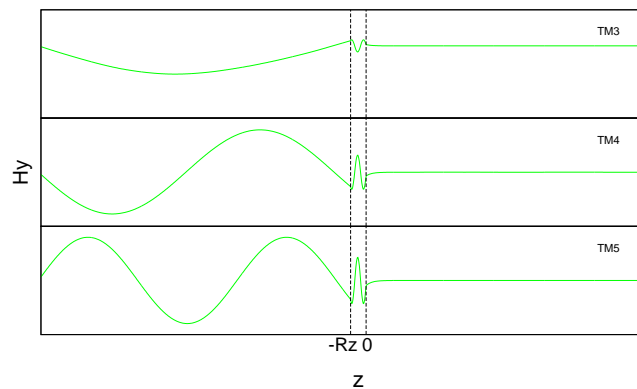


Figure 4.14. *TM* Slab Modes for Asymmetric Dielectric Waveguide Slab. Y-axis shows H_y component of the magnetic field and x-axis shows the z direction of the waveguide slab.

The radiation modes are above the red line. There are *TE* radiation modes and *TM* radiation modes. The mode profiles of the some *TE* and *TM* radiation modes are shown in Fig. (4.15) and (4.16), respectively. Again the vertical dashed lines on $z = R_z$ and $z = 0$ represent the limits of the guiding layer. In this zone, radiation modes are not well confined in the guiding layer because they are not decreasing exponentially outside the guiding layer. Contrarily outside of the guiding layer modes exist, and due to the asymmetrical structure, mode is asymmetric in the upper and lower slabs.

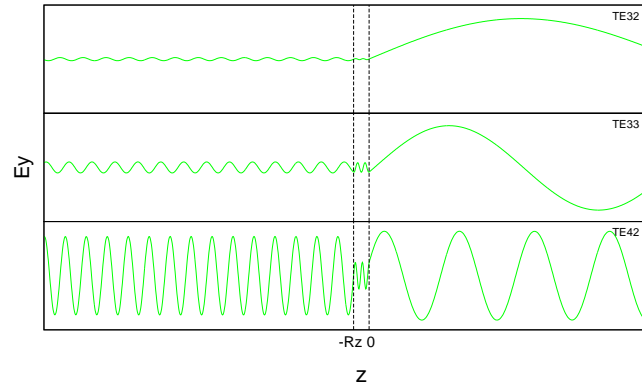


Figure 4.15. *TE* Radiation Modes for Asymmetric Dielectric Waveguide Slab. Y-axis shows E_y of the electric field, and x-axis shows the z direction of the waveguide slab.

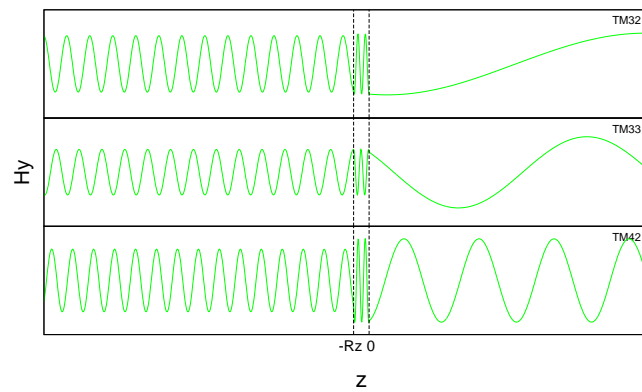


Figure 4.16. *TM* Radiation Modes for Asymmetric Dielectric Waveguide Slab. Y-axis shows H_y components of the magnetic field, and x-axis shows the z direction of the waveguide slab.

CHAPTER 5

PHOTONIC CRYSTAL WAVEGUIDE SLAB (PCW-SLAB)

Photonic crystal waveguides allow only certain electromagnetic wave modes to propagate inside the structure. Because of this characteristic, photonic crystal waveguides can be used to control light propagation in the integrated circuit design. But such integrated circuit designs can be realized in the three-dimensional system. This suggest us to use the PCW-slabs.

PCW-slabs are 1 dimensional or 2 dimensional periodic structures with a finite thickness in vertical z-direction. They achieve light confinement by using the effect of 2D-photonic crystal in the x-y plane and in the vertical direction by refractive index contrast.

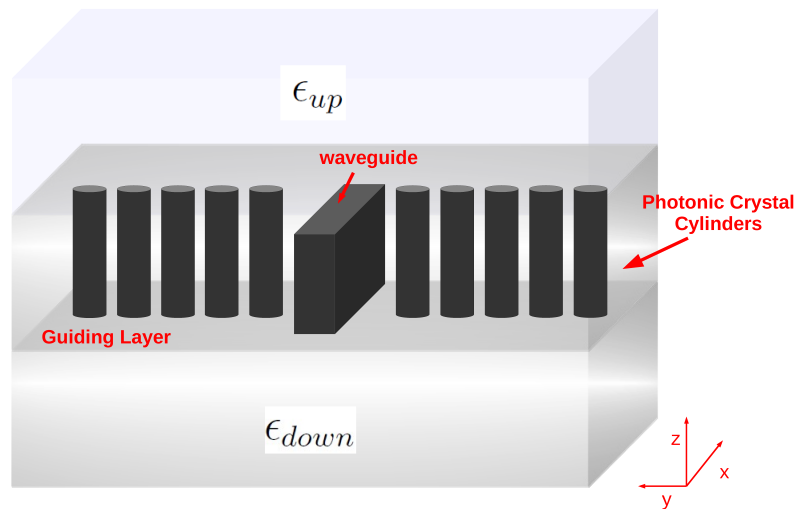


Figure 5.1. PCW-slab

In general the PCWG-slab consists of a guiding layer sandwiched between two finite bounded media as shown in Fig. (5.1). If two bounding media is identical then it is called symmetric PCW-slab ($\epsilon_{up} = \epsilon_{down}$). If two bounding media is not identical then waveguide called asymmetric PCW-slab ($\epsilon_{up} \neq \epsilon_{down}$). So we can say that symmetric waveguides are a special case of the asymmetric ones. For light confinement, the refractive index of the guiding

layer must be greater than that of the surrounding medium and the thickness of the guiding layer is typically of the order of a wavelength.

The outline of this chapter is as follows; firstly we will give a general mathematical formulation of PCW-slabs as eigenvalue problem for \mathbf{E} and \mathbf{H} respectively. The formulations are $(3N \times 3N)$ problems. Then by using a similarity transformation we will decrease the dimension from $(3N \times 3N)$ to $(2N \times 2N)$. These discussed formalisms are the same for both symmetric PCW-slabs and asymmetric PCW-slabs. The only difference is calculations of structure factors (dielectric permittivity), ϵ , so at the last section, we will give the calculation of ϵ for PCW-slab.

5.1. PCW-Slab as an Eigenvalue Problem

In this section our aim is formalize Maxwell equation for \mathbf{E} and \mathbf{H} in Eq. (4.10) and Eq. (5.2) in the form of an eigenvalue problem. The result of these formalisms are the same in both of the symmetric and asymmetric PCW slabs.

Maxwell's equations in a macroscopic medium were previously written as

$$\nabla \times \left[\frac{1}{\mu(\mathbf{r})} \nabla \times \mathbf{E} \right] + \frac{1}{c^2} \frac{\partial^2}{\partial t^2} \epsilon(\mathbf{r}) \mathbf{E} = 0 \quad (5.1)$$

$$\nabla \times \left[\frac{1}{\epsilon(\mathbf{r})} \nabla \times \mathbf{H} \right] + \frac{1}{c^2} \frac{\partial^2}{\partial t^2} \mu(\mathbf{r}) \mathbf{H} = 0 \quad (5.2)$$

where the fields depend on $\mathbf{r} = x\hat{\mathbf{x}} + y\hat{\mathbf{y}} + z\hat{\mathbf{z}}$. Let's write Fourier transformation for \mathbf{E} and \mathbf{H}

$$\mathbf{E}(\mathbf{r}, t) = \mathbf{E}(\mathbf{r}, t) = \int_{-\infty}^{\infty} d\omega \mathbf{E}(\mathbf{r}, \omega) e^{-i\omega t} \quad (5.3)$$

$$\mathbf{H}(\mathbf{r}, t) = \mathbf{H}(\mathbf{r}, t) = \int_{-\infty}^{\infty} d\omega \mathbf{H}(\mathbf{r}, \omega) e^{-i\omega t} \quad (5.4)$$

Plugging Eq. (5.3) into Eq. (5.1) and Eq. (5.4) into Eq. (5.2) we obtain

$$\int_{-\infty}^{\infty} d\omega e^{-i\omega t} \left\{ \nabla \times \left(\frac{1}{\mu(\mathbf{r})} \nabla \times \mathbf{E}(\mathbf{r}, \omega) \right) - \frac{\omega^2}{c^2} \epsilon(\mathbf{r}) \mathbf{E}(\mathbf{r}, \omega) \right\} = 0 \quad (5.5)$$

$$\int_{-\infty}^{\infty} d\omega e^{-i\omega t} \left\{ \nabla \times \left(\frac{1}{\epsilon(\mathbf{r})} \nabla \times \mathbf{H}(\mathbf{r}, \omega) \right) - \frac{\omega^2}{c^2} \mu(\mathbf{r}) \mathbf{H}(\mathbf{r}, \omega) \right\} = 0 \quad (5.6)$$

Considering the above equations since the Fourier transform of each term in curly braces vanishes, the terms in curly braces must vanish too;

$$\nabla \times \left(\frac{1}{\mu(\mathbf{r})} \nabla \times \mathbf{E}(\mathbf{r}) \right) - \frac{\omega^2}{c^2} \epsilon(\mathbf{r}) \mathbf{E}(\mathbf{r}) = 0 \quad (5.7)$$

$$\nabla \times \left(\frac{1}{\epsilon(\mathbf{r})} \nabla \times \mathbf{H}(\mathbf{r}) \right) - \frac{\omega^2}{c^2} \mu(\mathbf{r}) \mathbf{H}(\mathbf{r}) = 0 \quad (5.8)$$

to simplify the notation of the fields we suppress the ω dependence of the fields. We now write the fields in the next form;

$$\mathbf{E}(\mathbf{r}) = \int_{\text{all } \mathbf{q}} d^3 \mathbf{q} \mathbf{E}(\mathbf{q}) e^{i\mathbf{q} \cdot \mathbf{r}} \quad (5.9)$$

$$\mathbf{H}(\mathbf{r}) = \int_{\text{all } \mathbf{q}} d^3 \mathbf{q} \mathbf{H}(\mathbf{q}) e^{i\mathbf{q} \cdot \mathbf{r}} \quad (5.10)$$

where $\mathbf{q} = \mathbf{k} + \mathbf{G}$, $\mathbf{k} = \mathbf{k}_x + \mathbf{k}_y + \mathbf{k}_z$ (here $\mathbf{k}_x = \beta \hat{\mathbf{x}}$ is in the propagation direction) and $\mathbf{G} = G_x \hat{\mathbf{x}} + G_y \hat{\mathbf{y}} + G_z \hat{\mathbf{z}}$. If we substitute Eq. (5.9) and Eq. (5.10) into Eq. (5.7) and Eq. (5.8) respectively, we get

$$\nabla \times \left(\frac{1}{\mu(\mathbf{r})} \nabla \times \int_{\text{all } \mathbf{q}} d^3 \mathbf{q} \mathbf{E}(\mathbf{q}) e^{i\mathbf{q} \cdot \mathbf{r}} \right) - \frac{\omega^2}{c^2} \epsilon(\mathbf{r}) \int_{\text{all } \mathbf{q}} d^3 \mathbf{q} \mathbf{E}(\mathbf{q}) e^{i\mathbf{q} \cdot \mathbf{r}} = 0 \quad (5.11)$$

$$\nabla \times \left(\frac{1}{\epsilon(\mathbf{r})} \nabla \times \int_{\text{all } \mathbf{q}} d^3 \mathbf{q} \mathbf{H}(\mathbf{q}) e^{i\mathbf{q} \cdot \mathbf{r}} \right) - \frac{\omega^2}{c^2} \mu(\mathbf{r}) \int_{\text{all } \mathbf{q}} d^3 \mathbf{q} \mathbf{H}(\mathbf{q}) e^{i\mathbf{q} \cdot \mathbf{r}} = 0 \quad (5.12)$$

We can use the next vector identity to evaluate $\nabla \times \int_{\text{all } \mathbf{q}} d^3 \mathbf{q} \mathbf{E}(\mathbf{q}) e^{i\mathbf{q} \cdot \mathbf{r}}$

$$\nabla \times (g\mathbf{A}) = g(\nabla \times \mathbf{A}) - \mathbf{A} \times (\nabla g) \quad (5.13)$$

recalling that ∇ does not operate on \mathbf{q} only operates on \mathbf{r} we get

$$\begin{aligned}
\nabla \times \int_{\text{all } \mathbf{q}} d^3 \mathbf{q} \mathbf{E}(\mathbf{q}) e^{i\mathbf{q} \cdot \mathbf{r}} &= \int_{\text{all } \mathbf{q}} d^3 \mathbf{q} \nabla \times [e^{i\mathbf{q} \cdot \mathbf{r}} \mathbf{E}(\mathbf{q})] \\
&= \int_{\text{all } \mathbf{q}} d^3 \mathbf{q} [e^{i\mathbf{q} \cdot \mathbf{r}} (\nabla \times \mathbf{E}(\mathbf{q})) - \mathbf{E}(\mathbf{q}) \times (\nabla e^{i\mathbf{q} \cdot \mathbf{r}})] \\
&= \int_{\text{all } \mathbf{q}} d^3 \mathbf{q} [0 - \mathbf{E}(\mathbf{q}) \times (\nabla e^{i\mathbf{q} \cdot \mathbf{r}})] \\
&= \int_{\text{all } \mathbf{q}} d^3 \mathbf{q} i\mathbf{q} \times \mathbf{E}(\mathbf{q}) e^{i\mathbf{q} \cdot \mathbf{r}} \tag{5.14}
\end{aligned}$$

Since waveguide slab structure is periodic in yz -plane we can expand $\epsilon(\mathbf{r})$, $\mu(\mathbf{r})$ and their inverses as follows,

$$\epsilon(\mathbf{r}) = \epsilon(\mathbf{r}) = \sum_{\mathbf{G}} \epsilon(\mathbf{G}) e^{i\mathbf{G} \cdot \mathbf{r}} \tag{5.15}$$

$$\frac{1}{\epsilon(\mathbf{r})} = \eta(\mathbf{r}) = \eta(\mathbf{r}) = \sum_{\mathbf{G}} \eta(\mathbf{G}) e^{i\mathbf{G} \cdot \mathbf{r}} \tag{5.16}$$

$$\mu(\mathbf{r}) = \mu(\mathbf{r}) = \sum_{\mathbf{G}} \mu(\mathbf{G}) e^{i\mathbf{G} \cdot \mathbf{r}} \tag{5.17}$$

$$\frac{1}{\mu(\mathbf{r})} = \varsigma(\mathbf{r}) = \varsigma(\mathbf{r}) = \sum_{\mathbf{G}} \varsigma(\mathbf{G}) e^{i\mathbf{G} \cdot \mathbf{r}} \tag{5.18}$$

The integral in Eq. (5.11) over \mathbf{q} is over the entire reciprocal space. Now we broke the reciprocal space into cells and reformulate it as in the next form;

$$\int_{\text{all } \mathbf{q}} d^3 \mathbf{q} g(\mathbf{q}) \longrightarrow \int_{\text{cell}} d^3 \mathbf{k} \sum_{\mathbf{G}} g(\mathbf{k} + \mathbf{G}). \tag{5.19}$$

Substituting Eq. (5.14) and Eq. (5.16) into Eq. (5.11) and using the new formalism in Eq. (5.19) we get

$$\begin{aligned}
\nabla \times \left[\left(\sum_{\mathbf{G}''} \varsigma(\mathbf{G}'') e^{i\mathbf{G}'' \cdot \mathbf{r}} \right) \left(\int_{\text{cell}} d^3 \mathbf{k} \sum_{\mathbf{G}'} i(\mathbf{k} + \mathbf{G}') \times \mathbf{E}(\mathbf{k} + \mathbf{G}') e^{i(\mathbf{k} + \mathbf{G}') \cdot \mathbf{r}} \right) \right] \\
- \frac{\omega^2}{c^2} \left(\sum_{\mathbf{G}''} \epsilon(\mathbf{G}'') e^{i\mathbf{G}'' \cdot \mathbf{r}} \right) \left(\int_{\text{cell}} d^3 \mathbf{k} \sum_{\mathbf{G}'} \mathbf{E}(\mathbf{k} + \mathbf{G}') e^{i(\mathbf{k} + \mathbf{G}') \cdot \mathbf{r}} \right) = 0
\end{aligned}$$

$$\int_{\text{cell}} d^3\mathbf{k} \sum_{\mathbf{G}''} \sum_{\mathbf{G}'} \varsigma(\mathbf{G}'') \nabla \times \left[i(\mathbf{k} + \mathbf{G}') \times \mathbf{E}(\mathbf{k} + \mathbf{G}') e^{i(\mathbf{k} + \mathbf{G}' + \mathbf{G}'') \cdot \mathbf{r}} \right] - \frac{\omega^2}{c^2} \int_{\text{cell}} d^3\mathbf{k} \sum_{\mathbf{G}''} \sum_{\mathbf{G}'} \epsilon(\mathbf{G}'') \mathbf{E}(\mathbf{k} + \mathbf{G}') e^{i(\mathbf{k} + \mathbf{G}' + \mathbf{G}'') \cdot \mathbf{r}} = 0$$

taking the integral sign to the left calculating ∇ we get;

$$\int_{\text{cell}} d^3\mathbf{k} \sum_{\mathbf{G}''} \sum_{\mathbf{G}'} e^{i(\mathbf{k} + \mathbf{G}' + \mathbf{G}'') \cdot \mathbf{r}} \left[\varsigma(\mathbf{G}'')(\mathbf{k} + \mathbf{G}' + \mathbf{G}'') \times [(\mathbf{k} + \mathbf{G}') \times \mathbf{E}(\mathbf{k} + \mathbf{G}')] + \frac{\omega^2}{c^2} \epsilon(\mathbf{G}'') \mathbf{E}(\mathbf{k} + \mathbf{G}') \right] = 0$$

Letting $\mathbf{G} \equiv \mathbf{G}' + \mathbf{G}''$ and rearranging the equation we get,

$$\int_{\text{cell}} d^3\mathbf{k} \sum_{\mathbf{G}} e^{i(\mathbf{k} + \mathbf{G}) \cdot \mathbf{r}} \left[\sum_{\mathbf{G}'} \varsigma(\mathbf{G} - \mathbf{G}')(\mathbf{k} + \mathbf{G}) \times [(\mathbf{k} + \mathbf{G}') \times \mathbf{E}(\mathbf{k} + \mathbf{G}')] + \frac{\omega^2}{c^2} \sum_{\mathbf{G}'} \epsilon(\mathbf{G} - \mathbf{G}') \mathbf{E}(\mathbf{k} + \mathbf{G}') \right] = 0.$$

Now we will use Eq. (5.19)

$$\int_{\text{all } \mathbf{q}} d^3\mathbf{q} e^{i\mathbf{q} \cdot \mathbf{r}} \left[\sum_{\mathbf{G}'} \varsigma(\mathbf{G} - \mathbf{G}')(\mathbf{k} + \mathbf{G}) \times [(\mathbf{k} + \mathbf{G}') \times \mathbf{E}(\mathbf{k} + \mathbf{G}')] + \frac{\omega^2}{c^2} \sum_{\mathbf{G}'} \epsilon(\mathbf{G} - \mathbf{G}') \mathbf{E}(\mathbf{k} + \mathbf{G}') \right] = 0.$$

Since the Fourier transform of the term in braces vanishes, inside it is equal to 0;

$$\sum_{\mathbf{G}'} \varsigma(\mathbf{G} - \mathbf{G}')(\mathbf{k} + \mathbf{G}) \times [(\mathbf{k} + \mathbf{G}') \times \mathbf{E}(\mathbf{k} + \mathbf{G}')] + \frac{\omega^2}{c^2} \sum_{\mathbf{G}'} \epsilon(\mathbf{G} - \mathbf{G}') \mathbf{E}(\mathbf{k} + \mathbf{G}') = 0.$$

If we substitute $\mathbf{E} \rightarrow \mathbf{H}$, $\epsilon \rightarrow \mu$ and $\varsigma \rightarrow \eta$, we can obtain a similar equation for \mathbf{H}

$$\sum_{\mathbf{G}'} \eta(\mathbf{G} - \mathbf{G}')(\mathbf{k} + \mathbf{G}) \times [(\mathbf{k} + \mathbf{G}') \times \mathbf{H}(\mathbf{k} + \mathbf{G}')] + \frac{\omega^2}{c^2} \sum_{\mathbf{G}'} \mu(\mathbf{G} - \mathbf{G}')\mathbf{H}(\mathbf{k} + \mathbf{G}') = 0.$$

As a result now we have the last two equations are in the form of eigenvalue equation

$$\underbrace{\sum_{\mathbf{G}} \varsigma(\mathbf{G} - \mathbf{G}')(\mathbf{k} + \mathbf{G}) \times [(\mathbf{k} + \mathbf{G}') \times \mathbf{E}(\mathbf{k} + \mathbf{G}')] }_{A_x} = -\frac{\omega^2}{c^2} \underbrace{\sum_{\mathbf{G}'} \epsilon(\mathbf{G} - \mathbf{G}')\mathbf{E}(\mathbf{k} + \mathbf{G}')}_{\lambda B_x}, \quad (5.20)$$

$$\underbrace{\sum_{\mathbf{G}} \eta(\mathbf{G} - \mathbf{G}')(\mathbf{k} + \mathbf{G}) \times [(\mathbf{k} + \mathbf{G}') \times \mathbf{H}(\mathbf{k} + \mathbf{G}' + \beta \hat{\mathbf{x}})] }_{A_x} = -\frac{\omega^2}{c^2} \underbrace{\sum_{\mathbf{G}'} \mu(\mathbf{G} - \mathbf{G}')\mathbf{H}(\mathbf{k} + \mathbf{G}')}_{\lambda B_x}. \quad (5.21)$$

5.1.1. Similarity Transformation

The equations (5.20) and (5.21) are $3N \times 3N$ generalized eigenvalue problems, which can be solved to find ω for the given values of \mathbf{k} . The dimensions of the problem can be reduced by using a similarity transformation from $3N \times 3N$ to $2N \times 2N$.

From now on we will make calculations only for \mathbf{H} and then at the end of the section, we will pass from \mathbf{H} to \mathbf{E} .

Let's define

$$\hat{\mathbf{e}}_3 \equiv \frac{\mathbf{q}}{|\mathbf{q}'|}, \quad \hat{\mathbf{e}}_2 \equiv \frac{\hat{\mathbf{e}}_3 \times \hat{\mathbf{x}}}{|\hat{\mathbf{e}}_3 \times \hat{\mathbf{x}}|}, \quad \hat{\mathbf{e}}_1 \equiv \hat{\mathbf{e}}_2 \times \hat{\mathbf{e}}_3 \quad (5.22)$$

where $\mathbf{q} = \mathbf{k} + \mathbf{G} = (k_x + G_x, k_y + G_y, k_z + G_z)$ and $\mathbf{q}' = \mathbf{k} + \mathbf{G}' = (k_x + G'_x, k_y + G'_y, k_z + G'_z)$. Only the direction of $\hat{\mathbf{e}}_3$ is significant, because \mathbf{H} mustn't have any component at the direction of $\hat{\mathbf{e}}_3$ since $\nabla \cdot \mathbf{H} = 0$. However $\hat{\mathbf{e}}_2$ and $\hat{\mathbf{e}}_1$ can be any orthogonal vectors such that perpendicular to $\hat{\mathbf{e}}_3$. We can redefine components of \mathbf{H} in Cartesian basis $(\hat{\mathbf{x}}_1, \hat{\mathbf{x}}_2, \hat{\mathbf{x}}_3)$ and in the defined basis $(\hat{\mathbf{e}}_1, \hat{\mathbf{e}}_2, \hat{\mathbf{e}}_3)$ as,

$$\begin{cases} H_i \equiv \hat{\mathbf{x}}_i \cdot \mathbf{H} & \text{in the cartesian basis} \\ \tilde{H}_i \equiv \hat{\mathbf{e}}_i \cdot \mathbf{H} & \text{in the defined basis} \end{cases}$$

where $i = 1, 2, 3$. Introducing a transition matrix s_{ij} by relating the two basis as the following way

$$\begin{aligned} \mathbf{H} &= \sum_{i=1}^3 \hat{\mathbf{e}}_i (\hat{\mathbf{e}}_i \cdot \mathbf{H}) = \sum_{i=1}^3 \hat{\mathbf{e}}_i \left[\hat{\mathbf{e}}_i \cdot \left(\sum_{j=1}^3 \hat{\mathbf{x}}_j H_j \right) \right] = \sum_{i=1}^3 \hat{\mathbf{e}}_i \left[\sum_{j=1}^3 (\hat{\mathbf{e}}_i \cdot \hat{\mathbf{x}}_j) H_j \right] \\ &= \sum_{i=1}^3 \hat{\mathbf{e}}_i \left(\sum_{j=1}^3 s_{ij} H_j \right) = \sum_{i=1}^3 \hat{\mathbf{e}}_i \tilde{H}_i \end{aligned} \quad (5.23)$$

we get $\tilde{H}_i = \sum_{j=1}^3 s_{ij} H_j$ where $s_{ij} = (\hat{\mathbf{e}}_i \cdot \hat{\mathbf{x}}_j)$ is an orthogonal matrix, in the next form, We find the orthogonal s matrix using our new basis, in the next form,

$$s = \begin{bmatrix} \frac{q_y^2 + q_z^2}{|q| \sqrt{q_y^2 + q_z^2}} & \frac{-q_x q_y}{|q| \sqrt{q_y^2 + q_z^2}} & \frac{-q_x q_z}{|q| \sqrt{q_y^2 + q_z^2}} \\ 0 & \frac{q_z}{\sqrt{q_y^2 + q_z^2}} & \frac{-q_y}{\sqrt{q_y^2 + q_z^2}} \\ \frac{q_x}{|q|} & \frac{q_y}{|q|} & \frac{q_z}{|q|} \end{bmatrix} \quad (5.24)$$

Let's define an orthogonal $3N \times 3N$ matrix S , which is an $N \times N$ block diogonal matrix of s matrix, $S_{\mathbf{G}, \mathbf{G}'} \equiv \delta_{\mathbf{G}, \mathbf{G}'} s_{\mathbf{G}}$

$$S = \begin{bmatrix} \left[\begin{array}{c} s \\ \vdots \\ 0 \end{array} \right]_{3 \times 3} & 0 & \cdots & 0 \\ 0 & \left[\begin{array}{c} s \\ \vdots \\ 0 \end{array} \right]_{3 \times 3} & \cdots & 0 \\ \vdots & \vdots & \ddots & \vdots \\ 0 & 0 & \cdots & \left[\begin{array}{c} s \\ \vdots \\ 0 \end{array} \right]_{3 \times 3} \end{bmatrix}_{N \times N}$$

By using similarity transformation with the help of the S matrix, $SS^\dagger = S^\dagger S = 1$, we rewrite

Eq. (5.21) as,

$$\begin{aligned}
A_x &= \lambda Bx \\
SAS^\dagger Sx &= \lambda SBS^\dagger Sx \\
(SAS^\dagger)(Sx) &= \lambda(SBS^\dagger)(Sx) \\
\tilde{A}\tilde{x} &= \lambda\tilde{B}\tilde{x}.
\end{aligned} \tag{5.25}$$

Now we evaluate the matrices \tilde{A} and \tilde{B} , bearing in mind that A and B matrices are $N \times N$ block matrices with 3×3 blocks. Firstly we start from \tilde{A} ;

$$\begin{aligned}
\tilde{A} = [SAS^\dagger]_{\mathbf{G}, \mathbf{G}'} &= \sum_{\mathbf{G}''} \sum_{\mathbf{G}'''} S_{\mathbf{G}, \mathbf{G}''} A_{\mathbf{G}'' \mathbf{G}'''} S_{\mathbf{G}'''}^\dagger \\
&= \sum_{\mathbf{G}''} \sum_{\mathbf{G}'''} \delta_{\mathbf{G} \mathbf{G}''} s_{\mathbf{G}} A_{\mathbf{G}'' \mathbf{G}'''} \delta_{\mathbf{G}'''} s_{\mathbf{G}'}^\dagger \\
&= s_{\mathbf{G}} A_{\mathbf{G} \mathbf{G}'} s_{\mathbf{G}'}^\dagger
\end{aligned} \tag{5.26}$$

After some calculations we get \tilde{A}

$$\tilde{A} = \eta(\mathbf{G} - \mathbf{G}') \begin{bmatrix} -\frac{|q||q'|(q_y q'_y + q_z q'_z)}{\sqrt{q_y^2 + q_z^2} \sqrt{q_y'^2 + q_z'^2}} & -\frac{q'_x |q|(-q'_y q_z + q_y q'_z)}{\sqrt{q_y^2 + q_z^2} \sqrt{q_y'^2 + q_z'^2}} & 0 \\ \frac{q_x |q'|(q'_y q_z - q_y q'_z)}{\sqrt{q_y^2 + q_z^2} \sqrt{q_y'^2 + q_z'^2}} & -\frac{q_x q'_x (q_y q'_y + q_z q'_z) + (q_y^2 + q_z^2)(q_y'^2 + q_z'^2)}{\sqrt{q_y^2 + q_z^2} \sqrt{q_y'^2 + q_z'^2}} & 0 \\ 0 & 0 & 0 \end{bmatrix}. \tag{5.27}$$

If we restrict our work for a class of materials which have weak magnetic susceptibilities, and assume $\mu(r) = 1$, then $\mu(\mathbf{G} - \mathbf{G}') = \delta_{\mathbf{G} \mathbf{G}'}$. That follows $SBS^\dagger = I$ and we get the next result;

$$\sum_{\mathbf{G}'} \eta(\mathbf{G} - \mathbf{G}') \begin{bmatrix} -\frac{|q||q'|(q_y q'_y + q_z q'_z)}{\sqrt{q_y^2 + q_z^2} \sqrt{q_y'^2 + q_z'^2}} & -\frac{q'_x |q|(-q'_y q_z + q_y q'_z)}{\sqrt{q_y^2 + q_z^2} \sqrt{q_y'^2 + q_z'^2}} \\ \frac{q_x |q'|(q'_y q_z - q_y q'_z)}{\sqrt{q_y^2 + q_z^2} \sqrt{q_y'^2 + q_z'^2}} & -\frac{q_x q'_x (q_y q'_y + q_z q'_z) + (q_y^2 + q_z^2)(q_y'^2 + q_z'^2)}{\sqrt{q_y^2 + q_z^2} \sqrt{q_y'^2 + q_z'^2}} \end{bmatrix} \begin{bmatrix} \tilde{H}_x \\ \tilde{H}_y \end{bmatrix} = \frac{\omega^2}{c^2} \begin{bmatrix} \tilde{H}_x \\ \tilde{H}_y \end{bmatrix}$$

Once calculating $\tilde{\mathbf{H}}$ we can calculate $\mathbf{H} = S^{-1} \tilde{\mathbf{H}}$ and then using the Maxwell equation

$\nabla \times \mathbf{H} = \epsilon_0 \epsilon(r) \partial \mathbf{E} / \partial t$ we can calculate \mathbf{E} in the next form;

$$\mathbf{E}(\mathbf{q}') = -\frac{1}{\omega \epsilon_0} \left[\sum_{\mathbf{G}'} \epsilon(\mathbf{G} - \mathbf{G}') \right]^{-1} (\mathbf{q} \times \mathbf{H}(\mathbf{q})).$$

As mentioned earlier, until now, all calculations are the same for symmetric and asymmetric PCW-slabs. The only thing that creates the change is the dielectric permittivity, ϵ , so at the next section we give some examples about the calculation of ϵ .

5.2. PCW-Slab Structure

We want to calculate the structure factors, which is called dielectric permittivity (ϵ). The calculations will be hold for two different PCW-slabs, one of them is called 1D-LDWG slab and the other is called 2D-LDWG slab. We will use these calculations at next chapter.

5.2.1. 1D-LDWG Slab Structure

In this example, we consider a 2D array of slabs with length $2R$ sandwiched between two dielectric medium ϵ_{upper} and ϵ_{lower} respectively, as shown in Fig. (5.2). The length of the middle part is $2R_z$. The slabs have a dielectric constant ϵ_a and the background medium has a dielectric constant of ϵ_b . The length of the waveguide is $2R_d$ with a dielectric constant of ϵ_d . The distance of the half of the defect slab to the half of the nearest slab is R_1 .

1D-LDWG slab structure is periodic in yz -plane so we only calculate over the yz coordinates. The reciprocal lattice vectors are $\mathbf{G} = (\frac{2\pi}{a})(n_y \hat{\mathbf{y}} + n_z \hat{\mathbf{z}})$. The Fourier coefficients

$\epsilon(\mathbf{G})$ are calculated as

$$\begin{aligned}
\epsilon(\mathbf{G}) &= \frac{1}{V_{cell}} \int_{cell} \epsilon(\mathbf{r}) e^{-i(\mathbf{G} \cdot \mathbf{r})} d^2\mathbf{r} \\
&= \frac{1}{V_{cell}} \epsilon_{up} \int_{-\frac{A_y}{2}}^{\frac{A_y}{2}} e^{-iG_y y} dy \int_{-\frac{A_z}{2}}^{\frac{A_z}{2}} e^{-iG_z z} dz \\
&+ \frac{1}{V_{cell}} (\epsilon_b - \epsilon_{up}) \int_{-\frac{A_y}{2}}^{\frac{A_y}{2}} e^{-iG_y y} dy \int_{-R_z}^{R_z} e^{-iG_z z} dz \\
&+ \frac{1}{V_{cell}} (\epsilon_a - \epsilon_b) \sum_{j=1}^{MSCy} 2 \cos(\mathbf{G} \cdot \mathbf{b}_j) \int_{-R}^R e^{-iG_y y} dy \int_{-R_z}^{R_z} e^{-iG_z z} dz \quad (5.28) \\
&+ \frac{1}{V_{cell}} (\epsilon_d - \epsilon_b) \int_{-Rd}^{Rd} e^{-iG_y y} dy \int_{-R_z}^{R_z} e^{-iG_z z} dz \\
&+ \frac{1}{V_{cell}} (\epsilon_{down} - \epsilon_{up}) e^{-i(\mathbf{Gz} \cdot \mathbf{bzb})} \int_{-\frac{A_y}{2}}^{\frac{A_y}{2}} e^{-iG_y y} dy \int_{-R_{zb}}^{R_{zb}} e^{-iG_z z} dz
\end{aligned}$$

where, $R_{zb} = ((A_z/2) - R_z)/2$, $\mathbf{b}_j = R_1 + (j - 1)a$, $bzb = R_z + R_{zb}$, $MSCy = 5$.

5.2.2. 2D-LDWG Slab Structure

In this example, we consider a 3D array of circular cylindrical rods of radius R sandwiched between two dielectric medium ϵ_{upper} and ϵ_{lower} respectively, as shown in Fig. (5.3). The length of the middle part is $2R_z$. The circular cylindrical rods have a dielectric constant ϵ_a and the background medium has a dielectric constant of ϵ_b . The length of the waveguide is $2Rd$ with a dielectric constant of ϵ_d . The distance of the half of the defect slab to the half of the nearest circular cylindrical rod is R_1 .

The structure is periodic in 3D. The reciprocal lattice vectors are $\mathbf{G} = (\frac{2\pi}{a})(n_x \hat{\mathbf{x}} +$

$n_y \hat{\mathbf{y}} + n_z \hat{\mathbf{z}}$). The Fourier coefficients $\epsilon(\mathbf{G})$ are calculated as

$$\begin{aligned}
\epsilon(\mathbf{G}) &= \frac{1}{V_{cell}} \int_{cell} \epsilon(\mathbf{r}) e^{-i(\mathbf{G} \cdot \mathbf{r})} d^3\mathbf{r} \\
&= \frac{1}{V_{cell}} \epsilon_{up} \int_{-\frac{A_x}{2}}^{\frac{A_x}{2}} e^{-iG_x x} dx \int_{-\frac{A_y}{2}}^{\frac{A_y}{2}} e^{-iG_y y} dy \int_{-\frac{A_z}{2}}^{\frac{A_z}{2}} e^{-iG_z z} dz \\
&+ \frac{1}{V_{cell}} (\epsilon_b - \epsilon_{up}) \int_{-\frac{A_x}{2}}^{\frac{A_x}{2}} e^{-iG_x x} dx \int_{-\frac{A_y}{2}}^{\frac{A_y}{2}} e^{-iG_y y} dy \int_{-R_z}^{R_z} e^{-iG_z z} dz \\
&+ \frac{1}{V_{cell}} (\epsilon_a - \epsilon_b) \sum_{j=1}^{MSCy} 2 \cos(\mathbf{G} \cdot \mathbf{b}_j) \int_0^{2\pi} \int_0^R r e^{-i\mathbf{G} \cdot \mathbf{r}} dr d\theta \int_{-R_z}^{R_z} e^{-iG_z z} dz \quad (5.29) \\
&+ \frac{1}{V_{cell}} (\epsilon_d - \epsilon_b) \int_{-\frac{A_x}{2}}^{\frac{A_x}{2}} e^{-iG_x x} dx \int_{-\frac{Rd}{2}}^{\frac{Rd}{2}} e^{-iG_y y} dy \int_{-R_z}^{R_z} e^{-iG_z z} dz \\
&+ \frac{1}{V_{cell}} (\epsilon_{down} - \epsilon_{up}) e^{-i(\mathbf{Gz} \cdot \mathbf{bzb})} \int_{-\frac{A_x}{2}}^{\frac{A_x}{2}} e^{-iG_x x} dx \int_{-\frac{A_y}{2}}^{\frac{A_y}{2}} e^{-iG_y y} dy \int_{-R_{zb}}^{R_{zb}} e^{-iG_z z} dz
\end{aligned}$$

where, $R_{zb} = ((A_z/2) - R_z)/2$, $\mathbf{b}_j = R_1 + (j - 1)a$, $bzb = R_z + R_{zb}$, $MSCy = 5$.

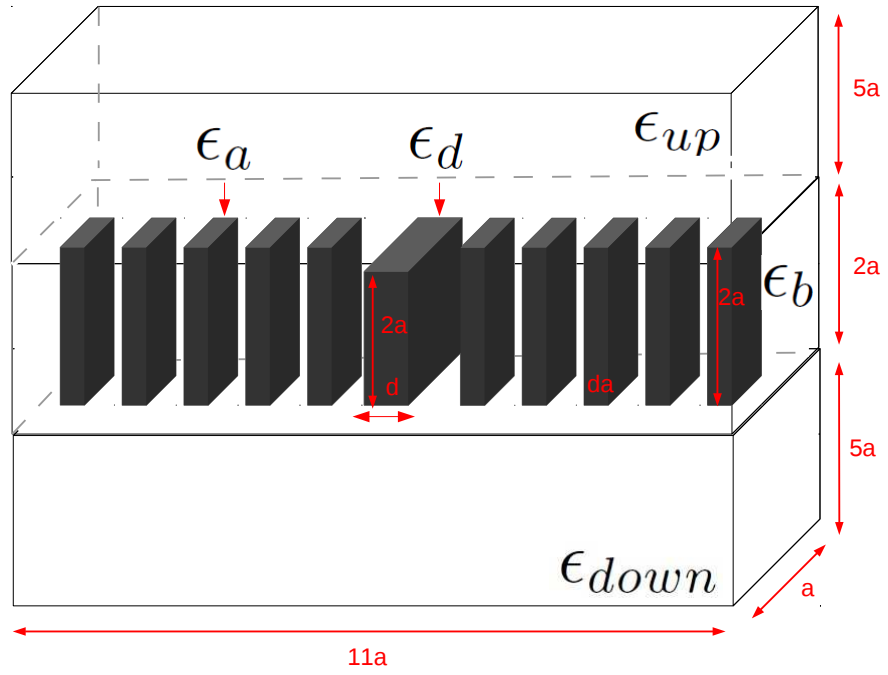


Figure 5.2. 1D-LDWG slab.

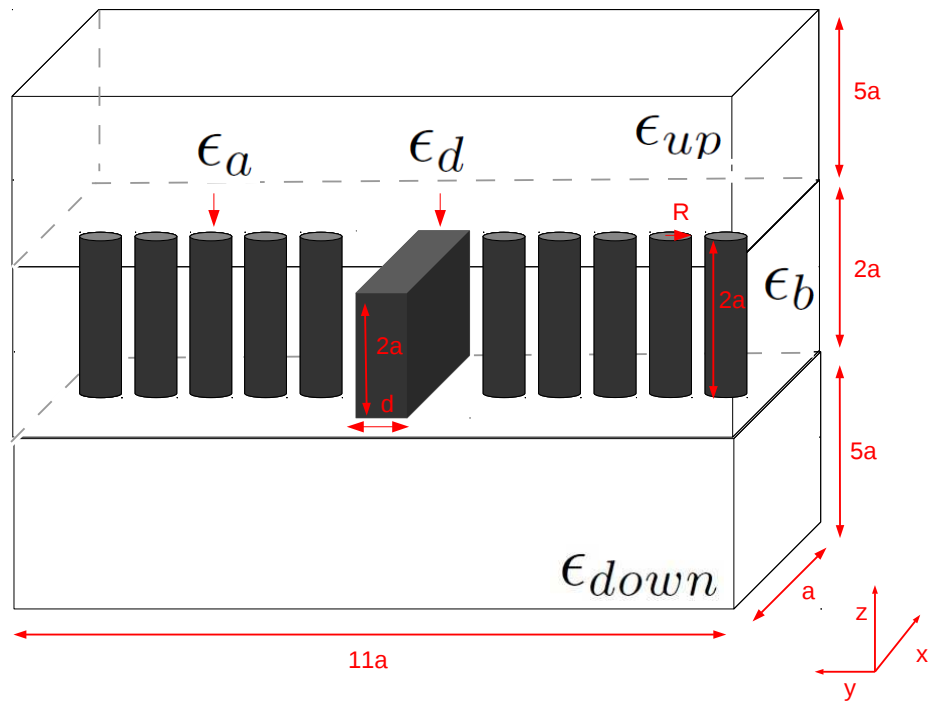


Figure 5.3. 2D-LDWG slab.

CHAPTER 6

L-SHAPED PHOTONIC CRYSTAL WAVEGUIDE SLAB

In this chapter we present photonic crystal line defect waveguide slabs to bend light. The structures are combination of 1 dimensionally periodic waveguide slab (1D-LDWG slab) and 2 dimensionally periodic line defect waveguide slab (2D-LDWG slab).

1D-LDWG slab is not periodic in the direction of propagation. Therefore light will be guided with much less loss in such a waveguide due to lesser manufacturing imperfections as a result of its much simpler geometry Taniyama et al. (2005)-Sözüer and Sevim (2005). So 1D-LDWG slab is a good option if light would travel straight.

On the other hand 2D-LDWG slab is periodic into two dimensions, thus it has sensitivity to imperfections during manufacturing, that causes to high losses and limits their usage to guide light over long distances Hughes et al. (2005), Kuramochi et al. (2005). Besides, the high dispersion of 2D-LDWG slab limits their used bandwidth. So although 2D-LDWG slab is not a good choice for light to travel straight in it for long distances, it is still the most convenient geometry to bend the light through a 90° turn Chutinan et al. (2003).

We will use the 1D-LDWG slab for the straight sections and use a 2D-LDWG slab for the corners. By this way, the wave travels with little loss through the straight sections, turns through sharp corner with little bending loss and then re-enters the 1D-LDWG slab region to travel for another long straight segment.

L-shaped photonic crystal line defect waveguide structure in 2D was previously worked in the article Sami Sözüer and DUYGU ŞENGÜN (2011). The obtained transmission result is nearly %100 for $(\beta a/2\pi, \omega a/2\pi) = (0.68, 0.2667)$. We examine the 3D version of this approach in terms of transmission.

In this chapter we briefly discuss the waveguide structures in 2D and 3D, then we give information about mode polarization and mode coupling of the band diagrams. After we show band diagrams for silica silicon waveguide slab and air silicon waveguide slab for each one symmetric and asymmetric cases and discuss on transmission results.

6.1. Waveguide Structures in 2D

In order to understand thoroughly the 3D structure we start from analogous 2D structure. The 3D structures can be converted to 2D by considering $z = 0$ plane of view. In two dimensions we will work on two forms. We will call them as "silica silicon waveguide" and "air silicon waveguide". The only difference between the forms are background materials. In the "silica silicon waveguide" we use silica as a background while in the "air silicon waveguide" we use air. In Fig. (6.2) we see the 2D version of the forms which is common for both of the structures.

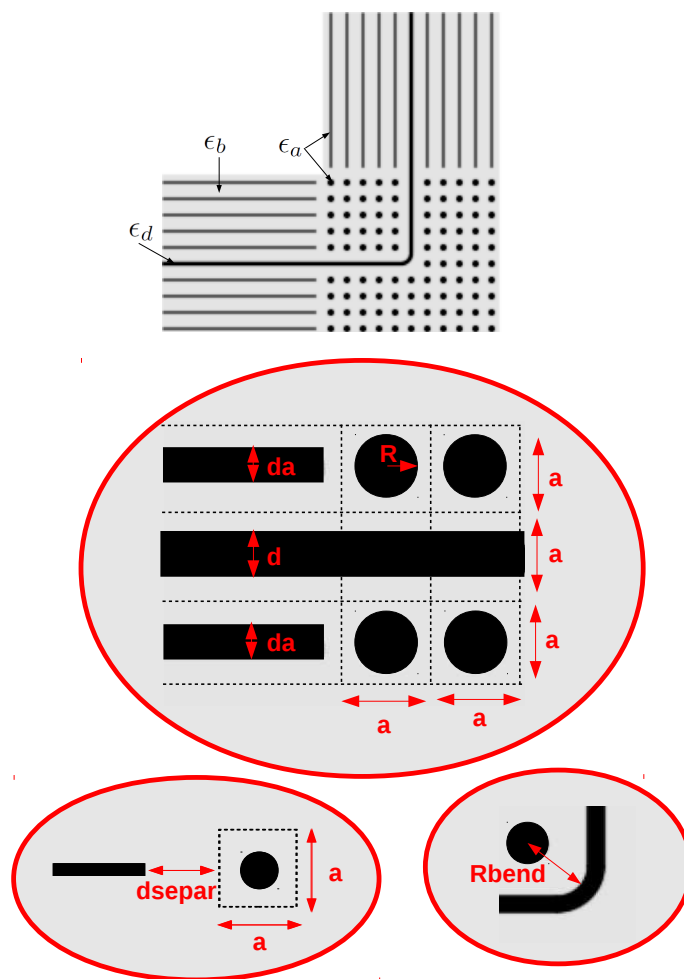


Figure 6.2. L-shaped photonic crystal line defect waveguide in 2D on the top, geometrical details of line defect waveguide on the bottom.

In Fig. (6.2) we see that, the silicon slabs with thickness $da = 0.179a$, where a is a lattice constant, and with dielectric constant of $\epsilon_a = 13$ (color in black) immersed in the silica background with $\epsilon_b = 2.25$ for the "silica silicon waveguide" and for the "air silicon waveguide" air background with $\epsilon_b = 1$ is used (color in gray). Here, we formed the defect by removing one row of dielectric slabs and by placing a dielectric slab of thickness $d = 0.3184a$ and with dielectric constant of $\epsilon_d = 13$. The corner element designed from square lattice of silicon rods of radius $R = 0.2387a$ and immersed in a silica background. The line defect is formed by removing one row of dielectric rods and by extending the core of the 1D-LDWG. Rbend is $2d$ and dsepar is $0.2a$.

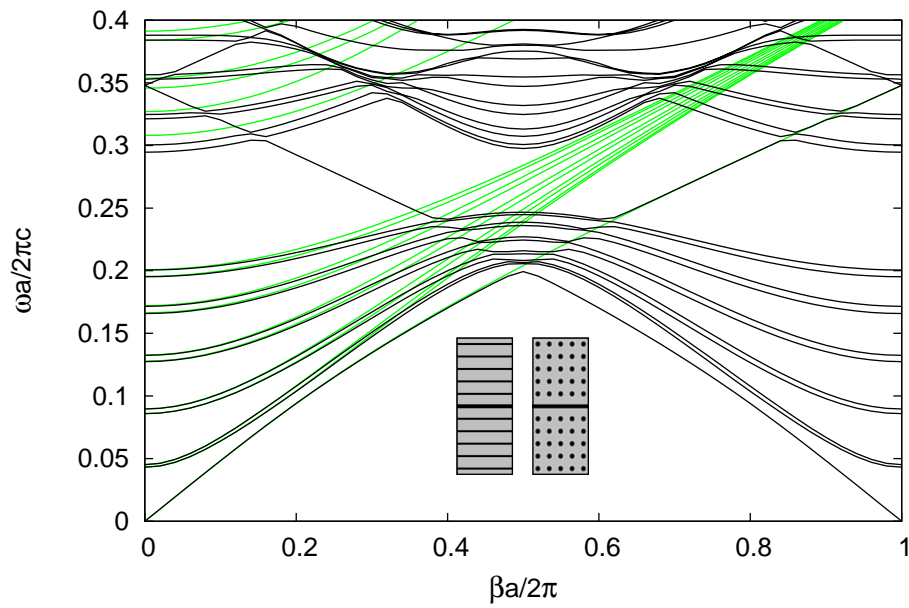


Figure 6.3. "Silica silicon waveguide". The overlapped band diagrams of 1D-LDWG in green color and 2D-LDWG in black color.

The corresponding band diagrams of the structures for transverse electric (TE) modes with $E_x = 0, E_y = 0, E_z \neq 0$ are given in Fig. (6.3) and in Fig. (6.4) for the "silica silicon waveguide" and for the "air silicon waveguide", respectively.

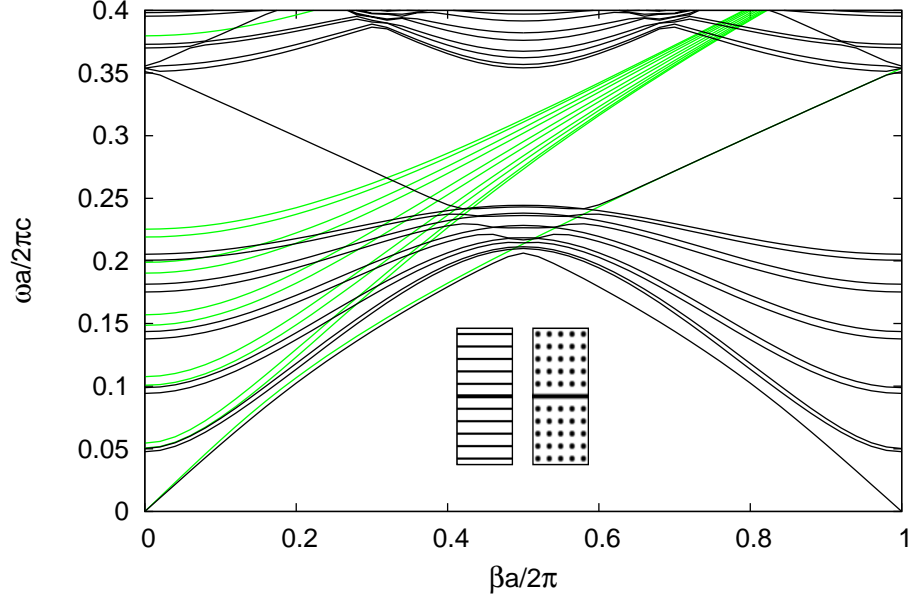


Figure 6.4. "Air silicon waveguide." The overlapped band diagrams of 1D-LDWG in green color and 2D-LDWG in black color.

The green bands show the propagation modes for 1D-LDWG. The black bands show the propagation modes for 2D-LDWG. Since our proposed structures are combinations of 1D-LDWG and 2D-LDWG light should be able to propagate in the both. This is why we give the overlapped graphs for structures. When the "silica silicon waveguide" in Fig. (6.3) is compared with the "air silicon waveguide" in Fig. (6.4), we see that the band gap is bigger at "air silicon waveguide" because of the high contrast in the dielectric constants.

The band diagrams in the figures are modelled using the supercell method with a supercell size of $A_x \times A_y$. We used $A_x = a$ and $A_y = 11a$ for 1D-LDWG, and for 2D-LDWG, we used $A_x = 11a$ and $A_y = 11a$. The supercell sizes are adjusted to ensure that the guided mode is well contained within the supercell.

6.2. Waveguide Structures in 3D

At the previous section we presented "silica silicon waveguide" and "air silicon waveguide" in 2D. Now we give the structures the third dimension by giving them a height, " R_z ", and sandwiching them into the two slabs. We will name them according to the above and below slabs, symmetric or asymmetric. If the waveguide is surrounded by air from above and

below, that gives it a symmetrical feature, so we will call it symmetric. If the waveguide is surrounded by air from above and silica from below, that gives it an asymmetrical feature, so we will call it asymmetric. In this way we can designate the structures as follows; symmetric silica silicon waveguide slab (sss-wgs), asymmetric silica silicon waveguide slab (ass-wgs), symmetric air silicon waveguide slab (sas-wgs) and asymmetric air silicon waveguide slab (aas-wgs) as shown the below.

$$\begin{array}{l}
 \text{Silica silicon waveguide slab} \\
 \text{Air silicon waveguide slab}
 \end{array}
 \left\{ \begin{array}{l}
 \text{Symmetric silica silicon waveguide slab (sss-wgs)} \\
 \text{Asymmetric silica silicon waveguide slab (ass-wgs)} \\
 \text{Symmetric air silicon waveguide slab (sas-wgs)} \\
 \text{Asymmetric air silicon waveguide slab (aas-wgs)}
 \end{array} \right.$$

No matter what the name is all of the structures are a combination of 1D-LDWG slab and 2D-LDWG slab. At the figures (5.2) and (5.3) we define the names of the values for 1D-LDWG slab and 2D-LDWG slab respectively.

The table (6.1) give the dielectric values for the each variations. In this table the structures are given by their shortened names. Since the dielectric constants are the same for 1D-LDWG slab and 2D-LDWG slab we have not specified separately.

Dielectric Constants	sss-wgs	ass-wgs	sas-wgs	aas-wgs
ϵ_a	13	13	13	13
ϵ_b	2.25	2.25	1	1
ϵ_d	13	13	13	13
ϵ_{up}	1	1	1	1
ϵ_{down}	1	2.25	1	2.25

Table 6.1. Dielectric values for each variations.

6.3. Mode Polarization

For photonic crystals in 1D and 2D, the fields are divided into two polarizations by symmetry: transverse electric (TE) modes, in which no electric field in the direction of propagation (in our case $E_x = 0$) and transverse magnetic (TM) modes, in which no magnetic field in the direction of propagation (in our case $H_x = 0$).

We can see 2D-LDWG band diagrams of "silica silicon waveguide" and "air silicon waveguide" in Fig. (6.6) and in Fig. (6.8) respectively. TE modes are shown in Fig. (6.6a) and Fig. (6.8a), TM modes are shown in Fig. (6.6b) and Fig. (6.8b), and mixed modes are shown in Fig. (6.6c) and Fig. (6.8c).

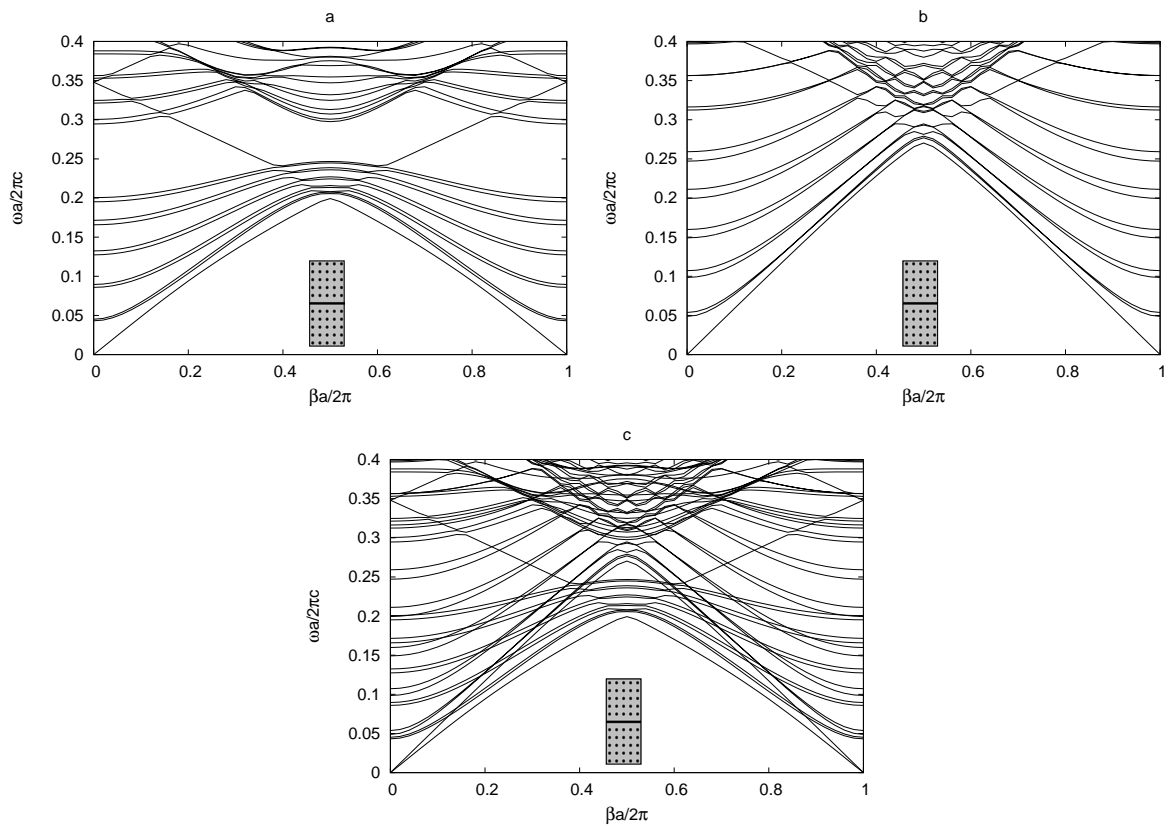


Figure 6.6. 2D-LDWG band diagrams of "silica silicon waveguide" for TE modes, TM modes and for mixed modes.

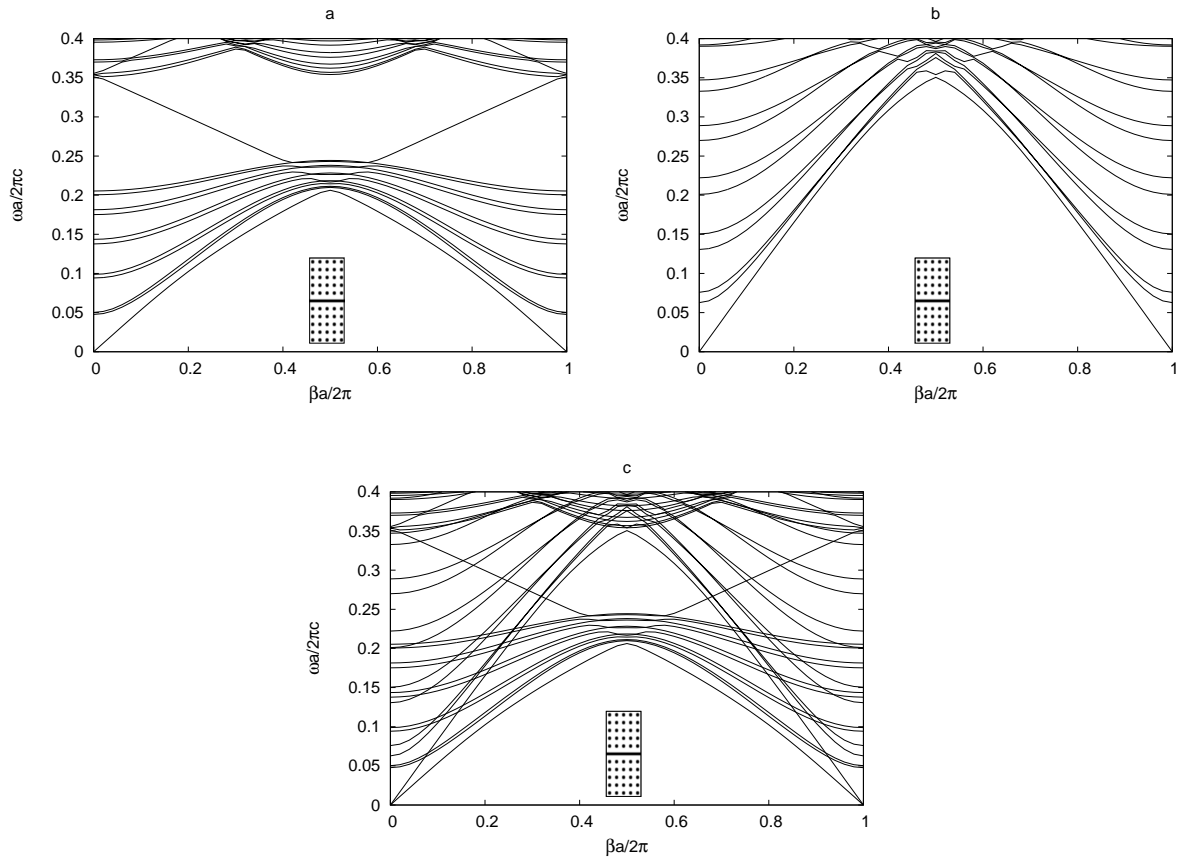


Figure 6.8. 2D-LDWG band diagrams of "air silicon waveguide" for TE modes, TM modes and for mixed modes.

But for the photonic crystal slab modes in 3D, they can not be divided into two polarizations. They are included all the modes. That means one can not get band structures for slab modes separately as Fig. (6.6a) or Fig. (6.6b), but one gets only graphic as Fig. (6.6c). This is because of the lack of translational symmetry in the vertical direction. Therefore the slab modes are classified in terms of transverse electric like (TE-like) modes and transverse magnetic like (TM-like) modes.

Looking the field components of the modes, we can understand if the mode is TE-like or TM-like. The modes and corresponding field components are shown in the table (6.2), the propagating wave assumed in the \hat{x} – direction.

Mode	E_y	E_z	E_x	H_y	H_z	H_x
TE	$\neq 0$	$\neq 0$	0	$\neq 0$	$\neq 0$	$\neq 0$
TE-like	$\neq 0$	$\neq 0$	≈ 0	$\neq 0$	$\neq 0$	$\neq 0$
TM	$\neq 0$	$\neq 0$	$\neq 0$	$\neq 0$	$\neq 0$	0
TM-like	$\neq 0$	$\neq 0$	$\neq 0$	$\neq 0$	$\neq 0$	≈ 0

Table 6.2. Mode polarizations.

In the rest of the work, we study on TE-like modes. The table shows the difference between TE mode and TE-like modes for electric field components. The difference is while E_x component in TE mode equal to 0, for TE-like modes E_x component is close to 0.

6.4. Mode Coupling

After mode polarization another important issue for our designs is the mode coupling. For the guidance of light, the proposed system has two important elements:

- 1) The guided modes of 1D-LDWG slabs and 2D-LDWG slabs must be coupled. So we want to find the guided mode which will propagate in these structures in the same time. On account of this it is important to see matched band diagram to decide at which values it is possible to work.
- 2) The chosen coupled frequency must be in the 2D-LDWG slabs band gap to prevent loss for 90° turning.

By providing these two items we will design silica silicon waveguide slab and air silicon waveguide slab.

6.5. Silica Silicon Waveguide Slab

In this section we will present silica silicon waveguide slab for symmetric and asymmetric cases. For each case we will show the band diagrams, mode coupling of the structures.

6.5.1. Symmetric Silica Silicon Waveguide Slab

We show the symmetric silica silicon waveguide slab in Fig. (6.9). Here the waveguide is surrounded by air from above and below. At the middle of the structure, silica is used as a background material and silicon rods and slabs are immersed in the silica background.

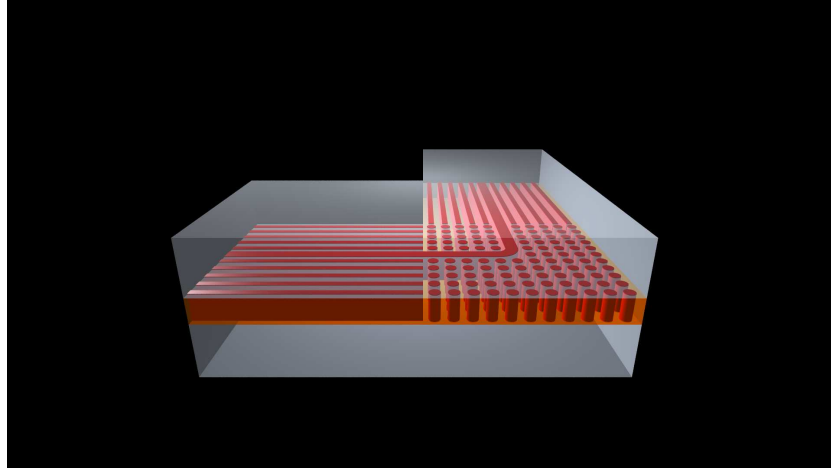


Figure 6.9. Symmetric silica silicon waveguide slab.

The band diagram of the symmetric silica silicon waveguide slab are studied for 1D-LDWG slab and 2D-LDWG slab, both for symmetric case.

The Figs. (6.10) and (6.11) show band diagrams of 1D-LDWG in Fig. (6.10) and 1D-LDWG slab in Fig. (6.11). Here simultaneously two figures are shown together. The reason is that we want to do comparison between the two. The Fig. (6.10) shows silica silicon waveguide for TE modes, in this figure the first fundamental TE mode is the guided mode in the line defect. The Fig. (6.11) shows silica silicon waveguide slab for TE-like modes, in this figure the first fundamental TE-like mode is the guided mode in the line defect. If we compare the two figures, we see that Fig. (6.11) has extra modes because of the 3 dimensionality of the structure and also represents a mixture of TE-like and TM-like modes.

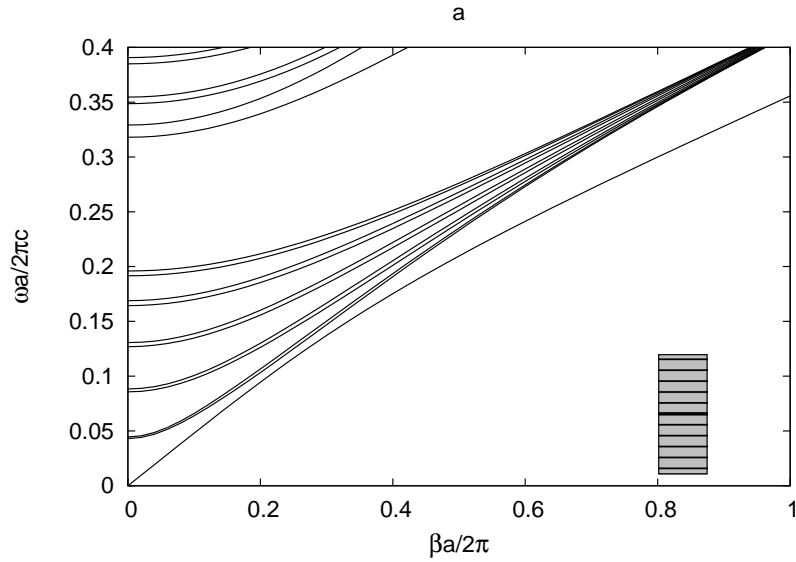


Figure 6.10. Band diagrams of silica silicon waveguide (1D-LDWG)

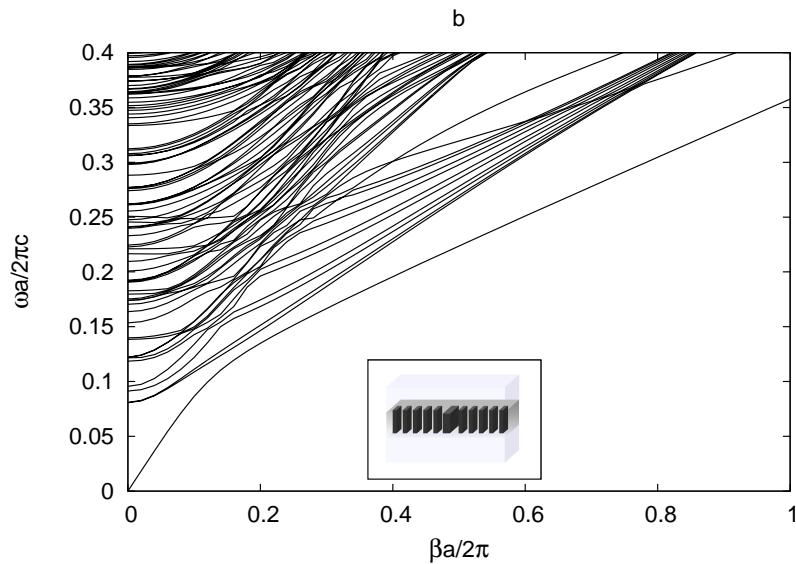


Figure 6.11. Band diagrams of symmetric silica silicon waveguide slab (1D-LDWG Slab).

The Figs. (6.12) and (6.13) show band diagrams of 2D-LDWG in Fig. (6.12) and 2D-LDWG slab in Fig. (6.13). The Fig. (6.12) shows silica silicon waveguide for mixed modes. The Fig. (6.13) shows silica silicon waveguide slab for mixed modes. When we compare the band diagrams of 2D-LDWG and 2D-LDWG slab, we see while the band gap (for mixed modes) for 2D-LDWG in Fig. (6.12) is wide, the band gap for symmetric 2D-LDWG slab gets narrow. Also if we compare the two figures, we see that Fig. (6.13) has extra modes because of the 3 dimensionality of the structure. Nevertheless the shapes of the curves preserved similar in 2D and 3D cases.

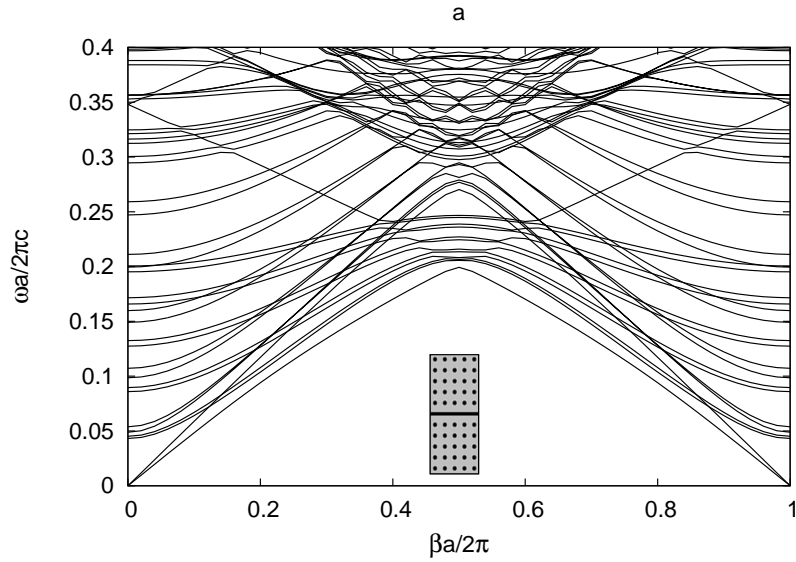


Figure 6.12. Band diagrams of silica silicon waveguide (2D-LDWG)

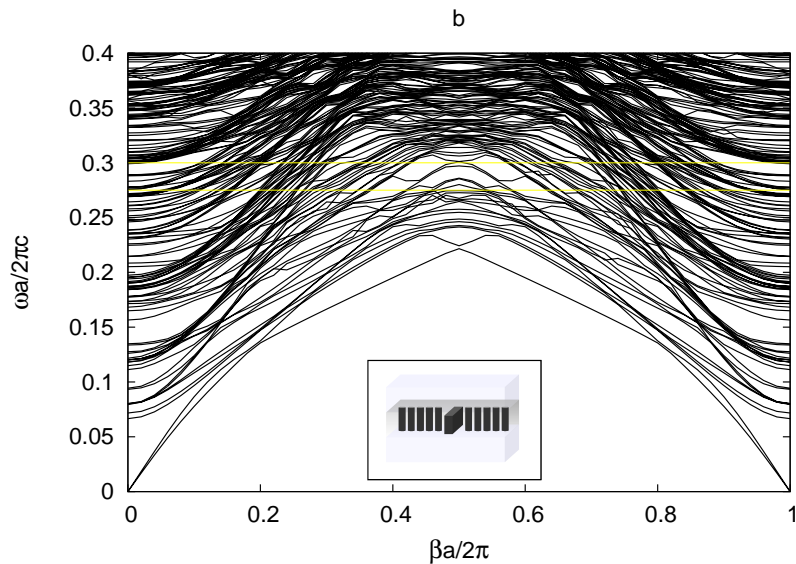


Figure 6.13. Band diagrams of symmetric silica silicon waveguide slab (2D-LDWG Slab).

As stated previously for the guidance of light, the guided modes of 1D-LDWG slabs and 2D-LDWG slabs must be coupled. Because we want to find the guided mode which will propagate in these structures in the same time. On account of this we show in Fig. (6.14) the band diagrams of 1D-LDWG slab is with green color and 2D-LDWG slab is with black color. The red dashed lines show matched line defect modes that is guided in the line defect, and also guided in this defect even in the absence of photonic crystal. As mentioned earlier, there exist band gaps for TE-like modes between horizontal yellow lines. Consequently, the red dashed lines through the band gap give us the TE-like mode, which will be guided in the

line defect and won't be reflected during the 90° turning.

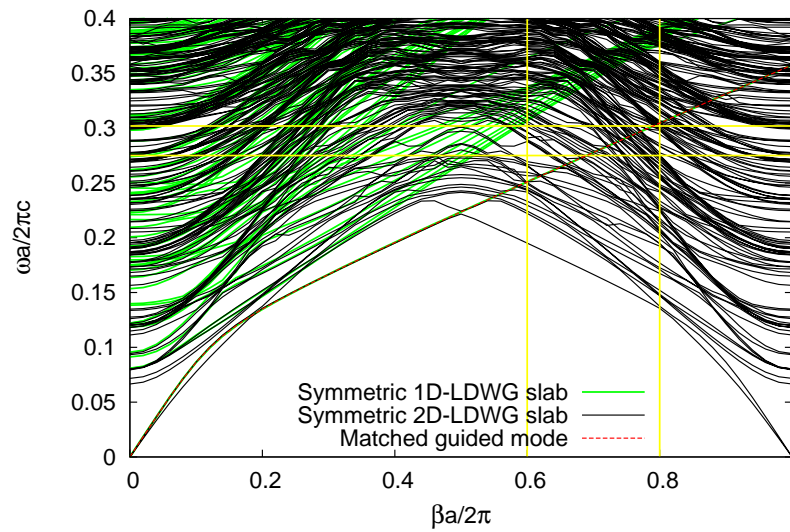


Figure 6.14. Matched band diagrams of symmetric silica silicon waveguide slab.

6.5.2. Asymmetric Silica Silicon Waveguide Slab

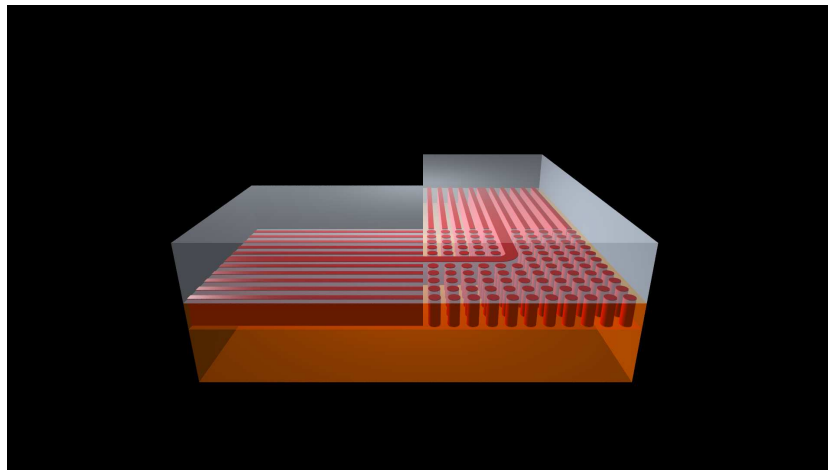


Figure 6.15. Asymmetric silica silicon waveguide slab.

We present the asymmetric silica silicon waveguide slab in Fig. (6.15). It lies on a silica substrate, that breaks the mirror symmetry in the vertical direction because of the different dielectric constants of air and silica.

The band diagram of the asymmetric silica silicon waveguide slab are studied for 1D-LDWG slab and 2D-LDWG slab, both for asymmetric case.

The Fig. (6.16) shows silica silicon waveguide slab for TE-like modes, in this figure the first fundamental TE-like mode is the guided mode in the line defect. The Fig. (6.17) shows band diagrams of asymmetric silica silicon waveguide slab for mixed modes.

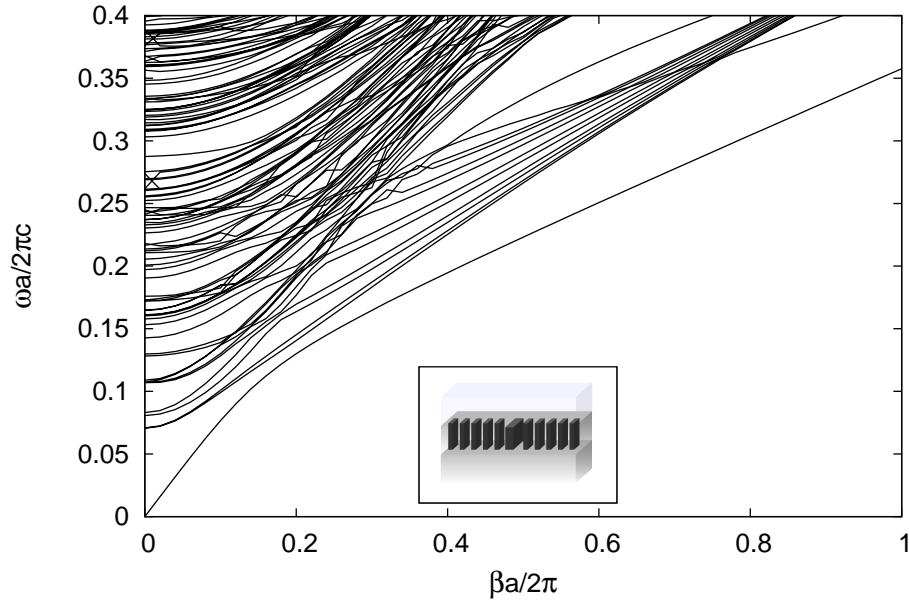


Figure 6.16. Band diagram of asymmetric silica silicon waveguide, 1D-LDWG Slab, mixed modes.

For the guidance of light, the guided modes of 1D-LDWG slabs and 2D-LDWG slabs must be coupled. Because we want to find the guided mode which will propagate in these structures in the same time. On account of this we show in Fig. (6.18) the band diagrams of 1D-LDWG slab is with green color and 2D-LDWG slab is with black color. The red dashed lines show matched line defect modes that is guided in the line defect, and also guided in this defect even in the absence of photonic crystal. As mentioned earlier, there exist band gaps for TE-like modes between horizontal yellow lines. Consequently, the red dashed lines through the band gap give us the TE-like mode, which will be guided in the line defect and won't be reflected during the 90° turning.

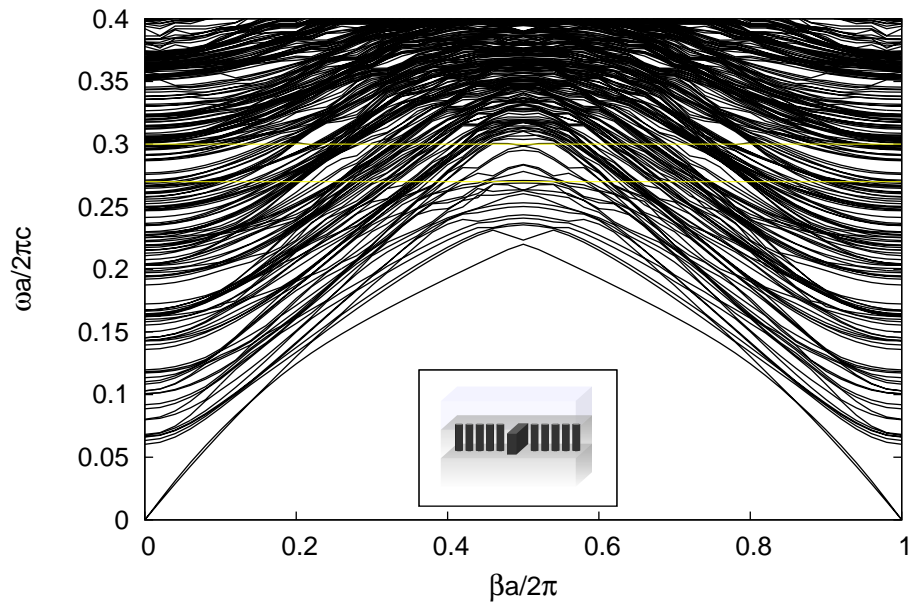


Figure 6.17. Band diagram of asymmetric silica silicon waveguide slab (2D-LDWG Slab).

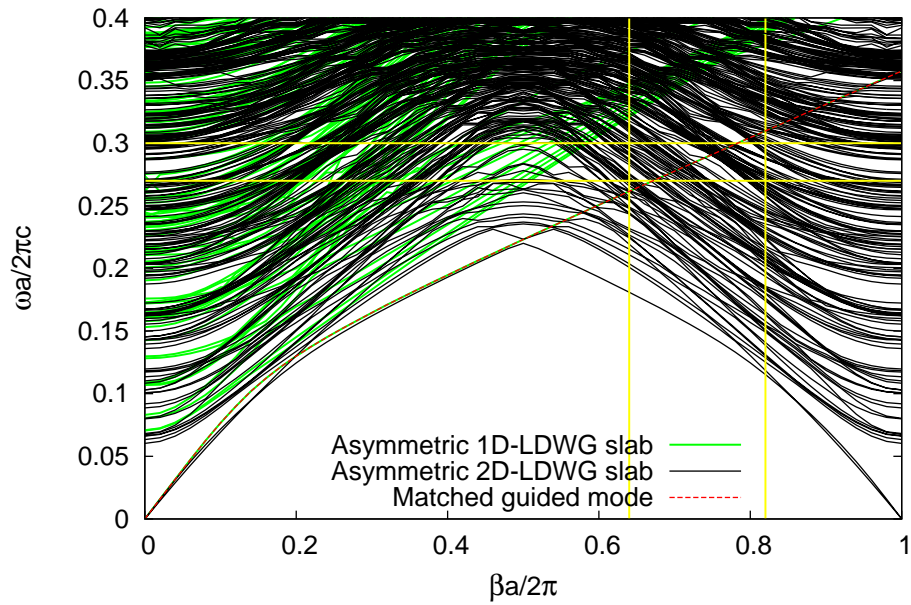


Figure 6.18. Matched band diagrams of asymmetric silica silicon waveguide slab.

6.6. Air Silicon Waveguide Slab

In this section we will present air silicon waveguide slab for symmetric and asymmetric cases. For each case we will show the band diagrams, mode coupling for the structures.

6.6.1. Symmetric Air Silicon Waveguide Slab

We show the symmetric air silicon waveguide slab in Fig. (6.19). Here the waveguide is surrounded by air from above and below. At the middle of the structure, air is used as a background material and silicon rods and slabs are immersed in the air background.

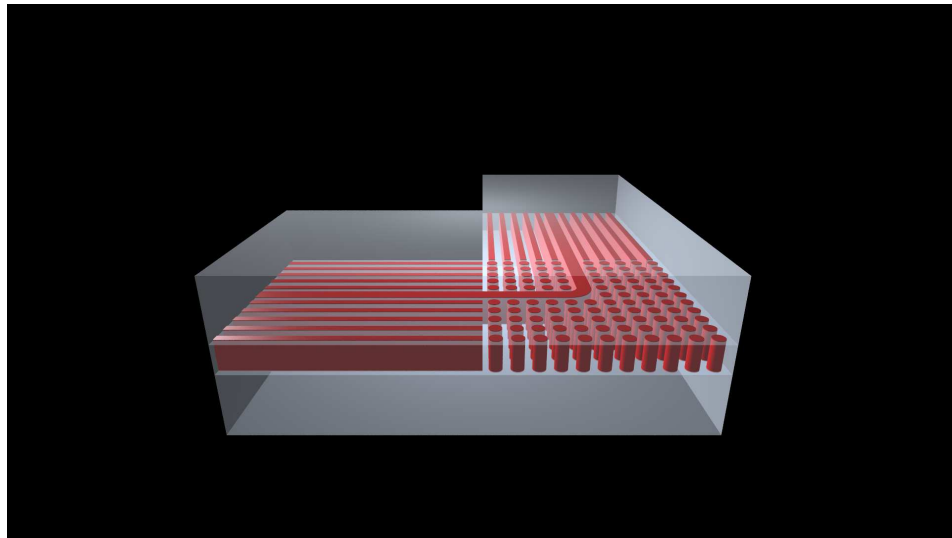


Figure 6.19. Symmetric air silicon waveguide slab.

The band diagram of the symmetric air silicon waveguide slab are studied for 1D-LDWG slab and 2D-LDWG slab, both for symmetric case.

The Fig. (6.21) shows band diagrams of 1D-LDWG in Fig. (6.21a) and 1D-LDWG slab in Fig. (6.21b). Here simultaneously two figures are shown together. The reason is that we want to do comparison between the two. The Fig. (6.21a) shows silica silicon waveguide for TE modes, in this figure the first fundamental TE mode is the guided mode in the line defect. The Fig. (6.21b) shows silica silicon waveguide slab for TE-like modes, in this figure the first fundamental TE-like mode is the guided mode in the line defect. If we compare the two figures, we see that Fig. (6.21b) has extra modes because of the 3 dimensionality of the structure and also represents a mixture of TE-like and TM-like modes.

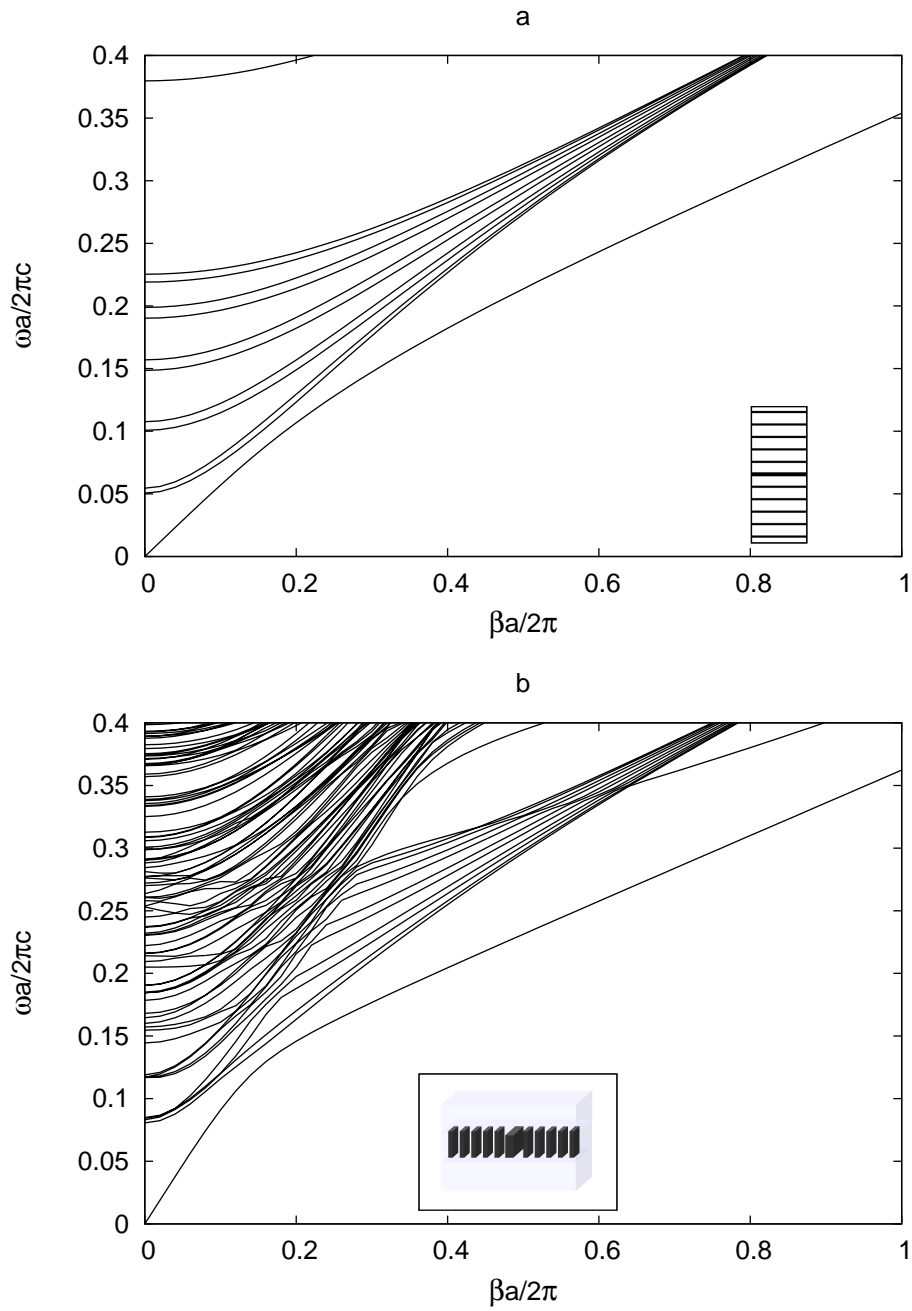


Figure 6.21. Band diagrams of air silicon waveguide (1D-LDWG) and symmetric air silicon waveguide slab (1D-LDWG Slab).

The Fig. (6.23) shows band diagrams of 2D-LDWG in Fig. (6.23a) and 2D-LDWG slab in Fig. (6.23b). The Fig. (6.23a) shows air silicon waveguide for mixed modes. The Fig. (6.23b) shows air silicon waveguide slab for mixed modes. When we compare the band diagrams of 2D-LDWG and 2D-LDWG slab, we see while the band gap (for mixed modes) for 2D-LDWG in Fig. (6.23a) is wide, the band gap for symmetric 2D-LDWG slab gets narrow. Also if we compare the two figures, we see that Fig. (6.23b) has extra modes because of the 3 dimensionality of the structure. Nevertheless the shapes of the curves preserved similar in 2D and 3D cases.

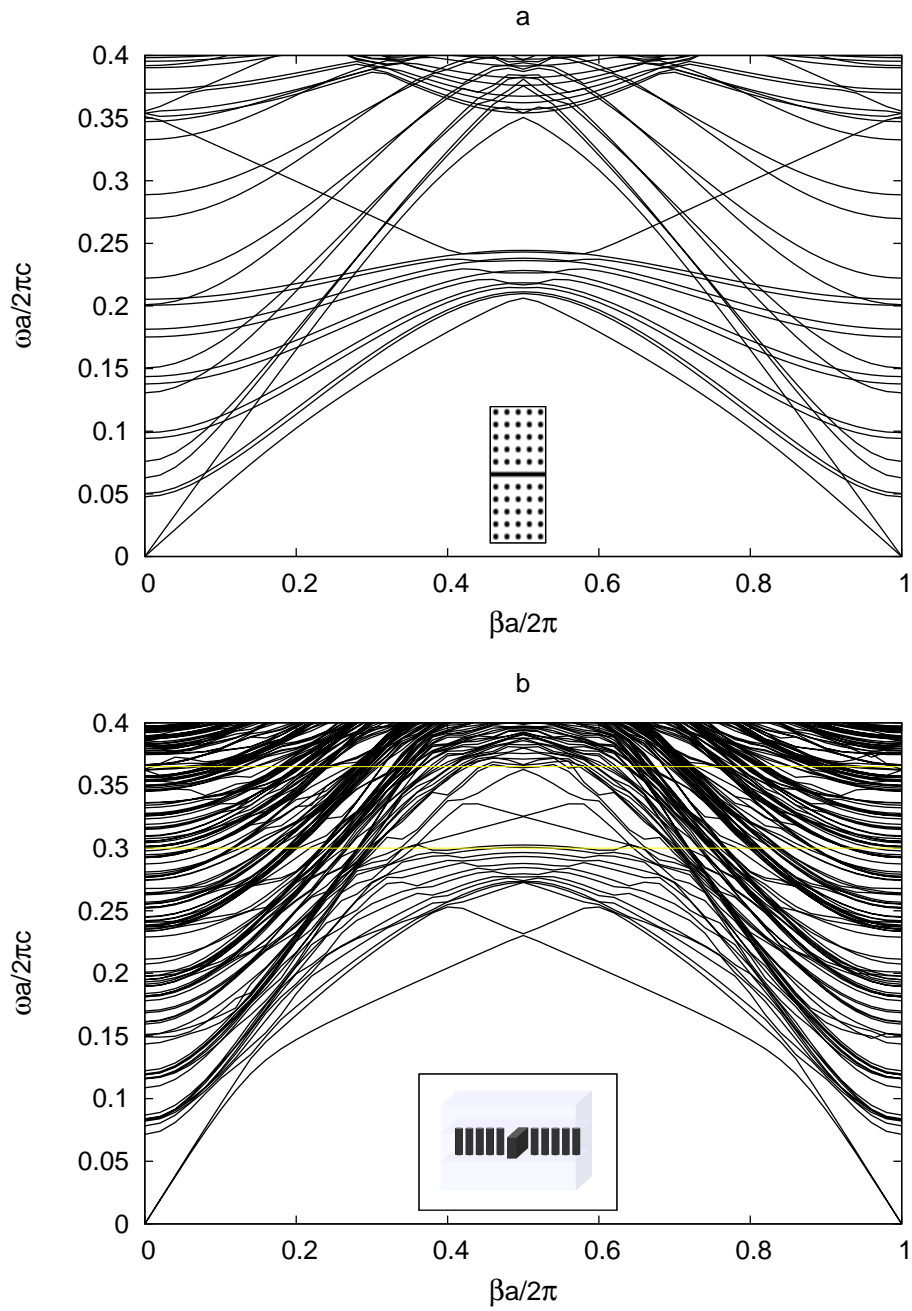


Figure 6.23. Band diagrams of air silicon waveguide (2D-LDWG) and symmetric air silicon waveguide slab (2D-LDWG Slab).

As stated previously for the guidance of light, the guided modes of 1D-LDWG slabs and 2D-LDWG slabs must be coupled. Because we want to find the guided mode which will propagate in these structures in the same time. On account of this we show in Fig. (6.24) the band diagrams of 1D-LDWG slab is with green color and 2D-LDWG slab is with black color. The red dashed lines show matched line defect modes that is guided in the line defect, and also guided in this defect even in the absence of photonic crystal. As mentioned earlier, there exist band gaps for TE-like modes between horizontal yellow lines. Consequently, the red dashed lines through the band gap give us the TE-like mode, which will be guided in the line defect and won't be reflected during the 90° turning.

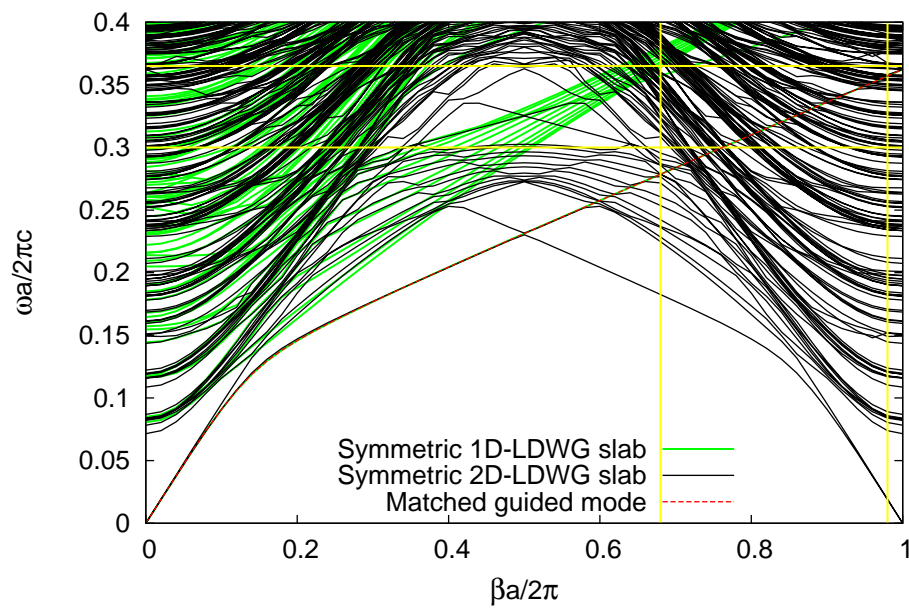


Figure 6.24. Matched band diagrams of symmetric air silicon waveguide slab.

6.6.2. Asymmetric Air Silicon Waveguide Slab

We present the asymmetric air silicon waveguide slab in Fig. (6.25). It lies on a silica substrate, that breaks the mirror symmetry in the vertical direction because of the different dielectric constants of air and silica.

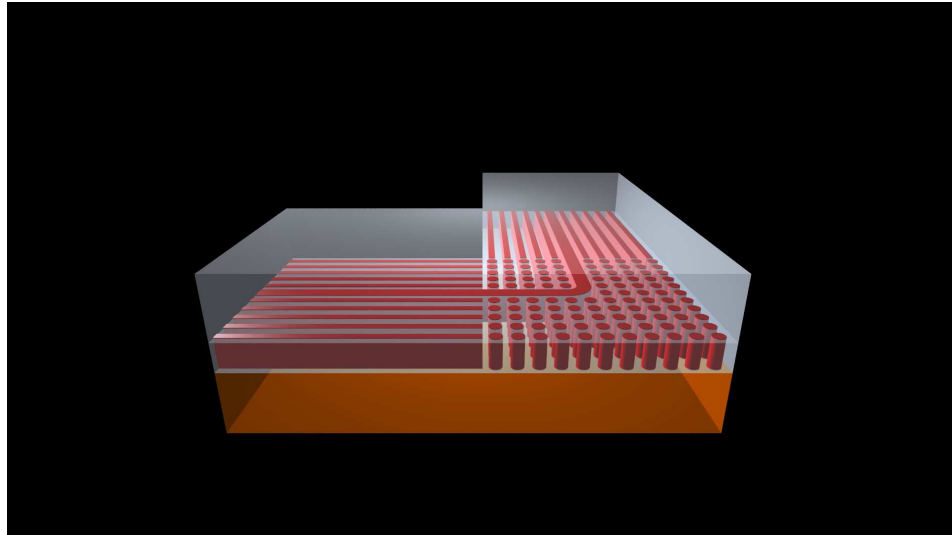


Figure 6.25. Asymmetric air silicon waveguide slab.

The band diagram of the asymmetric air silicon waveguide slab are studied for 1D-LDWG slab and 2D-LDWG slab, both for asymmetric case.

The Fig. (6.26) shows air silicon waveguide slab for TE-like modes, in this figure the first fundamental TE-like mode is the guided mode in the line defect. The Fig. (6.27) shows band diagrams of asymmetric air silicon waveguide slab for mixed modes.

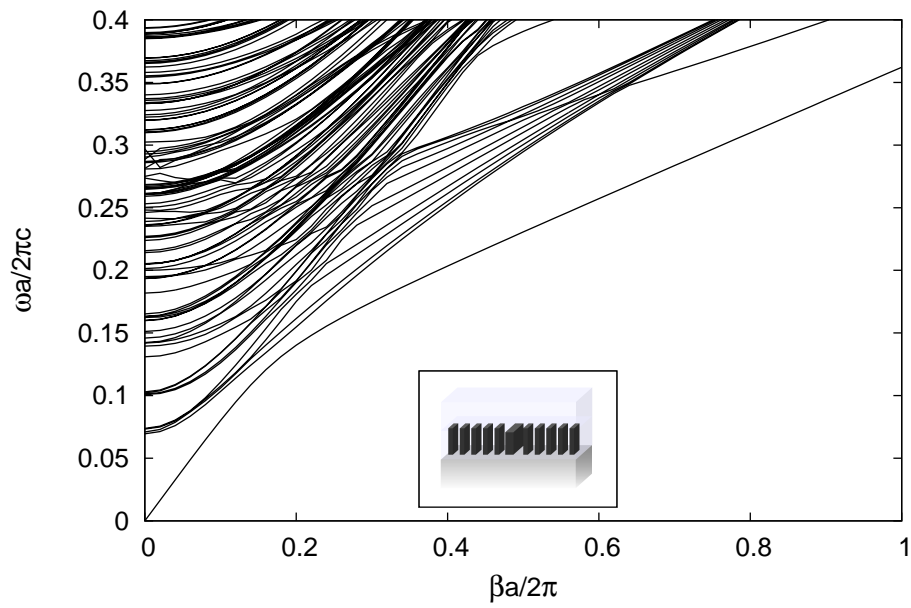


Figure 6.26. Band diagram of asymmetric air silicon waveguide, 1D-LDWG Slab, mixed modes.

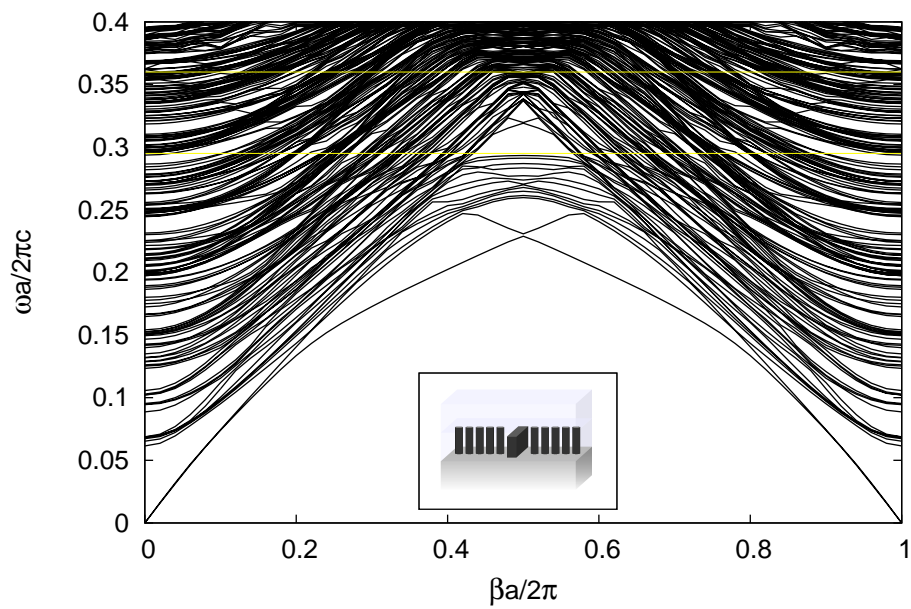


Figure 6.27. Band diagram of asymmetric air silicon waveguide slab (2D-LDWG Slab).

For the guidance of light, the guided modes of 1D-LDWG slabs and 2D-LDWG slabs must be coupled. Because we want to find the guided mode which will propagate in these structures in the same time. On account of this we show in Fig. (6.28) the band diagrams of 1D-LDWG slab is with green color and 2D-LDWG slab is with black color. The red dashed lines show matched line defect modes that is guided in the line defect, and also guided in this defect even in the absence of photonic crystal. As mentioned earlier, there exist band gaps for TE-like modes between horizontal yellow lines. Consequently, the red dashed lines through the band gap give us the TE-like mode, which will be guided in the line defect and won't be reflected during the 90° turning.

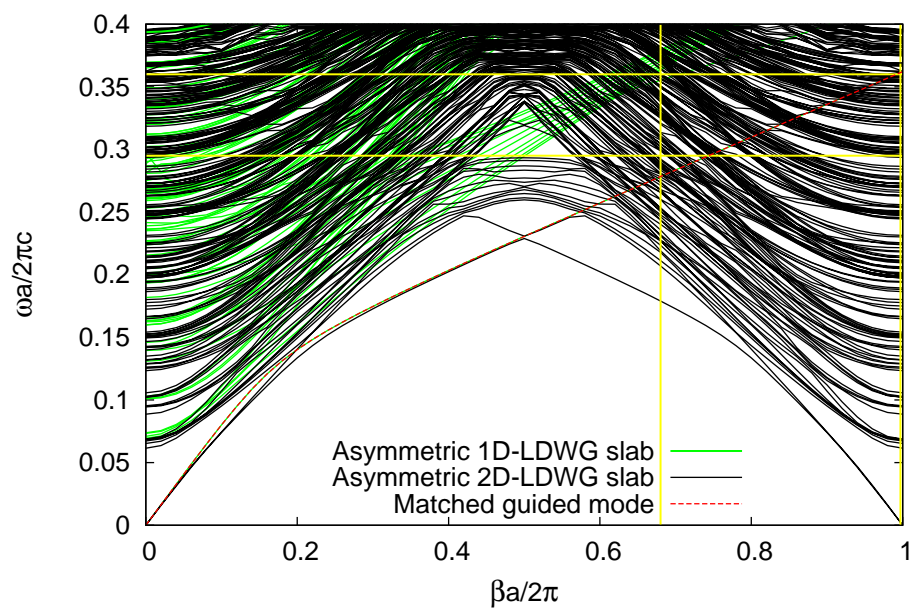


Figure 6.28. Matched band diagrams of asymmetric air silicon waveguide slab.

6.7. Transmission Results

The next step is time domain simulation to prove if the designs works. Above, we give the parameters for our proposed structure and also we shown the band diagrams for each of the structures. Now we want to understand how much power turns the bend. To know this we need to find transmission. Transmission of the bend can be defined as the ratio of the total output flux measured after bend, P_o , to total input flux for the corresponding 1D-LDWG slab, P_i , which is given by

$$T = P_o/P_i.$$

Therefore we calculated flux on yz-plane of the waveguide once for the straight 1D-LDWG slab, and on xz-plane of the waveguide once for after the bend for each of the structures.

The FDTD simulations have been performed using MEEP [22], which gives convenience in using custom sources. We used a current source in the next form

$$\mathbf{J}_m(\mathbf{r}, t) = \delta(x - x_s)\mathbf{H}(y, z, \omega)exp\left[\frac{-(t - t_0)}{2\sigma^2}\right] \exp(-i\omega t)$$

where $\mathbf{J}_m(\mathbf{r}, t)$ is a monochromatic source located at $x = x_s$ of frequency ω . It is enveloped in a Gaussian packet with width $\Delta\omega = 1/\sigma$, where σ is wavelength, in the frequency domain. $\mathbf{H}(y, z, \omega)$ is the guided mode of the 1D-LDWG slab at the center frequency ω . We use $H_x(y, z, \omega)$, $H_y(y, z, \omega)$, $H_z(y, z, \omega)$ to generate a current source is in yz-plane in order to excite TE-like modes. We call this source as “mode source”. The mode source excites only itself, by this way the initial straight segment can be made very short, so considerably reducing the simulation time, additionally yielding much more correct results for transmission. Gaussian source is adjusted for the flux calculations until well after the fields have decayed to 1/10.000th of their peak values at the end of the waveguide where the flux-regions have been placed.

We analysed the role of the interface between 1D-LDWG slab and 2D-LDWG slab, which is previously defined as d_{separ} . That’s why while calculating the flux we take flux once for the straight 1D-LDWG slab, and once for the structure in the Fig. (6.29). For each case calculation dimensions are identical and locations of the flux regions are in the same place. The transmission is taken as the ratio of the fluxes and measured from $-0.4a$ to $1a$ increasing in $0.1a$ steps. We observed that the transmission results averagely changed only one percent. Therefore we worked with the same d_{separ} value for all structures, it is $d_{separ} = 0.2a$.

In Fig. (6.30), we present the snapshots from our simulations of ”silica silicon waveguide”, symmetric slab. The figure on the left is a snapshot when the frequency $\omega a/2\pi c =$

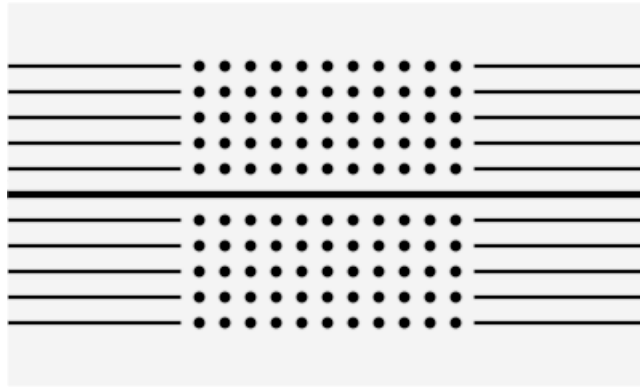


Figure 6.29. $z = 0$ slice from 3D slab is shown with $d_{separ} = 0.2a$. All parameters are the same described for 3 dimensional system.

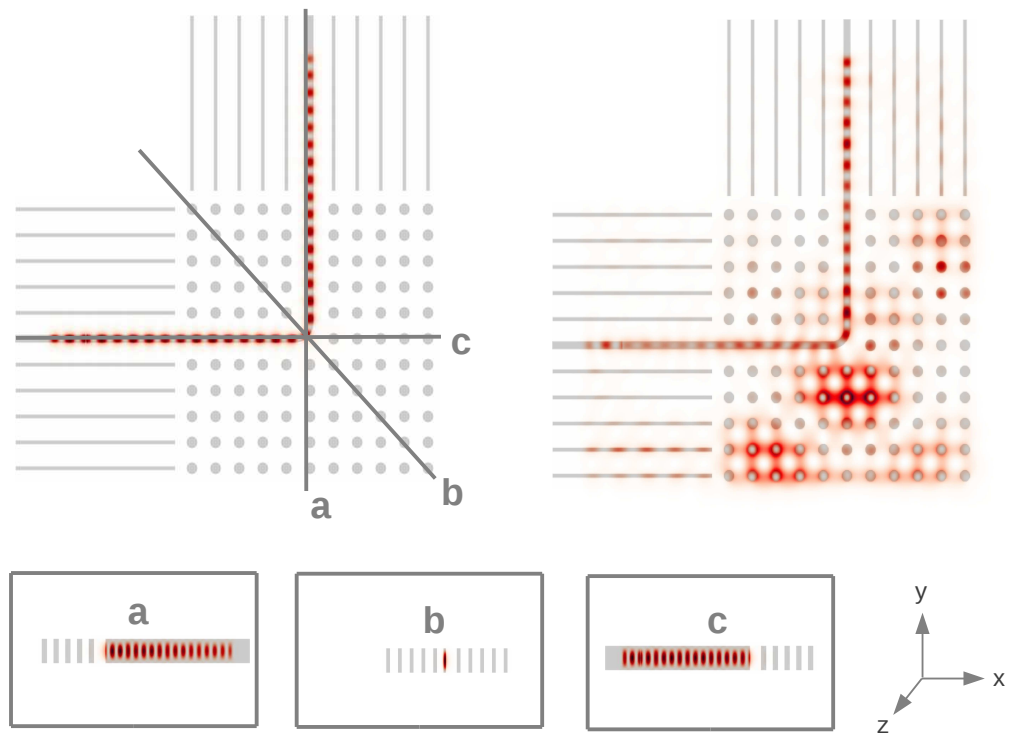


Figure 6.30. FDTD simulations of $z = 0$ slice from "silica silicon waveguide" symmetric slab. On the left the slab is at the frequency of $\omega a / 2\pi c = 0.2967$ which is in the band gap. a, b and c show different plane sections for the figure on the left. On the right the slab is at the frequency of $\omega a / 2\pi c = 0.2633$ which is below the band gap. The wave is gaussian with width $\Delta(\omega a / 2\pi c) = 0.1$.

0.2967 is in the band gap $0.2745 < \omega a/2\pi c < 0.3077$ of the 2D-LDWG structure. Therefore there is no visible penetration into the corner element. The transmission is nearly lossless (% 97.23) as it is clear from the plane sections a , b and c of the structure. In contrast the figure on the right is a snapshot when the frequency $\omega a/2\pi c = 0.2633$, which is below the band gap of the 2D-LDWG structure. This time the radiation penetrates visibly into the photonic crystal and corner element so there is large leakage and transmission is low (% 57.06).

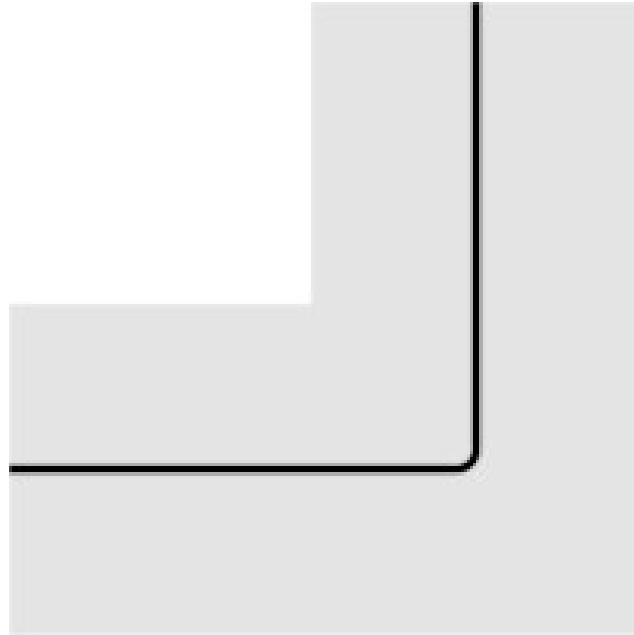


Figure 6.31. $z = 0$ slice from 3D single slab is shown. Single slab is a waveguide without photonic crystal assistance.

Fig. (6.32) shows the transmission for the "silica silicon waveguide" as function of frequency. The results are given for through the symmetric photonic crystal (red filled circles), symmetric single slab (green blank circles), asymmetric photonic crystal (blue filled squares) and asymmetric single slab (pink blank squares). Here single slab means a slab waveguide without photonic crystal assistance as shown in Fig. (6.31). The transmission of the symmetric photonic crystal is largest for frequencies inside the 2D-LDWG slab bandgap which lies in the range $0.2745 < \omega a/2\pi c < 0.3077$. On the other hand the transmission of the asymmetric photonic crystal is smaller comparing the symmetric photonic crystal for frequencies inside the 2D-LDWG slab bandgap which lies in the range $0.2740 < \omega a/2\pi c < 0.3018$.

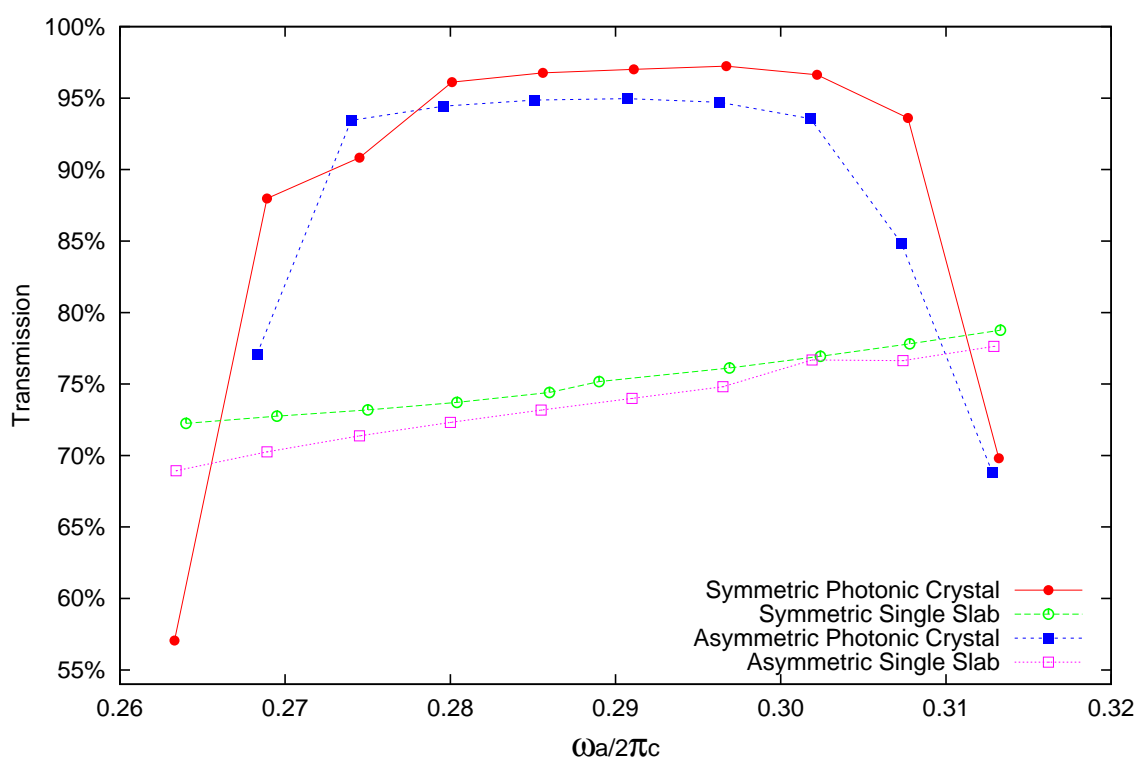


Figure 6.32. Transmission result of MEEP according to different values of $\omega a/2\pi c$ for the "silica silicon waveguide". All parameters are the same described for 3D system.

Fig. (6.33) shows the transmission for the "air silicon waveguide" as function of frequency. The results are given for through the symmetric photonic crystal (red filled circles), symmetric single slab (green blank circles), asymmetric photonic crystal (blue filled squares) and asymmetric single slab (pink blank squares). Like the previous transmission results the symmetric photonic crystal is largest for the frequencies inside the 2D-LDWG slab bandgap

which lies in the range $0.2985 < \omega a/2\pi c < 0.3790$. The transmission of the asymmetric photonic crystal is smaller comparing the symmetric photonic crystal for frequencies inside the 2D-LDWG slab bandgap which lies in the range $0.3035 < \omega a/2\pi c < 0.3683$.

Let's show the FDTD simulations of the symmetric silicon silica waveguide slab at a frequency out of the photonic band gap $\tilde{\omega} = 0.2633$ in Fig. (6.34) and at a frequency in the photonic band gap, $\tilde{\omega} = 0.2966$ in Fig. (6.35). Here we can see the effect of the photonic band gap to bend light.

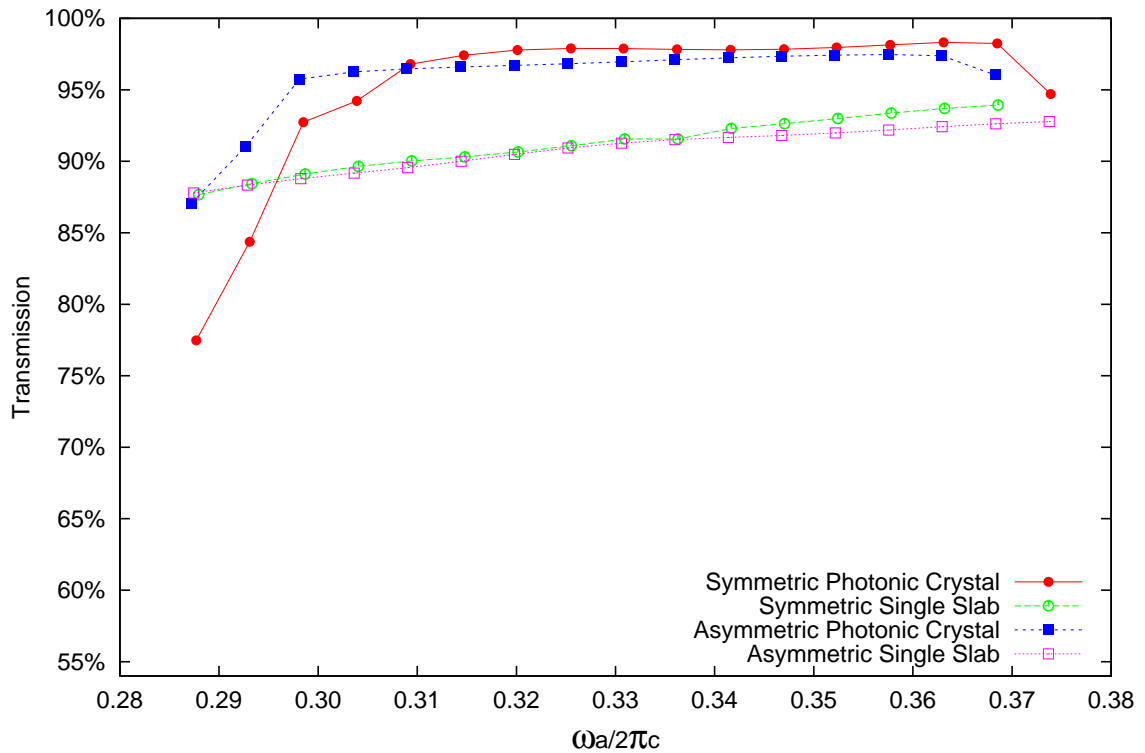
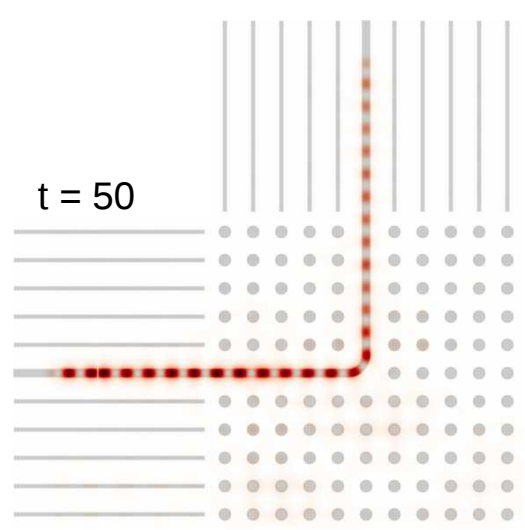
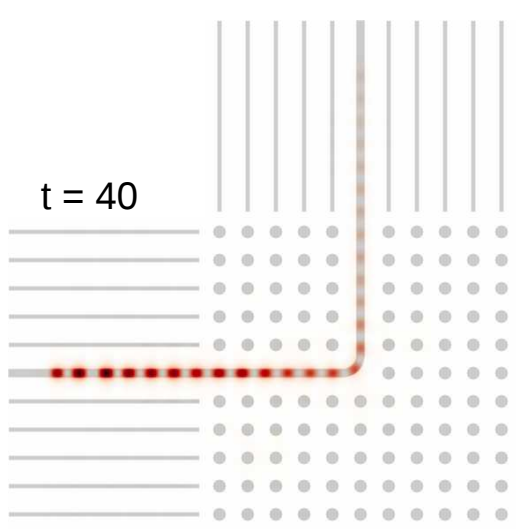
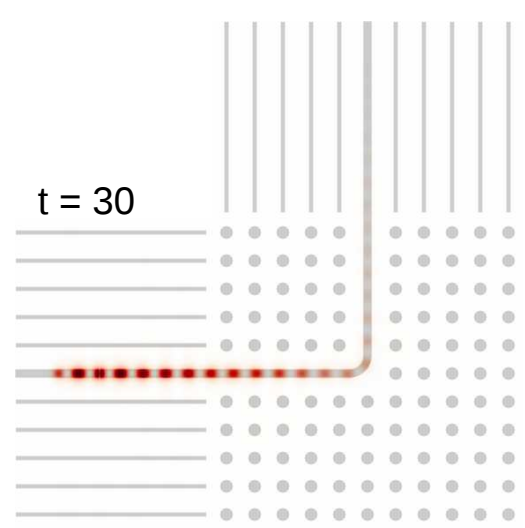
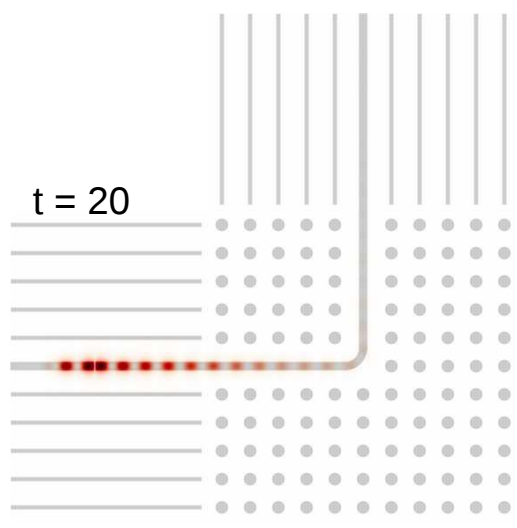
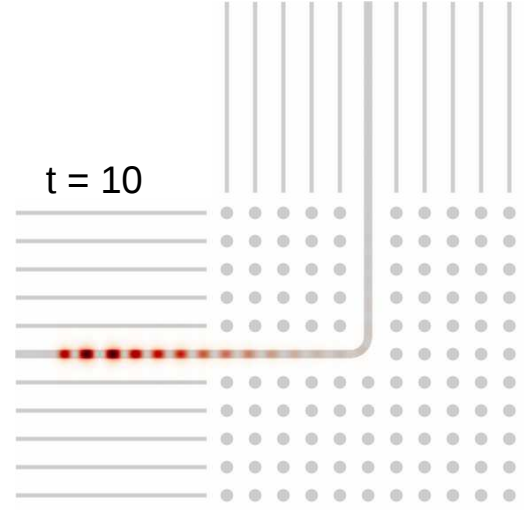
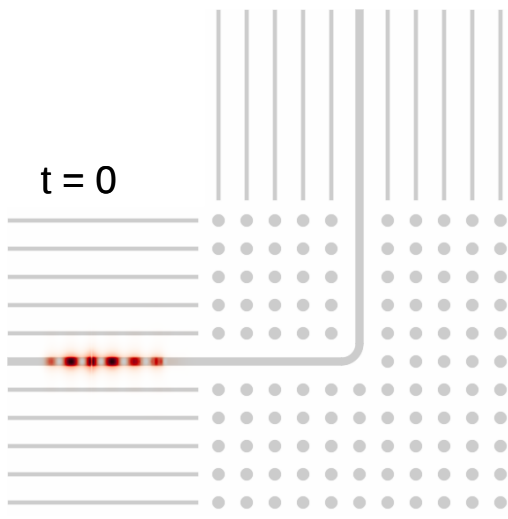


Figure 6.33. Transmission result of MEEP according to different values of $\omega a/2\pi c$ for the "air silicon waveguide". All parameters are the same described for 3D system.

As a result we worked for TE modes in 1D-LDWG for the straight sections and for TE-like modes in 2D-LDWG for the corner element. Here we present the maximum values of the transmission results for worked examples in the Table (6.3). The best transmission is obtained for symmetric air silicon waveguide slab is %98.32 but since in the real world this design is not possible this data just given for theoretical realization. The second best transmission is obtained for asymmetric air silicon waveguide slab is %97.43. If one examines where the losses arise, they occur in two places. \approx %0.44 is dispersed at the transition between the



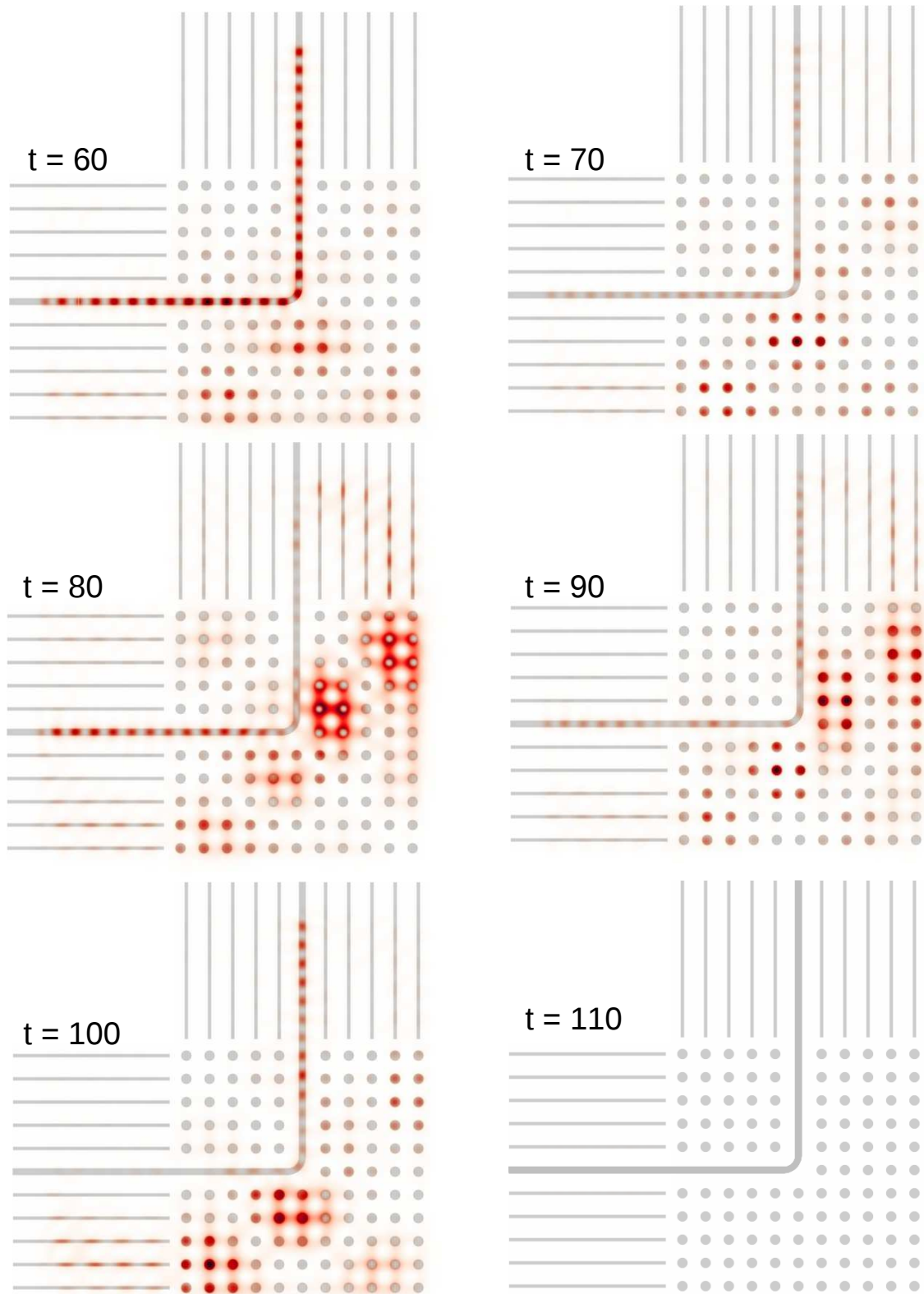
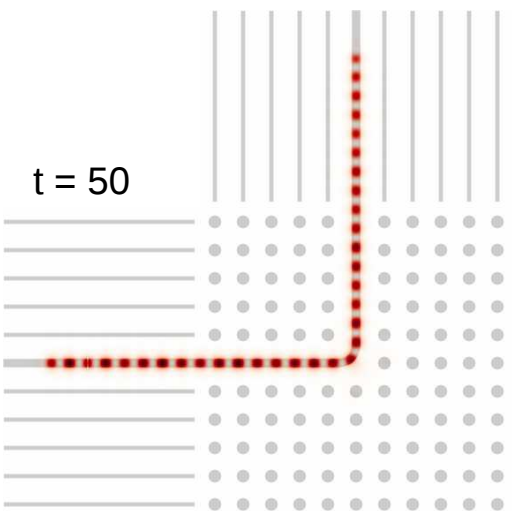
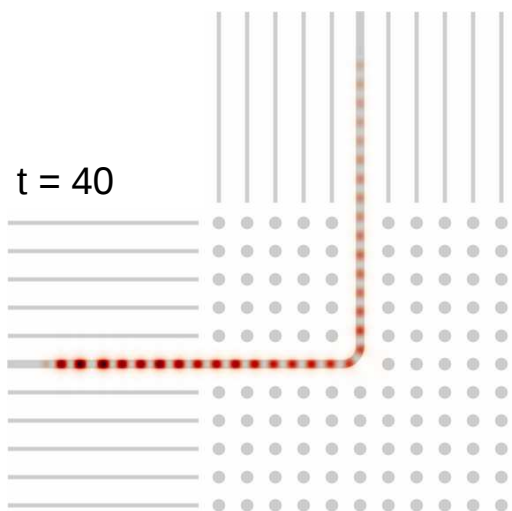
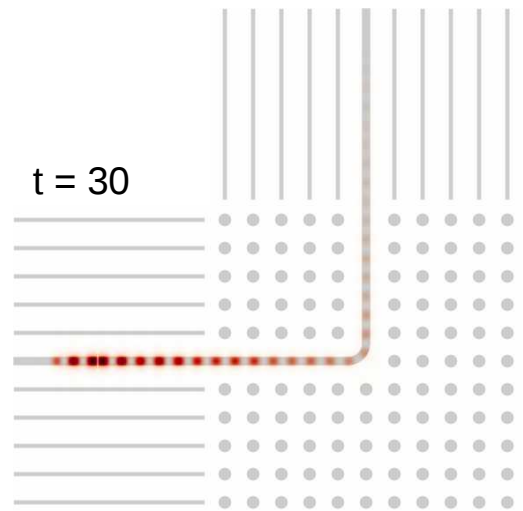
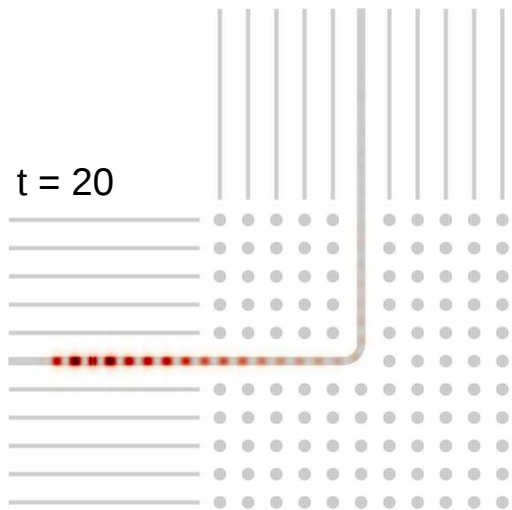
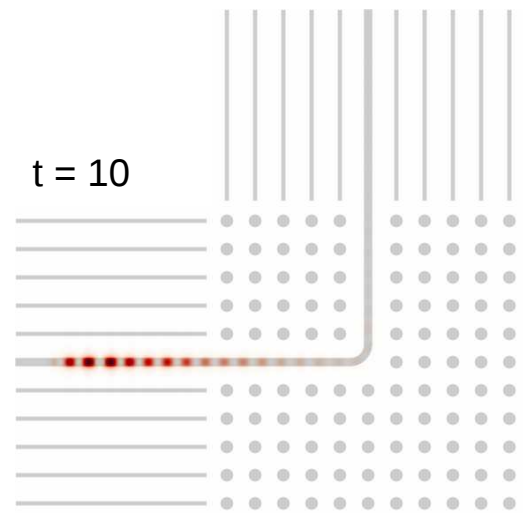
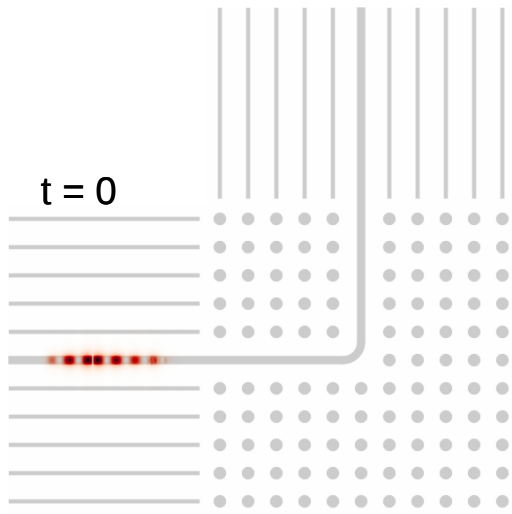


Figure 6.34. FDTD simulations of the symmetric silicon silica waveguide slab at a frequency out of the photonic band gap, $\tilde{\omega} = 0.2633$.



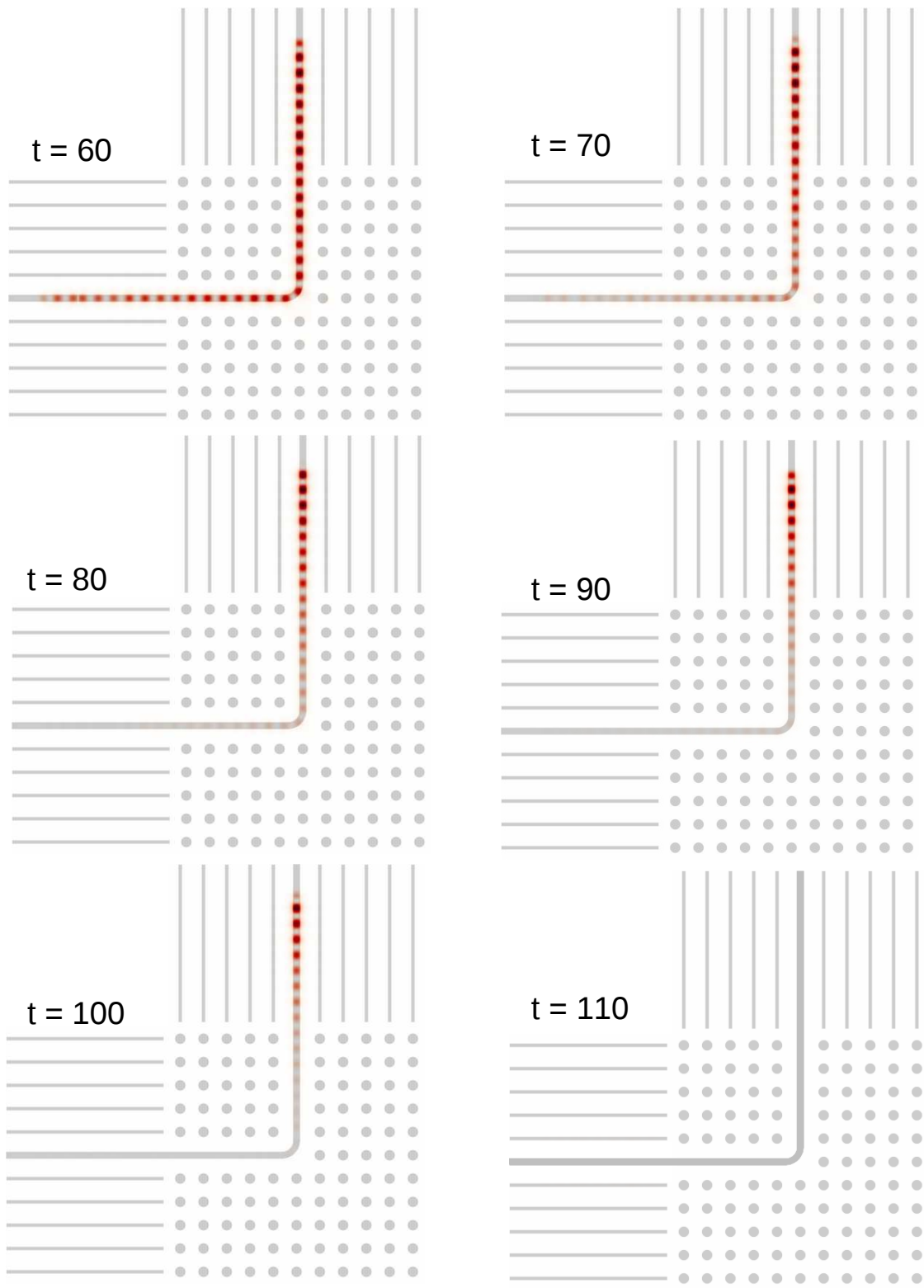


Figure 6.35. FDTD simulations of the symmetric silicon silica waveguide slab at a frequency in the photonic band gap, $\tilde{\omega} = 0.2966$.

Structure types	Frequency ($\omega a/2\pi c$)	Obtained best transmission (%)	Lost in the transition between 1D-LDWS and 2D-LDWGS (%)	Lost during 90° bend (%)
sss-wgs	0.2967	97.23	1	1.77
ass-wgs	0.2907	94.96	1.16	3.88
sas-wgs	0.3685	98.32	0.45	1.23
aas-wgs	0.3522	97.43	0.44	2.13

Table 6.3. The best transmission results.

structures and $\approx 2.13\%$ is reflected at the moment of turning. The maximum transmission is obtained for symmetric silica silicon waveguide slab is 97.23% . $\approx 1\%$ is dispersed at the transition between the structures and $\approx 1.77\%$ is reflected at the moment of turning. The maximum transmission is obtained for asymmetric silica silicon waveguide slab is 94.96% . $\approx 1.16\%$ is dispersed at the transition between the structures and $\approx 3.88\%$ is reflected at the moment of turning.

CHAPTER 7

CONCLUSION

We analyzed mathematical modeling of light propagation in Photonic Crystal Waveguide Slab. We described Maxwell's equations in periodic media with proper boundary conditions as generalized eigenvalue problem for Hermitian operators. Two types of periodic media we modeled; 1D-LDWGS and 2D-LDWS. Using unitary transformation we reduced problem to block diagonal Hermitian eigenvalue problem. By combination of basic geometrical photonic crystal slabs in 1D and 2D, we constructed some waveguides in silica substrates. Solving the problem using the computer simulations we found the maximum transmission of light propagation. Obtained the best transmission results are given in the previous chapter.

REFERENCES

- Baba, T., A. Motegi, T. Iwai, N. Fukaya, Y. Watanabe, and A. Sakai (2002). Light propagation characteristics of straight single-line-defect waveguides in photonic crystal slabs fabricated into a silicon-on-insulator substrate. *Quantum Electronics, IEEE Journal of* 38(7), 743–752.
- Benisty, H. (1996). Modal analysis of optical guides with two-dimensional photonic band-gap boundaries. *Journal of applied physics* 79(10), 7483–7492.
- Berenger, J.-P. (1994). A perfectly matched layer for the absorption of electromagnetic waves. *Journal of computational physics* 114(2), 185–200.
- Bloch, F. (1929). Über die quantenmechanik der elektronen in kristallgittern. *Zeitschrift für physik* 52(7-8), 555–600.
- Chutinan, A., S. John, and O. Toader (2003). Diffractionless flow of light in all-optical microchips. *Physical review letters* 90(12), 123901.
- Chutinan, A. and S. Noda (2000). Waveguides and waveguide bends in two-dimensional photonic crystal slabs. *Physical review B* 62(7), 4488.
- Floquet, G. (1883). Sur les equations differentielles lineaires. *Ann. ENS [2]* 12, 47–88.
- Hughes, S., L. Ramunno, J. F. Young, and J. Sipe (2005). Extrinsic optical scattering loss in photonic crystal waveguides: role of fabrication disorder and photon group velocity. *Physical review letters* 94(3), 033903.
- Imada, M., L. H. Lee, M. Okano, S. Kawashima, and S. Noda (2006). Development of three-dimensional photonic-crystal waveguides at optical-communication wavelengths. *Applied physics letters* 88(17), 171107.
- Ishizaki, K., M. Koumura, K. Suzuki, K. Gondaira, and S. Noda (2013). Realization of three-dimensional guiding of photons in photonic crystals. *Nature Photonics* 7(2), 133–137.
- Ishizaki, K. and S. Noda (2009). Manipulation of photons at the surface of three-dimensional photonic crystals. *Nature* 460(7253), 367–370.

- Joannopoulos, J. D., P. R. Villeneuve, and S. Fan (1997). Photonic crystals: putting a new twist on light. *Nature* 386(6621), 143–149.
- John, S. (1987). Strong localization of photons in certain disordered dielectric superlattices. *Physical review letters* 58(23), 2486.
- Johnson, S. G., S. Fan, P. R. Villeneuve, J. Joannopoulos, and L. Kolodziejski (1999). Guided modes in photonic crystal slabs. *Physical Review B* 60(8), 5751.
- Johnson, S. G., P. R. Villeneuve, S. Fan, and J. Joannopoulos (2000). Linear waveguides in photonic-crystal slabs. *Physical Review B* 62(12), 8212.
- Kafesaki, M., M. Agio, and C. Soukoulis (2002). Waveguides in finite-height two-dimensional photonic crystals. *JOSA B* 19(9), 2232–2240.
- Kawashima, S., K. Ishizaki, and S. Noda (2010). Light propagation in three-dimensional photonic crystals. *Optics express* 18(1), 386–392.
- Kuchinsky, S., D. Allan, N. Borrelli, and J.-C. Cotteverte (2000). 3d localization in a channel waveguide in a photonic crystal with 2d periodicity. *Optics communications* 175(1), 147–152.
- Kuramochi, E., M. Notomi, S. Hughes, A. Shinya, T. Watanabe, and L. Ramunno (2005). Disorder-induced scattering loss of line-defect waveguides in photonic crystal slabs. *Physical Review B* 72(16), 161318.
- Lin, S.-Y., E. Chow, V. Hietala, P. R. Villeneuve, and J. Joannopoulos (1998). Experimental demonstration of guiding and bending of electromagnetic waves in a photonic crystal. *Science* 282(5387), 274–276.
- Lin, S.-Y., E. Chow, S. Johnson, and J. Joannopoulos (2000). Demonstration of highly efficient waveguiding in a photonic crystal slab at the 1.5- μm wavelength. *Optics letters* 25(17), 1297–1299.
- Loncar, M., T. Doll, J. Vuckovic, and A. Scherer (2000). Design and fabrication of silicon photonic crystal optical waveguides. *Lightwave Technology, Journal of* 18(10), 1402–1411.

- Lončar, M., D. Nedeljković, T. Doll, J. Vučković, A. Scherer, and T. P. Pearsall (2000). Waveguiding in planar photonic crystals. *Applied Physics Letters* 77(13), 1937–1939.
- Meade, R. D., A. Devenyi, J. Joannopoulos, O. Alerhand, D. Smith, and K. Kash (1994). Novel applications of photonic band gap materials: Low-loss bends and high q cavities. *Journal of applied physics* 75(9), 4753–4755.
- Mekis, A., J. Chen, I. Kurland, S. Fan, P. R. Villeneuve, and J. Joannopoulos (1996). High transmission through sharp bends in photonic crystal waveguides. *Physical Review Letters* 77(18), 3787.
- Mekis, A., S. Fan, and J. Joannopoulos (1998). Bound states in photonic crystal waveguides and waveguide bends. *Physical Review B* 58(8), 4809.
- Noda, S., K. Tomoda, N. Yamamoto, and A. Chutinan (2000). Full three-dimensional photonic bandgap crystals at near-infrared wavelengths. *Science* 289(5479), 604–606.
- Sami Sözüer, H. and H. DUYGU ŞENGÜN (2011). Photonic crystal assisted 90 waveguide bend. *International Journal of Modern Physics B* 25(16), 2167–2182.
- Shinya, A., M. Notomi, I. Yokohama, C. Takahashi, J.-I. Takahashi, and T. Tamamura (2002). Two-dimensional si photonic crystals on oxide using soi substrate. *Optical and quantum electronics* 34(1-3), 113–121.
- Sözüer, H. S. and K. Sevim (2005). Robustness of one-dimensional photonic band gaps under random variations of geometrical parameters. *Physical Review B* 72(19), 195101.
- Taniyama, H., M. Notomi, and Y. Yoshikuni (2005). Propagation characteristics of one-dimensional photonic crystal slab waveguides and radiation loss. *Physical Review B* 71(15), 153103.
- Tokushima, M., H. Kosaka, A. Tomita, and H. Yamada (2000). Lightwave propagation through a 120 sharply bent single-line-defect photonic crystal waveguide. *Applied physics letters* 76(8), 952–954.
- Yablonovitch, E. (1987). Inhibited spontaneous emission in solid-state physics and electronics. *Physical review letters* 58(20), 2059.

Yee, K. S. et al. (1966). Numerical solution of initial boundary value problems involving maxwells equations in isotropic media. *IEEE Trans. Antennas Propag* 14(3), 302–307.

VITA

Date and Place of Birth: 28.09.1981, İzmir - Turkey

EDUCATION

2007 - 2014 Doctor of Philosophy in Mathematics

Graduate School of Engineering and Sciences, İzmir Institute of Technology,
İzmir -Turkey

Thesis Title: Mathematical Modelling of Light Propagation in Photonic
Crystal Waveguides

Supervisor: Associated Prof. Dr. H. Sami Sozuer

2004 - 2007 Master of Science in Mathematics

Graduate School of Engineering and Sciences, İzmir Institute of Technology
İzmir -Turkey

Thesis Title: Classical and Quantum Euler Equation

Supervisor: Prof. Dr. Oktay PASHAEV

2000 - 2004 Bachelor of Mathematics

Department of Physics, İzmir Institute of Technology, İzmir - Turkey

PROFESSIONAL EXPERIENCE

2005 - 2014 Research and Teaching Assistant

Department of Mathematics, İzmir Institute of Technology,
İzmir -Turkey

PUBLICATIONS